

2014-01-01

# Digitally Manufactured Spatially Variant Photonic Crystals

Javier Jair Pazos

*University of Texas at El Paso*, [javier.j.pazos@gmail.com](mailto:javier.j.pazos@gmail.com)

Follow this and additional works at: [https://digitalcommons.utep.edu/open\\_etd](https://digitalcommons.utep.edu/open_etd)



Part of the [Electrical and Electronics Commons](#), [Electromagnetics and Photonics Commons](#), and the [Physics Commons](#)

---

## Recommended Citation

Pazos, Javier Jair, "Digitally Manufactured Spatially Variant Photonic Crystals" (2014). *Open Access Theses & Dissertations*. 1323.  
[https://digitalcommons.utep.edu/open\\_etd/1323](https://digitalcommons.utep.edu/open_etd/1323)

This is brought to you for free and open access by DigitalCommons@UTEP. It has been accepted for inclusion in Open Access Theses & Dissertations by an authorized administrator of DigitalCommons@UTEP. For more information, please contact [lweber@utep.edu](mailto:lweber@utep.edu).

# DIGITALLY MANUFACTURED SPATIALLY VARIANT PHOTONIC CRYSTALS

JAVIER JAIR PAZOS

Department of Electrical and Computer Engineering

APPROVED:

---

Raymond C. Rumpf, Ph.D., Chair

---

Joseph H. Pierluissi, Ph.D.

---

Shirley V. Moore, Ph.D.

---

Scott Starks, Ph.D.

---

Charles H. Ambler, Ph.D.  
Dean of the Graduate School

Copyright ©

by

Javier Jair Pazos

2014

## **Dedication**

The several years' work, dedication, and struggle that went into achieving this research dissemination are dedicated to my family. In particular, my mother Aracely and my sister Ilvana deserve most of the recognition for embarking on this difficult and arduous road with me and for keeping in tow every step of the way. This work is also dedicated to my aunt Mariela, my uncle David, and cousin Cristobal, who provided a home for me for several years, and were nothing but a positive influence for me.

# DIGITALLY MANUFACTURED SPATIALLY VARIANT PHOTONIC CRYSTALS

by

JAVIER JAIR PAZOS

B.S.E.P., University of Texas at Brownsville, 2010

DISSERTATION

Presented to the Faculty of the Graduate School of  
The University of Texas at El Paso  
in Partial Fulfillment  
of the Requirements  
for the Degree of

DOCTOR OF PHILOSOPHY

Department of Electrical and Computer Engineering

THE UNIVERSITY OF TEXAS AT EL PASO

December 2014

## **Acknowledgements**

I am infinitely grateful to my family for their support and their encouragement every step of the way. I am also very grateful, and very lucky, to have the awesome advisor I did. Dr. Raymond

C. Rumpf was a friend, a mentor, and a colleague, always conscious of my professional development. This work would also not have been possible without the generous support from Dr. Miguel Velez-Reyes, chair of the Electrical & Computer Engineering department, and Dr. David G. Novick, of the department of Computer Science at UTEP. Many, many thanks as well to the department staff, who saved me time and frustration, but also provided many great memories. They include Jesus Zamarripa, Grace Chavarría, Linda Carrillo, Tiffany Gailey, Priscilla Carrasco, Sukie Vasquez, and more. Thank you all for your assistance, and most of all, your friendship.

## **Abstract**

Metamaterials and photonic crystals are engineered composites that exhibit electromagnetic properties superior to those found in nature. They have been shown to produce novel and useful phenomena that allow extraordinary control over the electromagnetic field. One of these phenomena is self-collimation, an effect observed in photonic crystals in which a beam of light propagates without diffraction and is forced to flow in the direction of the crystal. Self-collimation however, like many of the mechanisms enabled through dispersion engineering, is effective in directions only along the principal axes of the lattice. To this effect, a general purpose synthesis procedure was developed that is capable of simultaneously spatially varying the orientation, lattice spacing, fill fraction, and other properties of a periodic structure throughout its volume in a way that leaves the overall structure smooth and continuous. This enables unprecedented control over a beam's propagation, one that is now dictated by the spatially variant orientation of the unit cells. The algorithm was also used to synthesize a spatially variant photonic crystal waveguide based on band gaps. The waveguide was designed to be multi-moded, and it was spatially varied in a manner that highly minimizes crosstalk between the modes. Designing these devices with only ordinary all-dielectric materials, 3D printing was well-suited to produce these novel sculpted dielectric devices.

## Table of Contents

Acknowledgements.....	v
Abstract.....	vi
Table of Contents.....	vii
List of Tables .....	ix
List of Figures.....	x
Chapter 1: Introduction.....	1
1.1 Motivation.....	1
1.2 Overview of Dissertation .....	2
Chapter 2: Computational Electromagnetics for Planar Photonic Crystals.....	4
2.1 Maxwell’s Equations .....	4
2.2 Finite-Difference Frequency-Domain.....	6
2.3 Plane Wave Expansion Method.....	15
Chapter 3: Photonic Crystals .....	24
3.1 Mathematical Framework .....	24
3.2 Band Gaps.....	26
3.3 Self-Collimation.....	28
Chapter 4: Synthesis of Spatially Variant Lattices .....	42
4.1 Motivation.....	42
4.2 Synthesis Algorithm.....	43
4.3 Notes on Implementation.....	52
4.4 Deformation Control.....	53
Chapter 5: Spatially Variant Self-Collimating Photonic Crystals .....	56
5.1 Spatially Variant Self-Collimating Photonic Crystal at Microwave Frequencies .....	57
5.2 Spatially Variant Self-Collimating Photonic Crystals at Optical Frequencies .....	67
Chapter 6: Spatially Variant Multi-Mode Photonic Crystal Waveguides .....	74
6.1 Introduction.....	74
6.2 Background.....	74

6.3	Photonic Crystal Band Gap Waveguides .....	75
6.4	Multi-Mode Band Gap Waveguides .....	80
6.5	Spatially Variant Multi-Mode Band Gap Waveguides .....	81
Chapter 7: Conclusion.....		86
7.1	Summary .....	86
7.2	Future Work .....	86
References .....		87
Vita .....		90

## List of Tables

No table of figures entries found.

## List of Figures

Figure 2.1: LHI materials and their implications.....	6
Figure 2.2: Example derivative operator for a $2 \times 2$ grid in matrix form with Dirichlet boundary conditions.....	7
Figure 2.3 [28]: The Yee grid unit cell, which spatially staggers the field vector components for improved numerical convergence.....	11
Figure 2.4: The process of reducing a 3D device to a 2D model.....	12
Figure 2.5: A color-coded representation of the two distinct modes that Maxwell's equations decouple into under certain conditions.....	13
Figure 2.6: Constructing the $\mathbf{Q}$ matrix for the total-field/scattered-field technique.....	14
Figure 3.1: Band diagram showing the TM modes for a photonic crystal of dielectric rods in air background. The rods have a refractive index $n = 2.5$ and radius $r = 0.2a$ . The band gap frequency range is highlighted in yellow.....	27
Figure 3.2 [11]: (a) map of dispersion surfaces for a square photonic crystal and (b) the process of extracting its isofrequency contours.....	29
Figure 3.3 [52]: (a) square isofrequency contour and its effect on energy propagation, and (b) self-collimation observed in a lattice. A diverging beam is collimated in the lattice and is forced to propagate without scattering or diffraction.....	30
Figure 3.4 [11]: Determining the performance metrics for the self-collimation effect. Only the upper right quadrant of the Brillouin zone is shown here.....	32
Figure 3.5 [11]: Illustration of the self-collimation effect and the strength metric.....	34
Figure 3.6 [11]: Visualization of self-collimation over a range of frequencies. The optimum frequency for self-collimation is slightly offset from the inflection point.....	35
Figure 3.7 [11]: Unit cells for optimization.....	36
Figure 3.8 [11]: Performance metrics as a function of dielectric constant for the TM mode.....	37
Figure 3.9 [11]: Performance metrics as a function of dielectric constant for the TE mode.....	38
Figure 3.10 [11]: Performance metrics as a function of fill fraction.....	39
Figure 3.11 [11]: Demonstration of the performance enhancement in a spatially variant self-collimating photonic crystal for the TM mode. (a) Lattice with high FOM, and (b) lattice with lower FOM.....	41
Figure 4.1: The baseline unit cell, its spatial harmonics representation, and the parameters which can be extracted from it.....	44
Figure 4.2: The spatially variant parameter functions and their effects on the lattice.....	46
Figure 4.3: Example of the expansion of a grating vector to a full grid.....	47
Figure 4.4: Implementing spatially variant orientation and lattice spacing to the current $K$ function.....	48
Figure 4.5 [21]: Comparison of the direct versus grating phase approach for the construction of a spatially variant 1D grating.....	50
Figure 4.6 [21]: Using the threshold technique to control the fill fraction of a lattice constructed with only two grating vectors. This technique results in many geometries while remaining computationally inexpensive.....	52
Figure 4.7 [59]: (a) Beam propagation through an SVPC generated using the basic algorithm. Beam scatters at the center of the device. (b) Beam propagation through an SVPC generating with the modified algorithm to control deformations. Beam is well confined and propagates efficiently through the lattice.....	55

Figure 5.1 [60]: Photograph of the spatially variant self-collimating lattice designed to operate at microwave frequencies. ....	58
Figure 5.2 [60]: Three-dimensional simple cubic unit cell with 30% fill fraction. ....	60
Figure 5.3 [60]: Isofrequency contours superimposed with field of view. ....	62
Figure 5.4 [60]: Final lattice superimposed above the orientation function. ....	63
Figure 5.5 [60]: Simulations of lattices of different sizes to determine the minimum bend radius. (a) $7 \times 7$ unit cells. (b) $12 \times 12$ unit cells. (c) $17 \times 17$ unit cells. (d) $22 \times 22$ unit cells. ....	64
Figure 5.6 [60]: Experimental results for the spatially variant self-collimating lattice. (a) Spatially variant lattice in test setup. (b) Measured field profile around the perimeter of the device. ....	65
Figure 5.7 [61]: False-color SEM images of an SVPC. The perspective views and dimensional analysis noted in the figure were the information available to accurately model these in a computational domain. ....	68
Figure 5.8 : (a)-(b) [61] Perspective views of the ideal (blue) versus diffusion-simulated model unit cell. (c) A 2D approximation of the effective refractive index profile. ....	69
Figure 5.9 [61]: The 2D model that was generated from the 3D lattice using the effective index method. This 2D model was used for simulating the SVPCs. ....	70
Figure 5.10 [61]: (a – c) SEM image views of the SVPCs of varying fill factors and (d – f) the electromagnetic simulations of the intensity of vertically polarized light. (g – i) The experimentally measured beam-bending efficiency of the SVPCs versus varying fill factors. ....	71
Figure 5.11 [61]: Experimental results of the intensity line-scans for an SVPC guiding a vertically polarized beam versus a horizontally polarized one. The simulation visually agrees very well with experimental measurements. ....	72
Figure 5.12 [61]: False-color SEM image of a spatially variant photonic crystal and the field profile measurements (blue ribbons) along its perimeter, confirming a successful bending of optical beams. ....	73
Figure 6.1: (a) A common photonic crystal waveguide and (b) its supercell representation. ....	77
Figure 6.2: In the FDFD algorithm, information of the Bloch wave vector, which accounts for wave propagation, is embedded in the derivative operators. ....	79
Figure 6.3: Two techniques for extracting potential guided modes. The selection is made by measuring field concentrations in the specified regions. This work uses the technique of (b). ....	<b>Error! Bookmark not defined.</b>
Figure 6.4: (a) A photonic crystal band gap waveguide with a line defect width of $4a$ and (b-e) the four guided modes that it supports. ....	81
Figure 6.5: (a) A spatially variant W4 photonic crystal band gap waveguide made to turn $90^\circ$ . Waveguides supporting a large number of modes are more sensitive to deformations in the lattice when spatially varied. These waveguides require additional deformation control; (b) shows a waveguide with uniform regions at the input and output faces, and its regions of deformation control shaded red. ....	83
Figure 6.6 [59]: (a)-(c) First three modes in an ordinary multimode dielectric waveguide with $n_{core} = 3.4$ and $n_{clad} = 1.0$ . Width of the guide was $w = 0.5\lambda_0$ . (d)-(f) First three modes in a multimode band gap waveguide cut from a uniform lattice with $n_{rod} = 3.4$ and $n_{air} = 1.0$ . Lattice spacing is $a = 0.42\lambda_0$ , bend radius is $r_{bend} = 3.2\lambda_0$ , rod radius is $0.18a$ , and the width of the guide was $4a$ . (g)-(i) First three modes in a multimode band gap waveguide cut from a spatially-variant lattice with the same parameters as (d)-(f). ....	85



# Chapter 1: Introduction

## 1.1 MOTIVATION

It is ultimately desired to control everything about the electromagnetic field throughout some volume. This includes the flow of energy, the modal profile of the field, the phase of the waves, the polarization of the waves, intermodal crosstalk, and more. Many degrees of freedom are required in order to control such properties. Periodic structures, including photonic crystals and metamaterials, have been shown to provide extraordinary control over the electromagnetic field. Some of the more noticed mechanisms for wave control employ effects like band gaps [1-6], self-collimation [7-14], anisotropy [15, 16], and more [17-20]. Mechanisms based on these, however, are effective only along the principal axes of the lattice.

To exploit the directional dependence of these types of mechanisms, it is often desired to functionally grade and/or spatially vary a periodic structure like a photonic crystal or metamaterial, yet no general method for achieving this has been offered. To this effect, a general purpose synthesis procedure was developed that is capable of simultaneously spatially varying the lattice orientation, lattice spacing, fill fraction, and more throughout its volume in such a way that renders an overall smooth and continuous lattice [21]. Minimizing deformations and discontinuities is vital because these produce scattering and field concentrations that can degrade the performance of the device. The ability to spatially vary the orientation of the unit cells throughout a lattice enables phenomena like self-collimation and band gaps to be fully exploited. The capability of this tool to vary so many degrees of freedom is critical when multiple properties of the field and devices are to be controlled at the same time. The synthesis algorithm is unique in that it calculates the physical geometry of a spatially variant lattice so that it can be directly fabricated. In contrast, transformation optics, another popular spatial transform method, is a coordinate transformation technique that only calculates the permittivity and permeability tensor functions, which often require exotic materials [22].

A lattice with properly synthesized spatial variance, then, could exploit these mechanisms to arbitrarily control the flow of energy. This approach could provide an attractive alternative to transformation optics and graded index devices because the final structures require no anisotropy, permeability, or extreme parameters. This approach also provides many additional degrees of freedom to control the field.

## **1.2 OVERVIEW OF DISSERTATION**

Chapter 1 introduces a principal goal of this work to produce a novel synthesis algorithm. Two effects of photonic crystals obtained through engineered dispersion are selected as the mechanisms to be exploited through proper spatial variance. A popular spatial transform technique is introduced, and several major points are given as to why the synthesis algorithm would provide a much more practical means to modeling and fabrication.

Chapter 2 is concerned with the concepts of computational electromagnetic modeling. Maxwell's equations are presented and shaped to a computationally suitable form. Multiple sections are then dedicated to the finite-difference frequency-domain and the plane wave expansion methods, two of the major numerical methods used in this text and in photonic crystal modeling in general.

Photonic crystals and important concepts are presented in Chapter 3. Their mathematical and computational frameworks are discussed. Band diagrams, one of the most common means to analyze photonic crystals, are presented and discussed. From these, the concepts of dispersion surfaces and isofrequency contours are discussed. Finally, the self-collimation effect and band gaps are presented as viable tools for electromagnetic wave control.

Chapter 4 provides the motivation for, and a walkthrough of, the synthesis of spatially variant lattices. The need for this tool and its many advantages over existing methods are discussed. The synthesis procedure and its mathematical formulation is presented and discussed in detail. Finally, notes on implementation are provided.

Chapter 5 presents the first set of devices enabled by the synthesis algorithm: spatially variant photonic crystals with self-collimation. The first device operates at microwave frequencies, and the design, fabrication, and experimental testing and results are discussed. The second device is a spatially variant self-collimating photonic crystal designed to bend optical beams. The design, fabrication, and experimental results for this application is also discussed in detail.

Chapter 6 presents a photonic crystal waveguide, based on band gaps, that is spatially varied to control the flow of electromagnetic waves. The waveguide is designed to be multimoded, and it is unique in that it avoids modal crosstalk even when the beam is routed through a 90° bend. It is granted this uniqueness through proper spatial variance.

Concluding remarks, a summary statement, and notes on future work are located in Chapter 7.

## Chapter 2: Computational Electromagnetics for Planar Photonic Crystals

This chapter presents a mathematical framework suitable for describing electromagnetic wave behavior in photonic crystal structures. Maxwell's equations are presented in a general form; they are then molded by considerations of the physical reality of the devices under test in this work. This new form of Maxwell's equations is also more suitable for implementation using several computational electromagnetics algorithms, including the finite-difference frequency domain (FDFD) method, and the plane wave expansion method (PWEM).

### 2.1 MAXWELL'S EQUATIONS

Maxwell's equations will be presented in their differential form in the frequency domain [23]. The general set of four equations is described below along with a description and implication of each.

Gauss's law relates a distribution of charge to the resulting electric field.

$$\nabla \cdot \vec{D} = \rho_v \quad (2.1)$$

The second divergence equation claims that there is no magnetic charge (magnetic monopole).

$$\nabla \cdot \vec{B} = 0 \quad (2.2)$$

Faraday's law indicates that a changing magnetic field induces an electric field. No matter how a change in the magnetic field is induced, a proportional change in voltage, and thus an electric field, will be produced.

$$\nabla \times \vec{E} = -j\omega\vec{B} \quad (2.3)$$

Ampere's law states that an electric current and/or a time-changing electric flux density induce a magnetic field which circles them.

$$\nabla \times \vec{H} = \vec{J} + j\omega\vec{D} \quad (2.4)$$

### 2.1.1 Source-Free, Divergence-Free Media

The entirety of the work in this text concerns itself with the propagation of electromagnetic waves in passive, dielectric media. It is therefore safe to assume that there are no free charges in the device, nor are there any current sources. As consequence of the imposed divergence- and source-free conditions, the standard form of Maxwell's equations in the context of this work become

$$\begin{aligned}\nabla \cdot \vec{D} &= 0 \\ \nabla \cdot \vec{B} &= 0 \\ \nabla \times \vec{E} &= -j\omega\vec{B} \\ \nabla \times \vec{H} &= j\omega\vec{D}\end{aligned}\tag{2.5}$$

The reader should note that the new form of Eq. (2.1) now implies that the electric field must form loops [24]. There is an additional set of equations to relate the field quantities to the medium parameters: The constitutive relations.

$$\begin{aligned}\vec{D} &= [\varepsilon] \vec{E} \\ \vec{B} &= [\mu] \vec{H}\end{aligned}\tag{2.6}$$

These account for anisotropy, but not for bi-isotropic nor bi-anisotropic media. The most general form of these allows for materials that are nonlinear, anisotropic, and inhomogeneous. For the purpose of this work, it is assumed that the materials are operated at field intensities low enough to be considered linear, and they are ordinary materials described by isotropic material tensors (more details on this in later sections). The simplest case is when materials are linear, homogeneous, and isotropic (LHI). Figure 2.1 depicts what it means for a material to be described as LHI.

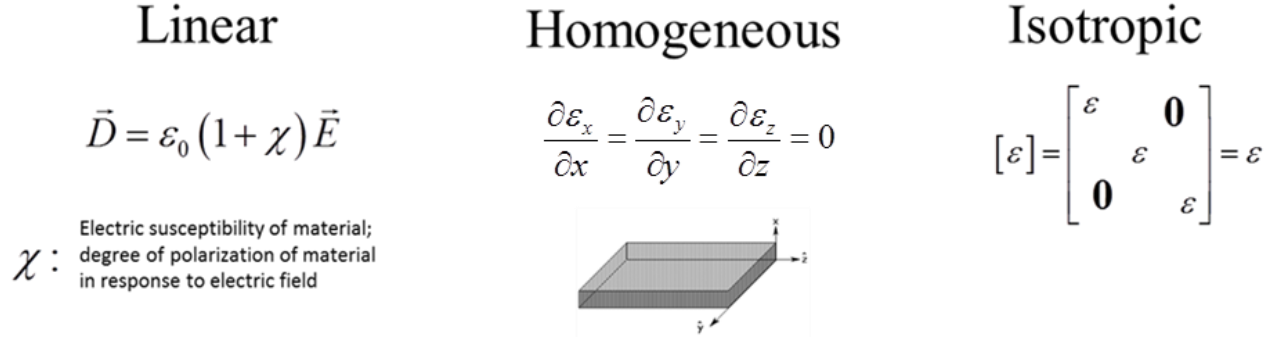


Figure 2.1: LHI materials and their implications.

The materials for this work are allowed to be inhomogeneous, as inhomogeneity is required to achieve substantial control over electromagnetic waves. The constitutive relations for linear, isotropic, and inhomogeneous materials can be expressed as shown below.

$$\begin{aligned} \vec{D}(\vec{r}) &= \epsilon(\vec{r}) \vec{E}(\vec{r}) \\ \vec{B}(\vec{r}) &= \mu(\vec{r}) \vec{H}(\vec{r}) \end{aligned} \tag{2.7}$$

The vector  $\vec{r}$  denotes spatial position. These relations, in the frequency domain, are expressed as a product; in the time domain, they are related through a convolution operation.

Finally, Maxwell's equations, as they will be used in this text, along with their constitutive parameters, are presented below.

$\begin{aligned} \nabla \times \vec{E}(\vec{r}) &= -j\omega \vec{B}(\vec{r}) \\ \nabla \times \vec{H}(\vec{r}) &= j\omega \vec{D}(\vec{r}) \end{aligned}$	$\begin{aligned} \vec{D}(\vec{r}) &= \epsilon(\vec{r}) \vec{E}(\vec{r}) \\ \vec{B}(\vec{r}) &= \mu(\vec{r}) \vec{H}(\vec{r}) \end{aligned}$
-----------------------------------------------------------------------------------------------------------------------------------------------------------	---------------------------------------------------------------------------------------------------------------------------------------------

(2.8)

## 2.2 FINITE-DIFFERENCE FREQUENCY-DOMAIN

The finite-difference frequency-domain (FDFD) method is a fully vectorial numerical method that obtains rigorous solutions to Maxwell's equations. Numerical methods are classified as rigorous when their solutions eventually converge exactly to those calculated analytically. Finite differences imply the transformation of Maxwell's equations into a set of linear algebraic equations using the finite-difference method [25]. Being a frequency domain method, it analyzes electromagnetic properties at a single frequency rather than over time. This

makes it very well suited to resolve sharp resonances that may be otherwise difficult to resolve using time-domain methods.

### 2.2.1 Finite-Difference Framework

The finite-difference computational framework is based on Maxwell's equations being cast in the form of linear algebraic equations. This work utilizes the central finite-difference method. Linear operations, such as derivatives, are cast as square, sparse matrices; unknown quantities, such as field quantities, are cast as column vectors; and point-by-point multiplication is achieved through the use of a square diagonal matrix. The reader is referred to Ref. [25] for more detailed information on these concepts. Fig. 2.2 shows an example of what a derivative and its central finite-difference representation might look like. This particular example is of a  $2 \times 2$  grid where values at the boundaries are set to zero (Dirichlet boundary conditions). The matrix derivative operators are typically initialized as sparse square matrices with entries of zero's; these are denoted by the black 0 entries. Then, the appropriate entries are manually added to perform the desired operation and apply the desired boundary conditions; these entries are shown in red, and in this example, depict the entries required for a first derivative operator along the  $x$ -direction with Dirichlet boundary conditions. Matrix notation (bold  $\mathbf{D}$ ) is also introduced in Figure 2.2 as it will be used for the remainder of this text. The remaining operators, and their variation due to boundary conditions and grid size, can be deduced by analogy.

$$\frac{\partial}{\partial x} \quad \longrightarrow \quad \mathbf{D}_x = \frac{1}{2\Delta x} \begin{bmatrix} 0 & \mathbf{1} & 0 & 0 \\ \mathbf{-1} & 0 & \mathbf{0} & 0 \\ 0 & \mathbf{0} & 0 & \mathbf{1} \\ 0 & 0 & \mathbf{-1} & 0 \end{bmatrix}$$

Figure 2.2: Example derivative operator for a  $2 \times 2$  grid in matrix form with Dirichlet boundary conditions.

### 2.2.2 Numerical Stability

There are steps that can be taken to ensure numerical stability and increase the accuracy of computational methods. One such step arises from the fact that the electric and magnetic field magnitudes are approximately three orders of magnitude apart. Eq. (2.9) expresses this fact along with alternate expressions describing the same.

$$\frac{|\vec{E}|}{|\vec{H}|} = \eta_0 = \mu_0 c_0 = \sqrt{\frac{\mu_0}{\epsilon_0}} = \frac{1}{\epsilon_0 c_0} \cong 377\Omega \quad (2.9)$$

The free space impedance is expressed as  $\eta_0$ ,  $\mu_0$  is the free space permeability,  $\epsilon_0$  is the free space permittivity, and  $c_0$  is the speed of light in vacuum. The magnitude discrepancy between the electric and magnetic field here can (computationally) lead to the loss of significant digits and, consequently, numerical accuracy. Eq. (2.10) proposes a normalized magnetic field parameter, which softens this numerical inconsistency and, for convenience, includes the additional step of removing the negative sign entirely from the curl equations, making them more similar.

$$\tilde{\vec{H}} = -j\sqrt{\frac{\mu_0}{\epsilon_0}}\vec{H} \quad (2.10)$$

Expressing the material parameter relations as  $\mu = \mu_r \mu_0$  and  $\epsilon = \epsilon_r \epsilon_0$ , and using the normalized magnetic field parameter introduced above, Maxwell's curl equations can be written in terms of the free-space wave number  $k_0 = \omega\sqrt{\mu_0 \epsilon_0}$ .

$$\begin{aligned} \nabla \times \vec{E} &= k_0 \mu_r \tilde{\vec{H}} \\ \nabla \times \tilde{\vec{H}} &= k_0 \epsilon_r \vec{E} \end{aligned} \quad (2.11)$$

### 2.2.3 FDFD Formulation

The FDFD algorithm (with the conventions and substitutions explained above) begins by expanding the curl equations of Eq. (2.11) into their Cartesian components (Cartesian in this text, but any coordinate system can be used).

$$\begin{aligned}
\frac{\partial E_z}{\partial y} - \frac{\partial E_y}{\partial z} &= k_0 (\mu_{xx} \tilde{H}_x + \mu_{xy} \tilde{H}_y + \mu_{xz} \tilde{H}_z) \\
\frac{\partial E_x}{\partial z} - \frac{\partial E_z}{\partial x} &= k_0 (\mu_{yx} \tilde{H}_x + \mu_{yy} \tilde{H}_y + \mu_{yz} \tilde{H}_z) \\
\frac{\partial E_y}{\partial x} - \frac{\partial E_x}{\partial y} &= k_0 (\mu_{zx} \tilde{H}_x + \mu_{zy} \tilde{H}_y + \mu_{zz} \tilde{H}_z)
\end{aligned} \tag{2.12}$$

$$\begin{aligned}
\frac{\partial \tilde{H}_z}{\partial y} - \frac{\partial \tilde{H}_y}{\partial z} &= k_0 (\varepsilon_{xx} E_x + \varepsilon_{xy} E_y + \varepsilon_{xz} E_z) \\
\frac{\partial \tilde{H}_x}{\partial z} - \frac{\partial \tilde{H}_z}{\partial x} &= k_0 (\varepsilon_{yx} E_x + \varepsilon_{yy} E_y + \varepsilon_{yz} E_z) \\
\frac{\partial \tilde{H}_y}{\partial x} - \frac{\partial \tilde{H}_x}{\partial y} &= k_0 (\varepsilon_{zx} E_x + \varepsilon_{zy} E_y + \varepsilon_{zz} E_z)
\end{aligned} \tag{2.13}$$

As stated before, the devices in this text are of isotropic media. Therefore, diagonal tensors of equal entries are assumed; off-diagonal entries and diagonally anisotropic terms are ignored.

$$\begin{aligned}
\frac{\partial E_z}{\partial y} - \frac{\partial E_y}{\partial z} &= k_0 \mu_{xx} \tilde{H}_x \\
\frac{\partial E_x}{\partial z} - \frac{\partial E_z}{\partial x} &= k_0 \mu_{yy} \tilde{H}_y \\
\frac{\partial E_y}{\partial x} - \frac{\partial E_x}{\partial y} &= k_0 \mu_{zz} \tilde{H}_z
\end{aligned} \tag{2.14}$$

$$\begin{aligned}
\frac{\partial \tilde{H}_z}{\partial y} - \frac{\partial \tilde{H}_y}{\partial z} &= k_0 \varepsilon_{xx} E_x \\
\frac{\partial \tilde{H}_x}{\partial z} - \frac{\partial \tilde{H}_z}{\partial x} &= k_0 \varepsilon_{yy} E_y \\
\frac{\partial \tilde{H}_y}{\partial x} - \frac{\partial \tilde{H}_x}{\partial y} &= k_0 \varepsilon_{zz} E_z
\end{aligned} \tag{2.15}$$

The FDFD method is generally employed to simulate electromagnetic behavior at a particular frequency. This fact allows for an additional substitution, where the frequency term is embedded in the grid coordinates. The normalized Cartesian grid coordinates are expressed as  $x' = k_0 x$ ,  $y' = k_0 y$ , and  $z' = k_0 z$ . Eqs. (2.14) & (2.15) are now written in terms of the normalized grid.

The frequency term  $k_0$  is absorbed by the spatial coordinates, and therefore the derivative operators.

$$\begin{aligned}\frac{\partial E_z}{\partial y'} - \frac{\partial E_y}{\partial z'} &= \mu_{xx} \tilde{H}_x \\ \frac{\partial E_x}{\partial z'} - \frac{\partial E_z}{\partial x'} &= \mu_{yy} \tilde{H}_y \\ \frac{\partial E_y}{\partial x'} - \frac{\partial E_x}{\partial y'} &= \mu_{zz} \tilde{H}_z\end{aligned}\tag{2.16}$$

$$\begin{aligned}\frac{\partial \tilde{H}_z}{\partial y'} - \frac{\partial \tilde{H}_y}{\partial z'} &= \varepsilon_{xx} E_x \\ \frac{\partial \tilde{H}_x}{\partial z'} - \frac{\partial \tilde{H}_z}{\partial x'} &= \varepsilon_{yy} E_y \\ \frac{\partial \tilde{H}_y}{\partial x'} - \frac{\partial \tilde{H}_x}{\partial y'} &= \varepsilon_{zz} E_z\end{aligned}\tag{2.17}$$

At this point, the formulation is developed enough to convert to matrix notation [16, 24, 26]. The field quantities, the material parameters, and the derivative operators are expressed in terms of vectors and matrices.

$$\begin{aligned}\mathbf{D}_{y'}^e \mathbf{e}_z - \mathbf{D}_{z'}^e \mathbf{e}_y &= \boldsymbol{\mu}_{xx} \tilde{\mathbf{h}}_x \\ \mathbf{D}_{z'}^e \mathbf{e}_x - \mathbf{D}_{x'}^e \mathbf{e}_z &= \boldsymbol{\mu}_{yy} \tilde{\mathbf{h}}_y \\ \mathbf{D}_{x'}^e \mathbf{e}_y - \mathbf{D}_{y'}^e \mathbf{e}_x &= \boldsymbol{\mu}_{zz} \tilde{\mathbf{h}}_z \\ \mathbf{D}_{y'}^h \tilde{\mathbf{h}}_z - \mathbf{D}_{z'}^h \tilde{\mathbf{h}}_y &= \boldsymbol{\varepsilon}_{xx} \mathbf{e}_x \\ \mathbf{D}_{z'}^h \tilde{\mathbf{h}}_x - \mathbf{D}_{x'}^h \tilde{\mathbf{h}}_z &= \boldsymbol{\varepsilon}_{yy} \mathbf{e}_y \\ \mathbf{D}_{x'}^h \tilde{\mathbf{h}}_y - \mathbf{D}_{y'}^h \tilde{\mathbf{h}}_x &= \boldsymbol{\varepsilon}_{zz} \mathbf{e}_z\end{aligned}\tag{2.18}$$

$$\begin{aligned}\mathbf{D}_{y'}^h \tilde{\mathbf{h}}_z - \mathbf{D}_{z'}^h \tilde{\mathbf{h}}_y &= \boldsymbol{\varepsilon}_{xx} \mathbf{e}_x \\ \mathbf{D}_{z'}^h \tilde{\mathbf{h}}_x - \mathbf{D}_{x'}^h \tilde{\mathbf{h}}_z &= \boldsymbol{\varepsilon}_{yy} \mathbf{e}_y \\ \mathbf{D}_{x'}^h \tilde{\mathbf{h}}_y - \mathbf{D}_{y'}^h \tilde{\mathbf{h}}_x &= \boldsymbol{\varepsilon}_{zz} \mathbf{e}_z\end{aligned}\tag{2.19}$$

The need for separate derivative operators for the  $E$ - and  $H$ - fields arises from the Yee grid convention [27]. Computationally calculating the curl of a multi-dimensional/multi-parameter function can become quite difficult. In 1966, Kane Yee proposed a grid where the vector components of the  $E$ - and  $H$ - fields in a Cartesian grid are spatially staggered. The staggering occurs in a manner which naturally satisfies the zero-divergence conditions implied in Maxwell's

equations. It also yields a more elegant approximation to the curl equations. Figure 2.3 shows the Yee grid unit cell [28].

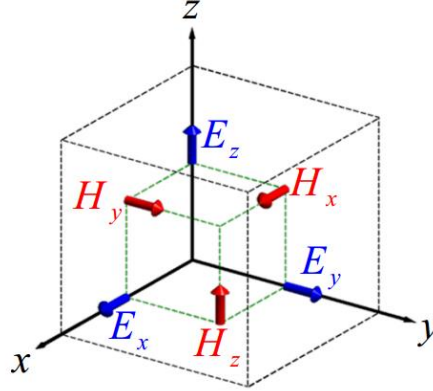


Figure 2.3 [28]: The Yee grid unit cell, which spatially staggers the field vector components for improved numerical convergence.

#### 2.2.4 FDFD Algorithm

Dimensional reduction in computational models should always be sought. It is often the case that a device, especially a photonic crystal device, is uniform along one axis. Additionally, wave propagation may be restricted to the plane of periodicity. When this is the case, a two-dimensional model greatly reduces computation time, and there is very often excellent agreement between these reduced models and the physical devices. All of the electromagnetic analysis in this text is performed on two-dimensional models for two reasons: 1. Two-dimensional models of the devices presented in this text have proven sufficiently accurate, and 2. Three-dimensional analysis of the same can be extremely computationally expensive; sometimes even prohibitively so. Fig. 2.4 shows an example of how a device can often be reduced to two-dimensions and still produce accurate results.

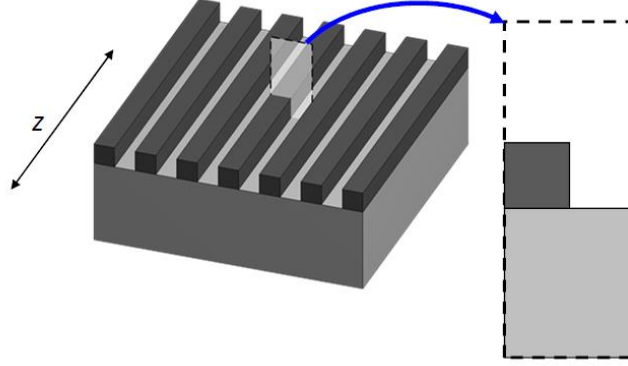


Figure 2.4: The process of reducing a 3D device to a 2D model.

This process of dimensional reduction is valid for devices uniform along the  $z$ -direction and with propagation restricted to the  $x$ - $y$  plane. These properties force the spatial and field derivatives to zero along the  $z$ -direction:  $\frac{\partial}{\partial z} = 0$ ,  $\mathbf{D}_z^e = \mathbf{D}_z^h = \mathbf{0}$ .

The 2D form of Maxwell's equations for the FDFD algorithm now become

$$\begin{aligned} \mathbf{D}_y^e \mathbf{e}_z &= \mu_{xx} \tilde{\mathbf{h}}_x \\ -\mathbf{D}_x^e \mathbf{e}_z &= \mu_{yy} \tilde{\mathbf{h}}_y \\ \mathbf{D}_x^e \mathbf{e}_y - \mathbf{D}_y^e \mathbf{e}_x &= \mu_{zz} \tilde{\mathbf{h}}_z \end{aligned} \quad (2.20)$$

$$\begin{aligned} \mathbf{D}_y^h \tilde{\mathbf{h}}_z &= \epsilon_{xx} \mathbf{e}_x \\ -\mathbf{D}_x^h \tilde{\mathbf{h}}_z &= \epsilon_{yy} \mathbf{e}_y \\ \mathbf{D}_x^h \tilde{\mathbf{h}}_y - \mathbf{D}_y^h \tilde{\mathbf{h}}_x &= \epsilon_{zz} \mathbf{e}_z \end{aligned} \quad (2.21)$$

This particular set of equations decouples into two distinct modes: 1. The “E-Mode”, what is generally called the TM-mode in the literature, solves for the  $E$ -field perpendicular to the plane of periodicity ( $E_z$ ); and 2. The “H-Mode”, or the TE-mode in the literature, which solves for the  $H$ -field perpendicular to the plane of periodicity ( $H_z$ ). The convention of the mode denoted by its out-of-plane field quantity will be used throughout this text (e.g. “E-Mode” solves for  $E_z$ ). This decoupling of equations also implies decoupling of the field quantities.

## E-Mode

$$\begin{aligned}\mathbf{D}_{x'}^h \tilde{\mathbf{h}}_y - \mathbf{D}_{y'}^h \tilde{\mathbf{h}}_x &= \boldsymbol{\varepsilon}_{zz} \mathbf{e}_z \\ \mathbf{D}_{y'}^e \mathbf{e}_z &= \boldsymbol{\mu}_{xx} \tilde{\mathbf{h}}_x \\ -\mathbf{D}_{x'}^e \mathbf{e}_z &= \boldsymbol{\mu}_{yy} \tilde{\mathbf{h}}_y\end{aligned}$$

## H-Mode

$$\begin{aligned}\mathbf{D}_{x'}^e \mathbf{e}_y - \mathbf{D}_{y'}^e \mathbf{e}_x &= \boldsymbol{\mu}_{zz} \tilde{\mathbf{h}}_z \\ \mathbf{D}_{y'}^h \tilde{\mathbf{h}}_z &= \boldsymbol{\varepsilon}_{xx} \mathbf{e}_x \\ -\mathbf{D}_{x'}^h \tilde{\mathbf{h}}_z &= \boldsymbol{\varepsilon}_{yy} \mathbf{e}_y\end{aligned}$$

Figure 2.5: A color-coded representation of the two distinct modes that Maxwell's equations decouple into under certain conditions.

Each mode consists of three equations that share the same three unknown parameters. For each mode, the three equations can combine to form one. Eq. (2.22) depicts this transformation for the E-mode, while Eq. (2.23) does the same for the H-mode.

$$\begin{aligned}\tilde{\mathbf{h}}_x &= \boldsymbol{\mu}_{xx}^{-1} \mathbf{D}_{y'}^e \mathbf{e}_z \\ \tilde{\mathbf{h}}_y &= -\boldsymbol{\mu}_{yy}^{-1} \mathbf{D}_{x'}^e \mathbf{e}_z \\ \left( \mathbf{D}_{x'}^h \boldsymbol{\mu}_{yy}^{-1} \mathbf{D}_{x'}^e + \mathbf{D}_{y'}^h \boldsymbol{\mu}_{xx}^{-1} \mathbf{D}_{y'}^e + \boldsymbol{\varepsilon}_{zz} \right) \mathbf{e}_z &= 0\end{aligned}\tag{2.22}$$

$$\begin{aligned}\mathbf{e}_x &= \boldsymbol{\varepsilon}_{xx}^{-1} \mathbf{D}_{y'}^h \tilde{\mathbf{h}}_z \\ \mathbf{e}_y &= -\boldsymbol{\varepsilon}_{yy}^{-1} \mathbf{D}_{x'}^h \tilde{\mathbf{h}}_z \\ \left( \mathbf{D}_{x'}^e \boldsymbol{\varepsilon}_{yy}^{-1} \mathbf{D}_{x'}^h + \mathbf{D}_{y'}^e \boldsymbol{\varepsilon}_{xx}^{-1} \mathbf{D}_{y'}^h + \boldsymbol{\mu}_{zz} \right) \tilde{\mathbf{h}}_z &= 0\end{aligned}\tag{2.23}$$

The two resulting equations have the form  $\mathbf{A}\mathbf{x} = \mathbf{0}$ , where the unknown quantities depend on the mode being solved. It is convenient at this point to refer to the equations in terms of their mode and their wave matrix according to Eq. (2.24) for the E-mode and Eq. (2.25) for the H-mode.

$$\begin{aligned}\mathbf{A}_E \mathbf{e}_z &= 0 \\ \mathbf{A}_E &= \mathbf{D}_{x'}^h \boldsymbol{\mu}_{yy}^{-1} \mathbf{D}_{x'}^e + \mathbf{D}_{y'}^h \boldsymbol{\mu}_{xx}^{-1} \mathbf{D}_{y'}^e + \boldsymbol{\varepsilon}_{zz}\end{aligned}\tag{2.24}$$

$$\begin{aligned}\mathbf{A}_H \tilde{\mathbf{h}}_z &= 0 \\ \mathbf{A}_H &= \mathbf{D}_{x'}^e \boldsymbol{\varepsilon}_{yy}^{-1} \mathbf{D}_{x'}^h + \mathbf{D}_{y'}^e \boldsymbol{\varepsilon}_{xx}^{-1} \mathbf{D}_{y'}^h + \boldsymbol{\mu}_{zz}\end{aligned}\tag{2.25}$$

The above equations only provide a trivial solution, however. To obtain a meaningful result, a source must be incorporated. The convention from here on follows the E-mode.

$$\mathbf{A}_E \mathbf{e}_z = \mathbf{b} \quad (2.26)$$

From this equation, the field solution can be calculated as

$$\mathbf{e}_z = \mathbf{A}_E^{-1} \mathbf{b} \quad (2.27)$$

To implement a source, this text uses the total-field/scattered-field (TF/SF) technique for incorporating a source [26]. The TF/SF technique is useful for separating reflected waves from the total field quantities. It consists of a grid of two separate regions, denoting the total-field and the scattered-field regions. From this, a masking matrix  $\mathbf{Q}$  that is compatible with the finite-difference framework is constructed to represent it. The grid separating the TF/SF and the masking matrix  $\mathbf{Q}$  for a  $2 \times 2$  case created from it are displayed below.  $N_x, N_y$  denote grid points along the  $x$ - and  $y$ -axis, respectively. The original entries of this specific example of a  $\mathbf{Q}$ -matrix are colored red to distinguish from the sparse 0's.

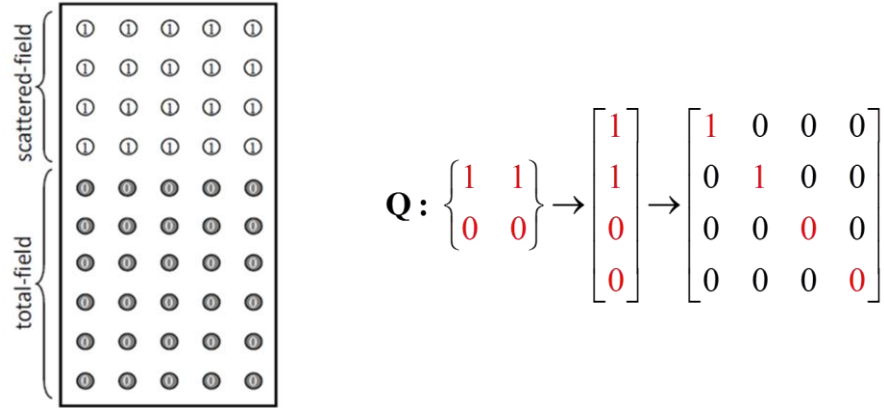


Figure 2.6: Constructing the  $\mathbf{Q}$  matrix for the total-field/scattered-field technique.

The TF/SF technique produces a modified source vector [26], Eq. (2.28), which combines the wave matrix, the original source vector, and the  $\mathbf{Q}$ -matrix to separate the total and reflected fields.

$$\mathbf{b} = (\mathbf{Q}\mathbf{A}_E - \mathbf{A}_E\mathbf{Q})\mathbf{f}_{\text{src}}, \quad (2.28)$$

where  $\mathbf{f}_{src}$  is defined as if it exists in a completely homogeneous grid (e.g. a plane-wave) where the material properties are set to values equal to those where the source is injected.

The field quantity is now calculated as

$$\mathbf{e}_z = \mathbf{A}_E^{-1} \mathbf{b} \quad (2.29)$$

## 2.3 PLANE WAVE EXPANSION METHOD

The plane wave expansion method (PWEM) is based on an expansion of the fields into a plane wave basis. Like the FDFD method, it is a stable and rigorous method, as no approximations are made to Maxwell's equations other than the truncation of plane waves used to represent the fields. It is most often used to analyze dielectric periodic structures like photonic crystals. Because the electromagnetic fields inside periodic structures like photonic crystals take on the (periodic) form of their (periodic) hosts, they can be expressed by Bloch waves [29]. This allows for a complete analysis by studying only a single unit cell of the photonic crystal (with appropriate Bloch boundary conditions).

### 2.3.1 Reciprocal Lattice Vectors

A three-dimensional periodic function  $f(x, y, z)$  can be analyzed by taking its Fourier transform. The expansion is as follows:

$$f(x, y, z) = \sum_{p=-\infty}^{\infty} \sum_{q=-\infty}^{\infty} \sum_{r=-\infty}^{\infty} a_{p,q,r} e^{j\left(\frac{2\pi p}{\Lambda_x}x + \frac{2\pi q}{\Lambda_y}y + \frac{2\pi r}{\Lambda_z}z\right)} \quad (2.30)$$

$$a_{p,q,r} = \frac{1}{V} \iiint_V f(x, y, z) e^{-j\left(\frac{2\pi p}{\Lambda_x}x + \frac{2\pi q}{\Lambda_y}y + \frac{2\pi r}{\Lambda_z}z\right)} dV$$

where  $p$ ,  $q$ , and  $r$  are integer numbers representing the current spatial harmonics along the  $x$ ,  $y$ , and  $z$  directions, respectively. Eq. (2.30) can be written in terms of the lattice's reciprocal lattice vectors. In the case of orthorhombic symmetries in three dimensions [30], the reciprocal lattice vectors are defined as:

$$\begin{aligned}
\vec{T}_1 &= \frac{2\pi}{\Lambda_x} \hat{x} \\
\vec{T}_2 &= \frac{2\pi}{\Lambda_y} \hat{y} \\
\vec{T}_3 &= \frac{2\pi}{\Lambda_z} \hat{z}
\end{aligned} \tag{2.31}$$

Writing the Fourier expansions of Eq. (2.30) in terms of the reciprocal lattice vectors yields

$$\begin{aligned}
f(x, y, z) &= \sum_{p=-\infty}^{\infty} \sum_{q=-\infty}^{\infty} \sum_{r=-\infty}^{\infty} a_{p,q,r} e^{j(p\vec{T}_1 + q\vec{T}_2 + r\vec{T}_3) \cdot \vec{r}} \\
a_{p,q,r} &= \frac{1}{V} \iiint_V f(x, y, z) e^{-j(p\vec{T}_1 + q\vec{T}_2 + r\vec{T}_3) \cdot \vec{r}} dV
\end{aligned} \tag{2.32}$$

where a three-dimensional position vector  $\vec{r}$  was introduced (not to be confused with the spatial harmonic index  $r$ ).

### 2.3.2 Fourier Space

Devices that are infinitely periodic in all directions can be analyzed through a Fourier transform. The Fourier expansions of the permittivity and permeability functions materials are:

$$\begin{aligned}
\varepsilon_r(\vec{r}) &= \sum_{p=-\infty}^{\infty} \sum_{q=-\infty}^{\infty} \sum_{r=-\infty}^{\infty} a_{p,q,r} e^{j(p\vec{T}_1 + q\vec{T}_2 + r\vec{T}_3) \cdot \vec{r}} \\
a_{p,q,r} &= \frac{1}{V} \iiint_V \varepsilon_r(\vec{r}) e^{-j(p\vec{T}_1 + q\vec{T}_2 + r\vec{T}_3) \cdot \vec{r}} dV
\end{aligned} \tag{2.33}$$

$$\begin{aligned}
\mu_r(\vec{r}) &= \sum_{p=-\infty}^{\infty} \sum_{q=-\infty}^{\infty} \sum_{r=-\infty}^{\infty} b_{p,q,r} e^{j(p\vec{T}_1 + q\vec{T}_2 + r\vec{T}_3) \cdot \vec{r}} \\
b_{p,q,r} &= \frac{1}{V} \iiint_V \mu_r(\vec{r}) e^{-j(p\vec{T}_1 + q\vec{T}_2 + r\vec{T}_3) \cdot \vec{r}} dV
\end{aligned} \tag{2.34}$$

The Fourier expansions of the field quantities are slightly different due to the fact that the fields in a photonic crystal take on the form of Bloch waves [30]. In addition to the plane-wave basis that the Fourier expansion results in, there is a periodic function (envelope) that modulates the

plane-waves in accordance with the periodicity of the lattice. The field expansions take on the following form:

$$\vec{E}(\vec{r}) = e^{-j\vec{\beta} \cdot \vec{r}} \sum_{p=-\infty}^{\infty} \sum_{q=-\infty}^{\infty} \sum_{r=-\infty}^{\infty} \vec{S}_{p,q,r} e^{j(p\vec{T}_1 + q\vec{T}_2 + r\vec{T}_3) \cdot \vec{r}} \quad (2.35)$$

$$\vec{H}(\vec{r}) = e^{-j\vec{\beta} \cdot \vec{r}} \sum_{p=-\infty}^{\infty} \sum_{q=-\infty}^{\infty} \sum_{r=-\infty}^{\infty} \vec{U}_{p,q,r} e^{j(p\vec{T}_1 + q\vec{T}_2 + r\vec{T}_3) \cdot \vec{r}} \quad (2.36)$$

Here, the crystal wave vector  $\vec{\beta}$  accounts for wave direction and magnitude in the lattice.

Combining the exponentials, we arrive at

$$\vec{E}(\vec{r}) = \sum_{p=-\infty}^{\infty} \sum_{q=-\infty}^{\infty} \sum_{r=-\infty}^{\infty} \vec{S}_{p,q,r} e^{-j(\vec{\beta} - p\vec{T}_1 - q\vec{T}_2 - r\vec{T}_3) \cdot \vec{r}} \quad (2.37)$$

$$\vec{H}(\vec{r}) = \sum_{p=-\infty}^{\infty} \sum_{q=-\infty}^{\infty} \sum_{r=-\infty}^{\infty} \vec{U}_{p,q,r} e^{-j(\vec{\beta} - p\vec{T}_1 - q\vec{T}_2 - r\vec{T}_3) \cdot \vec{r}} \quad (2.38)$$

The exponential terms are then combined to form new wave vectors, which are convenient for describing the wave behavior of these field quantities.

$$\vec{E}(\vec{r}) = \sum_{p=-\infty}^{\infty} \sum_{q=-\infty}^{\infty} \sum_{r=-\infty}^{\infty} \vec{S}_{p,q,r} e^{-j[\vec{k}(p,q,r)] \cdot \vec{r}} \quad (2.39)$$

$$\vec{H}(\vec{r}) = \sum_{p=-\infty}^{\infty} \sum_{q=-\infty}^{\infty} \sum_{r=-\infty}^{\infty} \vec{U}_{p,q,r} e^{-j[\vec{k}(p,q,r)] \cdot \vec{r}} \quad (2.40)$$

The wave vector and its components are now

$$\vec{k}(p, q, r) = \vec{\beta} - p\vec{T}_1 - q\vec{T}_2 - r\vec{T}_3 \quad (2.41)$$

$$\begin{aligned} k_x(p, q, r) &= \beta_x - pT_{1,x} - qT_{2,x} - rT_{3,x} \\ k_y(p, q, r) &= \beta_y - pT_{1,y} - qT_{2,y} - rT_{3,y} \\ k_z(p, q, r) &= \beta_z - pT_{1,z} - qT_{2,z} - rT_{3,z} \end{aligned} \quad (2.42)$$

Eq. (2.42) holds for general symmetries. For orthorhombic symmetries, including cubic, the component equations can be expressed in a reduced, clearer form:

$$\begin{aligned}
k_x(p) &= \beta_x - \frac{2\pi p}{\Lambda_x} \\
k_y(q) &= \beta_y - \frac{2\pi q}{\Lambda_y} \\
k_z(r) &= \beta_z - \frac{2\pi r}{\Lambda_z}
\end{aligned} \tag{2.43}$$

The notation  $k_x(p)$  indicates that, in this case, the  $x$ -component only varies with  $p$ , the  $y$ -component with  $q$ , and so forth; the array sizes remain a function of  $p$ ,  $q$ , and  $r$ , however.

The field expansions, finally, take on the following form:

$$\vec{E}(\vec{r}) = \sum_{p=-\infty}^{\infty} \sum_{q=-\infty}^{\infty} \sum_{r=-\infty}^{\infty} \vec{S}_{p,q,r} e^{-j[k_x(p)x + k_y(q)y + k_z(r)z]} \tag{2.44}$$

$$\vec{H}(\vec{r}) = \sum_{p=-\infty}^{\infty} \sum_{q=-\infty}^{\infty} \sum_{r=-\infty}^{\infty} \vec{U}_{p,q,r} e^{-j[k_x(p)x + k_y(q)y + k_z(r)z]} \tag{2.45}$$

### 2.3.3 Maxwell's Equations in Fourier Space

The field expansions of Eqs. (2.44)-(2.45) substitute into the original form of Maxwell's equations found in Eqs. (2.14)-(2.15). The process will be demonstrated with the first equation of Eq. (2.15), with color-coded field and material quantities for convenience:

$$\begin{aligned}
&\frac{\partial \tilde{H}_z}{\partial y} - \frac{\partial \tilde{H}_y}{\partial z} = k_0 \epsilon_r E_x \\
&\frac{\partial}{\partial y} \left[ \sum_{p=-\infty}^{\infty} \sum_{q=-\infty}^{\infty} \sum_{r=-\infty}^{\infty} U_z(p, q, r) e^{-j[k_x(p)x + k_y(q)y + k_z(r)z]} \right] - \\
&\frac{\partial}{\partial z} \left[ \sum_{p=-\infty}^{\infty} \sum_{q=-\infty}^{\infty} \sum_{r=-\infty}^{\infty} U_y(p, q, r) e^{-j[k_x(p)x + k_y(q)y + k_z(r)z]} \right] = \\
&k_0 \left[ \sum_{p=-\infty}^{\infty} \sum_{q=-\infty}^{\infty} \sum_{r=-\infty}^{\infty} a_{p,q,r} e^{j\left(\frac{2\pi p}{\Lambda_x}x + \frac{2\pi q}{\Lambda_y}y + \frac{2\pi r}{\Lambda_z}z\right)} \right] \left[ \sum_{p=-\infty}^{\infty} \sum_{q=-\infty}^{\infty} \sum_{r=-\infty}^{\infty} S_x(p, q, r) e^{-j[k_x(p)x + k_y(q)y + k_z(r)z]} \right]
\end{aligned} \tag{2.46}$$

The product of the two triple summations is handled by the Cauchy product [31] and results in

$$\sum_{p=-\infty}^{\infty} \sum_{q=-\infty}^{\infty} \sum_{r=-\infty}^{\infty} \left\{ e^{-j[k_x(p)x+k_y(q)y+k_z(r)z]} \sum_{p'=-\infty}^{\infty} \sum_{q'=-\infty}^{\infty} \sum_{r'=-\infty}^{\infty} a_{p-p',q-q',r-r'} S_x(p',q',r') \right\}, \quad (2.47)$$

where the shifted triple summation term is interpreted as a three-dimensional convolution in Fourier space.

Eq. (2.46) now becomes

$$\begin{aligned} & \sum_{p=-\infty}^{\infty} \sum_{q=-\infty}^{\infty} \sum_{r=-\infty}^{\infty} -jk_y(q)U_z(p,q,r)e^{-j[k_x(p)x+k_y(q)y+k_z(r)z]} + \\ & \sum_{p=-\infty}^{\infty} \sum_{q=-\infty}^{\infty} \sum_{r=-\infty}^{\infty} jk_z(r)U_y(p,q,r)e^{-j[k_x(p)x+k_y(q)y+k_z(r)z]} = \\ & k_0 \sum_{p=-\infty}^{\infty} \sum_{q=-\infty}^{\infty} \sum_{r=-\infty}^{\infty} \left\{ e^{-j[k_x(p)x+k_y(q)y+k_z(r)z]} \sum_{p'=-\infty}^{\infty} \sum_{q'=-\infty}^{\infty} \sum_{r'=-\infty}^{\infty} a_{p-p',q-q',r-r'} S_x(p',q',r') \right\} \end{aligned} \quad (2.48)$$

The entire equation can be brought inside a single triple summation, which means that every term in the equation inside must be satisfied for each combination of  $p$ ,  $q$ , and  $r$ . The resulting equation becomes

$$\begin{aligned} & -jk_y(q)U_z(p,q,r)e^{-j[k_x(p)x+k_y(q)y+k_z(r)z]} + jk_z(r)U_y(p,q,r)e^{-j[k_x(p)x+k_y(q)y+k_z(r)z]} \\ & = k_0 e^{-j[k_x(p)x+k_y(q)y+k_z(r)z]} \sum_{p'=-\infty}^{\infty} \sum_{q'=-\infty}^{\infty} \sum_{r'=-\infty}^{\infty} a_{p-p',q-q',r-r'} S_x(p',q',r') \end{aligned} \quad (2.49)$$

Finally, factoring out the common exponential term results in

$$-jk_y(q)U_z(p,q,r) + jk_z(r)U_y(p,q,r) = k_0 \sum_{p'=-\infty}^{\infty} \sum_{q'=-\infty}^{\infty} \sum_{r'=-\infty}^{\infty} a_{p-p',q-q',r-r'} S_x(p',q',r') \quad (2.50)$$

The process for the remaining equations is similar. Maxwell's equations of Eqs. (2.14)-(2.15), in Fourier Space, are expressed as follows:

$$\begin{aligned} & -jk_y(q)U_z(p,q,r) + jk_z(r)U_y(p,q,r) = k_0 \sum_{p'=-\infty}^{\infty} \sum_{q'=-\infty}^{\infty} \sum_{r'=-\infty}^{\infty} a_{p-p',q-q',r-r'} S_x(p',q',r') \\ & -jk_z(r)U_x(p,q,r) + jk_x(p)U_z(p,q,r) = k_0 \sum_{p'=-\infty}^{\infty} \sum_{q'=-\infty}^{\infty} \sum_{r'=-\infty}^{\infty} a_{p-p',q-q',r-r'} S_y(p',q',r') \\ & -jk_x(p)U_y(p,q,r) + jk_y(q)U_x(p,q,r) = k_0 \sum_{p'=-\infty}^{\infty} \sum_{q'=-\infty}^{\infty} \sum_{r'=-\infty}^{\infty} a_{p-p',q-q',r-r'} S_z(p',q',r') \end{aligned} \quad (2.51)$$

$$\begin{aligned}
-jk_y(q)S_z(p, q, r) + jk_z(r)S_y(p, q, r) &= k_0 \sum_{p'=-\infty}^{\infty} \sum_{q'=-\infty}^{\infty} \sum_{r'=-\infty}^{\infty} b_{p-p', q-q', r-r'} U_x(p', q', r') \\
-jk_z(r)S_x(p, q, r) + jk_x(p)S_z(p, q, r) &= k_0 \sum_{p'=-\infty}^{\infty} \sum_{q'=-\infty}^{\infty} \sum_{r'=-\infty}^{\infty} b_{p-p', q-q', r-r'} U_y(p', q', r') \quad (2.52) \\
-jk_x(p)S_y(p, q, r) + jk_y(q)S_x(p, q, r) &= k_0 \sum_{p'=-\infty}^{\infty} \sum_{q'=-\infty}^{\infty} \sum_{r'=-\infty}^{\infty} b_{p-p', q-q', r-r'} U_z(p', q', r')
\end{aligned}$$

Multiplying by  $j$  across each equation yields

$$\begin{aligned}
k_y(q)U_z(p, q, r) - k_z(r)U_y(p, q, r) &= jk_0 \sum_{p'=-\infty}^{\infty} \sum_{q'=-\infty}^{\infty} \sum_{r'=-\infty}^{\infty} a_{p-p', q-q', r-r'} S_x(p', q', r') \\
k_z(r)U_x(p, q, r) - k_x(p)U_z(p, q, r) &= jk_0 \sum_{p'=-\infty}^{\infty} \sum_{q'=-\infty}^{\infty} \sum_{r'=-\infty}^{\infty} a_{p-p', q-q', r-r'} S_y(p', q', r') \quad (2.53) \\
k_x(p)U_y(p, q, r) - k_y(q)U_x(p, q, r) &= jk_0 \sum_{p'=-\infty}^{\infty} \sum_{q'=-\infty}^{\infty} \sum_{r'=-\infty}^{\infty} a_{p-p', q-q', r-r'} S_z(p', q', r') \\
k_y(q)S_z(p, q, r) - k_z(r)S_y(p, q, r) &= jk_0 \sum_{p'=-\infty}^{\infty} \sum_{q'=-\infty}^{\infty} \sum_{r'=-\infty}^{\infty} b_{p-p', q-q', r-r'} U_x(p', q', r') \\
k_z(r)S_x(p, q, r) - k_x(p)S_z(p, q, r) &= jk_0 \sum_{p'=-\infty}^{\infty} \sum_{q'=-\infty}^{\infty} \sum_{r'=-\infty}^{\infty} b_{p-p', q-q', r-r'} U_y(p', q', r') \quad (2.54) \\
k_x(p)S_y(p, q, r) - k_y(q)S_x(p, q, r) &= jk_0 \sum_{p'=-\infty}^{\infty} \sum_{q'=-\infty}^{\infty} \sum_{r'=-\infty}^{\infty} b_{p-p', q-q', r-r'} U_z(p', q', r')
\end{aligned}$$

Each of these equations is written once for every combination of  $p$ ,  $q$ , and  $r$  retained in the plane wave expansion. These large sets of equations can be written in matrix form as [11]

$$\begin{aligned}
\mathbf{K}_y \mathbf{u}_z - \mathbf{K}_z \mathbf{u}_y &= jk_0 \boldsymbol{\epsilon}_r \mathbf{s}_x \\
\mathbf{K}_z \mathbf{u}_x - \mathbf{K}_x \mathbf{u}_z &= jk_0 \boldsymbol{\epsilon}_r \mathbf{s}_y \\
\mathbf{K}_x \mathbf{u}_y - \mathbf{K}_y \mathbf{u}_x &= jk_0 \boldsymbol{\epsilon}_r \mathbf{s}_z
\end{aligned} \quad (2.55)$$

$$\begin{aligned}
\mathbf{K}_y \mathbf{s}_z - \mathbf{K}_z \mathbf{s}_y &= jk_0 \boldsymbol{\mu}_r \mathbf{u}_x \\
\mathbf{K}_z \mathbf{s}_x - \mathbf{K}_x \mathbf{s}_z &= jk_0 \boldsymbol{\mu}_r \mathbf{u}_y \\
\mathbf{K}_x \mathbf{s}_y - \mathbf{K}_y \mathbf{s}_x &= jk_0 \boldsymbol{\mu}_r \mathbf{u}_z
\end{aligned} \quad (2.56)$$

The terms  $\mathbf{K}_x$ ,  $\mathbf{K}_y$ , and  $\mathbf{K}_z$  are diagonal matrices containing all the values of  $k_x(p, q, r)$ ,  $k_y(p, q, r)$ , and  $k_z(p, q, r)$ , respectively, along their diagonals. The column vectors

$\mathbf{s}_x, \mathbf{s}_y$ , and  $\mathbf{s}_z$  contain the amplitude coefficients of the electric field component of the spatial harmonics. Similarly,  $\mathbf{u}_x, \mathbf{u}_y$ , and  $\mathbf{u}_z$  are column vectors containing the magnetic field component of the spatial harmonics. The constitutive terms  $\boldsymbol{\epsilon}_r$  and  $\boldsymbol{\mu}_r$  are square matrices are embedded with a convolution in Fourier space, according to the terms on the right side of Eqs. (2.53)-(2.54).

$$\begin{aligned}
& \sum_{p'=-\infty}^{\infty} \sum_{q'=-\infty}^{\infty} \sum_{r'=-\infty}^{\infty} a_{p-p', q-q', r-r'} S_x(p', q', r') \\
& \quad \downarrow \\
& \quad \boldsymbol{\epsilon}_r * S_x \\
& \quad \downarrow \\
& \quad \boldsymbol{\epsilon}_r \mathbf{s}_x
\end{aligned} \tag{2.57}$$

This notation implies  $\boldsymbol{\epsilon}_r = \text{FT}[\boldsymbol{\epsilon}_r *]$  and  $\boldsymbol{\mu}_r = \text{FT}[\boldsymbol{\mu}_r *]$ .

### 2.3.4 PWEM Formulation

#### *Formulation in Three Dimensions*

The set of Maxwell's equations in Fourier space of Eqs. (2.55)-(2.56) can be written in block matrix form as

$$\begin{bmatrix} \mathbf{0} & -\mathbf{K}_z & \mathbf{K}_y \\ \mathbf{K}_z & \mathbf{0} & -\mathbf{K}_x \\ -\mathbf{K}_y & \mathbf{K}_x & \mathbf{0} \end{bmatrix} \begin{bmatrix} \mathbf{u}_x \\ \mathbf{u}_y \\ \mathbf{u}_z \end{bmatrix} = jk_0 \begin{bmatrix} \boldsymbol{\epsilon}_r & \mathbf{0} & \mathbf{0} \\ \mathbf{0} & \boldsymbol{\epsilon}_r & \mathbf{0} \\ \mathbf{0} & \mathbf{0} & \boldsymbol{\epsilon}_r \end{bmatrix} \begin{bmatrix} \mathbf{s}_x \\ \mathbf{s}_y \\ \mathbf{s}_z \end{bmatrix} \tag{2.58}$$

$$\begin{bmatrix} \mathbf{0} & -\mathbf{K}_z & \mathbf{K}_y \\ \mathbf{K}_z & \mathbf{0} & -\mathbf{K}_x \\ -\mathbf{K}_y & \mathbf{K}_x & \mathbf{0} \end{bmatrix} \begin{bmatrix} \mathbf{s}_x \\ \mathbf{s}_y \\ \mathbf{s}_z \end{bmatrix} = jk_0 \begin{bmatrix} \boldsymbol{\mu}_r & \mathbf{0} & \mathbf{0} \\ \mathbf{0} & \boldsymbol{\mu}_r & \mathbf{0} \\ \mathbf{0} & \mathbf{0} & \boldsymbol{\mu}_r \end{bmatrix} \begin{bmatrix} \mathbf{u}_x \\ \mathbf{u}_y \\ \mathbf{u}_z \end{bmatrix} \tag{2.59}$$

The same equations are more compactly written as

$$[\vec{\mathbf{K}} \times] \vec{\mathbf{u}} = jk_0 [\boldsymbol{\epsilon}_r] \vec{\mathbf{s}} \tag{2.60}$$

$$[\vec{\mathbf{K}} \times] \vec{\mathbf{s}} = jk_0 [\boldsymbol{\mu}_r] \vec{\mathbf{u}} , \tag{2.61}$$

where  $\left[\vec{\mathbf{K}} \times\right]$  is the notation used for a cross product in three dimensions performed by the  $\mathbf{K}_x, \mathbf{K}_y$ , and  $\mathbf{K}_z$  matrices. Solving for  $\vec{\mathbf{u}}$  in Eq. (2.61) and substituting into Eq. (2.60) yields

$$\left[\vec{\mathbf{K}} \times\right]\left[\boldsymbol{\mu}_r\right]^{-1}\left[\vec{\mathbf{K}} \times\right] \vec{\mathbf{s}}=-k_0^2\left[\boldsymbol{\epsilon}_r\right] \vec{\mathbf{s}} \quad (2.62)$$

Eq. (2.62) takes on the form of a generalized eigenvalue problem  $\mathbf{Ax} = \lambda \mathbf{Bx}$ , where  $k_0$  (frequency) is the eigenvalue; this constitutes the general equation for the solution of a three-dimensional plane wave expansion method.

### ***Formulation in Two Dimensions***

Periodic structures (e.g. photonic crystals) can often be accurately analyzed through a two-dimensional model. They commonly have a defined plane of periodicity while being uniform (extruded) along the third dimension. Therefore, if propagation is restricted to the plane of periodicity ( $x$ - $y$  plane for convenience), the wave vector components along the third dimension cancel to zero ( $\mathbf{K}_z = \mathbf{0}$ ). In two-dimensions, Maxwell's equations of Eqs. (2.55)-(2.56) become

$$\begin{aligned} \mathbf{K}_y \mathbf{u}_z &= jk_0 \boldsymbol{\epsilon}_r \mathbf{s}_x \\ -\mathbf{K}_x \mathbf{u}_z &= jk_0 \boldsymbol{\epsilon}_r \mathbf{s}_y \\ \mathbf{K}_x \mathbf{u}_y - \mathbf{K}_y \mathbf{u}_x &= jk_0 \boldsymbol{\epsilon}_r \mathbf{s}_z \end{aligned} \quad (2.63)$$

$$\begin{aligned} \mathbf{K}_y \mathbf{s}_z &= jk_0 \boldsymbol{\mu}_r \mathbf{u}_x \\ -\mathbf{K}_x \mathbf{s}_z &= jk_0 \boldsymbol{\mu}_r \mathbf{u}_y \\ \mathbf{K}_x \mathbf{s}_y - \mathbf{K}_y \mathbf{s}_x &= jk_0 \boldsymbol{\mu}_r \mathbf{u}_z \end{aligned} \quad (2.64)$$

These six equations have separated into two distinct modes: The TM mode, where the electric field is perpendicular to the plane of periodicity ( $E_z$ )

$$\begin{aligned} \mathbf{K}_x \mathbf{u}_y - \mathbf{K}_y \mathbf{u}_x &= jk_0 \boldsymbol{\epsilon}_r \mathbf{s}_z \\ \mathbf{K}_y \mathbf{s}_z &= jk_0 \boldsymbol{\mu}_r \mathbf{u}_x, \\ -\mathbf{K}_x \mathbf{s}_z &= jk_0 \boldsymbol{\mu}_r \mathbf{u}_y \end{aligned} \quad (2.65)$$

and the TE mode, where the magnetic field is perpendicular to the plane of periodicity ( $H_z$ ).

$$\begin{aligned}
\mathbf{K}_x \mathbf{s}_y - \mathbf{K}_y \mathbf{s}_x &= j k_0 \boldsymbol{\mu}_r \mathbf{u}_z \\
\mathbf{K}_y \mathbf{u}_z &= j k_0 \boldsymbol{\epsilon}_r \mathbf{s}_x \\
-\mathbf{K}_x \mathbf{u}_z &= j k_0 \boldsymbol{\epsilon}_r \mathbf{s}_y
\end{aligned} \tag{2.66}$$

From each mode, an eigen-value problem for two-dimensional devices can be derived. The TM mode eigenvalue problem follows as

$$\begin{aligned}
\mathbf{u}_x &= -\frac{j}{k_0} \boldsymbol{\mu}_r^{-1} \mathbf{K}_y \mathbf{s}_z \\
\mathbf{u}_y &= \frac{j}{k_0} \boldsymbol{\mu}_r^{-1} \mathbf{K}_x \mathbf{s}_z \\
&\downarrow \\
\boxed{(\mathbf{K}_x \boldsymbol{\mu}_r^{-1} \mathbf{K}_x + \mathbf{K}_y \boldsymbol{\mu}_r^{-1} \mathbf{K}_y) \mathbf{s}_z = k_0^2 \boldsymbol{\epsilon}_r \mathbf{s}_z}
\end{aligned} \tag{2.67}$$

The TE mode eigen-value problem is expressed as

$$\begin{aligned}
\mathbf{s}_x &= -\frac{j}{k_0} \boldsymbol{\epsilon}_r^{-1} \mathbf{K}_y \mathbf{u}_z \\
\mathbf{s}_y &= \frac{j}{k_0} \boldsymbol{\epsilon}_r^{-1} \mathbf{K}_x \mathbf{u}_z \\
&\downarrow \\
\boxed{(\mathbf{K}_x \boldsymbol{\epsilon}_r^{-1} \mathbf{K}_x + \mathbf{K}_y \boldsymbol{\epsilon}_r^{-1} \mathbf{K}_y) \mathbf{u}_z = k_0^2 \boldsymbol{\mu}_r \mathbf{u}_z}
\end{aligned} \tag{2.68}$$

These equations are in the form of a generalized eigen-value problem. The solutions (eigenvalues) are frequencies in the form of  $k_0^2$ .

## Chapter 3: Photonic Crystals

The analysis of photonic crystals largely follows methods analogous to those used in solid state theory [29, 32]. In solid state physics, “crystal” is the name given to a material composed of a periodic arrangement of atomic particles such as atoms or molecules. Electrons in this media experience a periodic potential which, along with the material properties and their geometry, mandates their propagating behavior. The mathematical equation describing their motion in this context is the Schrodinger equation, where it is observed that electrons take on a wave nature. In the macroscopic realm, photonic crystal lattices take on the form of dielectric distributions with periodically alternating material parameters. Here, it is instead photons experiencing a periodic index of refraction, and their wave behavior/displacement can be predicted with a similarly structured equation. These structures are called photonic crystals (PCs).

One- and two-dimensional photonic crystals are the recipients of much of the attention due to their ease of simulation and fabrication. Moreover, the extrusion along the third dimension that 2D models imply has proven to be not a limitation but a breeding ground for novel, unexpected devices [33-48], which continue to spring up as state-of-the-art (largely in addition to inexpensive computations).

### 3.1 MATHEMATICAL FRAMEWORK

The mathematical framework for analyzing photonic crystals is analogous to that of atomic crystals. Along with Maxwell’s equations to describe classical electromagnetic behavior, a framework for modeling photonic crystals becomes possible.

#### 3.1.1 Maxwell’s Equations for Photonic Crystals

In this work, the photonic crystal lattices under analysis are assumed to reside in a source-free, charge-free, divergence-free space. These approximations are strengthened by the fact that these lattices are composed completely of dielectric material in air; this is in contrast to metals, where surface currents and similar phenomena are difficult to ignore. Also, because the

steady state behavior is of interest, it is convenient to consider the frequency-domain form of Maxwell's equations. Eq. (3.1) reflects Maxwell's equations under these circumstances.

$$\begin{aligned}
\nabla \cdot \vec{D} &= 0 \\
\nabla \cdot \vec{B} &= 0 \\
\nabla \times \vec{E} &= -j\omega\vec{B} \\
\nabla \times \vec{H} &= j\omega\vec{D}
\end{aligned} \tag{3.1}$$

All media will be considered linear and isotropic. These approximations are appropriate when working with ordinary materials at low energy levels. Maxwell's curl equations are then expressed with their constitutive parameters reflecting these circumstances.

$$\begin{aligned}
\nabla \times \vec{E} &= -j\omega\mu(\vec{r})\vec{H} \\
\nabla \times \vec{H} &= j\omega\varepsilon(\vec{r})\vec{E}
\end{aligned} \tag{3.2}$$

Here it is possible to arrange the equations to isolate the field quantities.

$$\begin{aligned}
\vec{H} &= -\frac{1}{j\omega\mu(\vec{r})}\nabla \times \vec{E} \\
\vec{E} &= \frac{1}{j\omega\varepsilon(\vec{r})}\nabla \times \vec{H}
\end{aligned} \tag{3.3}$$

Waves are a consequence of the coupling between electric and magnetic fields. It is the interaction of these two which describes and predicts wave propagation; it therefore makes sense to combine the equations for both. They can be combined and arranged to express either electric or magnetic field quantities.

$$\nabla \times \frac{1}{\mu(\vec{r})}\nabla \times \vec{E} = \omega^2\varepsilon(\vec{r})\vec{E} \tag{3.4}$$

$$\nabla \times \frac{1}{\varepsilon(\vec{r})}\nabla \times \vec{H} = \omega^2\mu(\vec{r})\vec{H} \tag{3.5}$$

In the context of wave propagation, it is convenient to express the equations in terms of the free space wave number  $k_0 = \omega/c$ , recalling that the speed of light may be expressed in terms of the

free space permeability and permittivity  $c = 1/\sqrt{\mu_0 \epsilon_0}$ , and the notation for relative material parameters. This substitution expresses the wave behavior in terms of the relative material parameters. This substitution expresses the wave behavior in terms of the relative material parameters. Eqs. (3.4) & (3.5) now become

$$\nabla \times \frac{1}{\mu_r(\vec{r})} \nabla \times \vec{E} = k_0^2 \epsilon_r(\vec{r}) \vec{E} \quad (3.6)$$

$$\nabla \times \frac{1}{\epsilon_r(\vec{r})} \nabla \times \vec{H} = k_0^2 \mu_r(\vec{r}) \vec{H} \quad (3.7)$$

These wave equations take on the form of a generalized eigenvalue problem  $\mathbf{Ax} = \lambda \mathbf{Bx}$ , where the eigenvalues represent sets of frequencies and the eigenvectors their corresponding modal profiles.

Photonic crystals are periodic, so the eigenvalue problem results in discrete solutions. Additionally, the modes of the system will obey the Bloch-Floquet theorem.

$$\vec{H} = e^{j(\vec{k} \cdot \vec{r})} \vec{H}_{\vec{k}} \quad (3.8)$$

The theorem describes the mode as essentially a plane-wave modulated with a periodic envelope; it is this envelope that takes on the periodicity of the crystal.

## 3.2 BAND GAPS

### 3.2.1 Band Diagrams

The solutions to the eigen-value problems of Eqs. (3.6)-(3.7) are eigenfrequencies, which are often plotted as a function of wave vectors to describe the crystal's electromagnetic properties. These wave vectors are typically made to march along the perimeter of the irreducible Brillouin zone (IBZ) [49], which occupies the minimum area needed to fully exploit the symmetry of the unit cell in reciprocal space. This process of plotting the eigenfrequencies as a function of the wave vector marching along the IBZ produce dispersion diagrams, or band diagrams. These diagrams are maps of the eigenstates, or frequencies, allowed to propagate

within the photonic crystal with the corresponding wave vector [29]. Analysis along the key points of symmetry revealed by the Brillouin zone also allows for optimized algorithms that can, for instance, use a reduced set of eigenfunctions for a faster computation of these band structures [50].

Band diagrams are an efficient but incomplete method for analyzing photonic crystals. These maps, however, are enough to determine the existence of important phenomena such as band gaps [3, 29, 30, 32].

### 3.2.2 Band Gaps in Photonic Crystals

Figure 3.1 shows the band diagram for a two-dimensional unit cell of square symmetry. The unit cell is composed of an air background with centered rods of refractive index  $n = 2.5$  and radius  $r = 0.2a$ .

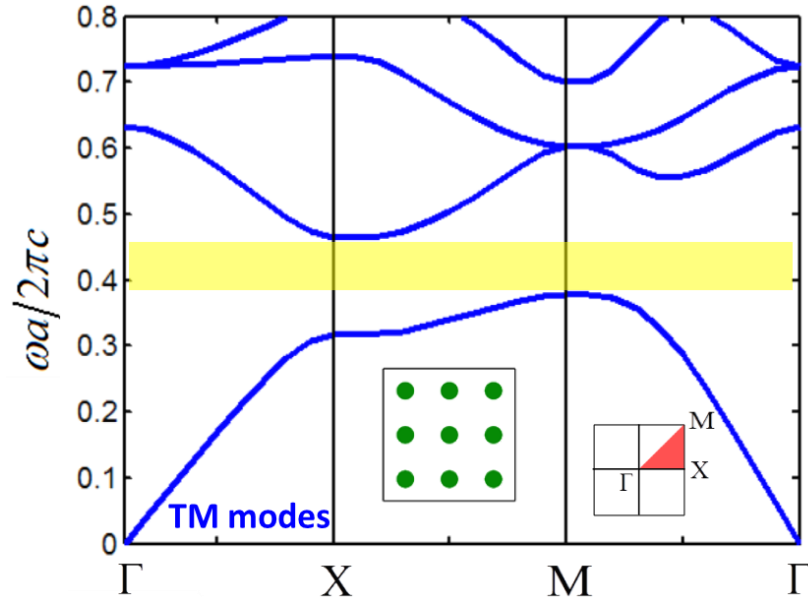


Figure 3.1: Band diagram showing the TM modes for a photonic crystal of dielectric rods in air background. The rods have a refractive index  $n = 2.5$  and radius  $r = 0.2a$ . The band gap frequency range is highlighted in yellow.

The eigenfrequencies are typically presented as values normalized to the wavelength, where  $\omega a / 2\pi c = a / \lambda_0$ . This step allows the quick and direct correlating of device dimensions to

operating frequencies. Of interest in this example is the normalized frequency range of  $0.378 < \omega a / 2\pi c < 0.464$ , where it can be seen that no allowed eigenstates exist between these frequencies at any wave vector configuration (for TM polarization). This phenomenon leads to photonic band gaps, where propagation is forbidden anywhere in the photonic crystal.

A photonic crystal is said to have a complete photonic bandgap only in the range of frequencies where both TM and TE polarizations exhibit a band gap in a full 3D simulation. However, for photonic crystals with planar periodicity, often called planar photonic crystals, a two-dimensional band gap analysis is sufficient to determine their existence.

Band gaps are an important phenomena, as many applications can exploit frequencies of forbidden propagation. One example is a photonic crystal waveguide based on band gaps. Because no propagation is allowed in the photonic crystal within the band gap frequency range, introducing a point defect (removing one unit cell) or a line defect (removing a row of unit cells) can serve as a guiding mechanism for electromagnetic waves. More details on these band gap waveguides will be explored in Chapter 6.

### **3.3 SELF-COLLIMATION**

#### **3.3.1 Dispersion Surfaces**

Although band diagrams offer a simple and effective means to characterize photonic crystals, they are not sufficient to indicate the presence of other useful effects based on dispersion. These effects are generally a consequence of the shape of their dispersion surfaces, as these reveal important parameters such as group velocity, from which parameters like direction of propagation can be inferred. The dispersion surfaces are, just like band diagrams, maps of the allowed eigenfrequencies as a function of the wave vector. The wave vector, however, now scans the entire Brillouin zone, producing a map of sheets rather than bands when analyzing a two-dimensional photonic crystal. An example set of dispersion surfaces is shown on Figure 3.2 (a) [11] below.

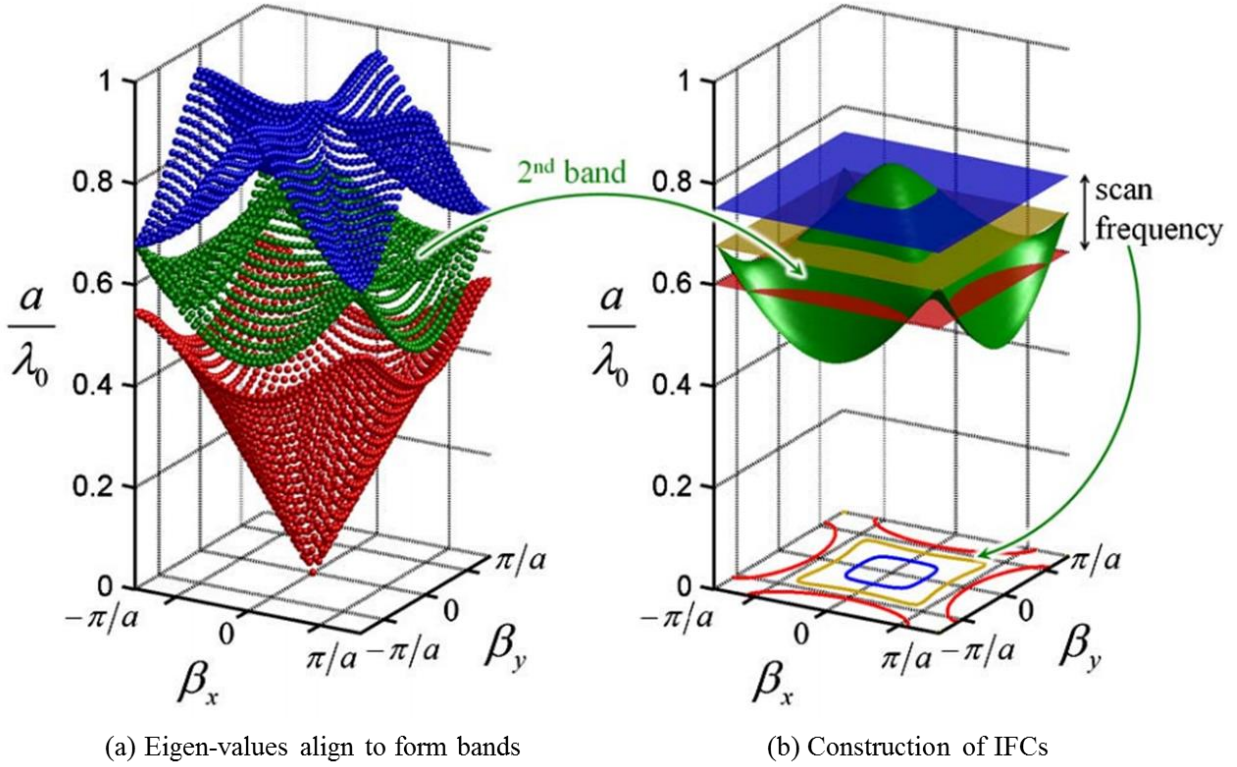


Figure 3.2 [11]: A (a) map of dispersion surfaces for a square photonic crystal and (b) the process of extracting its isofrequency contours.

### 3.3.2 Self-Collimation in Photonic Crystals

Of particular interest is the shape of the diagrams' isofrequency contours (IFCs), a set of contours formed at intersections of a band and a constant-frequency plane [11]. The shape of these contours is important because it reveals important wave parameters such as the direction of propagation. Because group velocity can be deduced from the shape of these maps, it follows that the direction of energy propagation lies in a direction normal to the isofrequency contour. The process of obtaining these isofrequency contours from dispersion diagrams is shown on Figure 3.2 (b).

One important consequence of this type of dispersion engineering is self-collimation, a mechanism that forces a beam of specific frequencies to propagate along the lattice without scattering or dispersion [7-13, 51]. Self-collimation occurs at frequencies which correspond to flat isocontours, as beams of a certain range of incident angle will be forced to propagate normal

to it, becoming a collimated beam and avoiding spreading. Figure 3.3 (a) shows how a beam of a specific range of angular incidence is collimated when the lattice operates under the self-collimation effect. When the isofrequency contour has flat facets, or is square, as is more often the case, the beam propagates without diffraction and is forced to flow in a direction relative to the principal axes of the unit cell. Figure 3.3 (b) [52] shows an example of the self-collimation effect acting on an incoming, diverging beam. Self-collimation is an attractive phenomena for devices because they can be monolithic, all-dielectric, and composed of only ordinary isotropic materials.

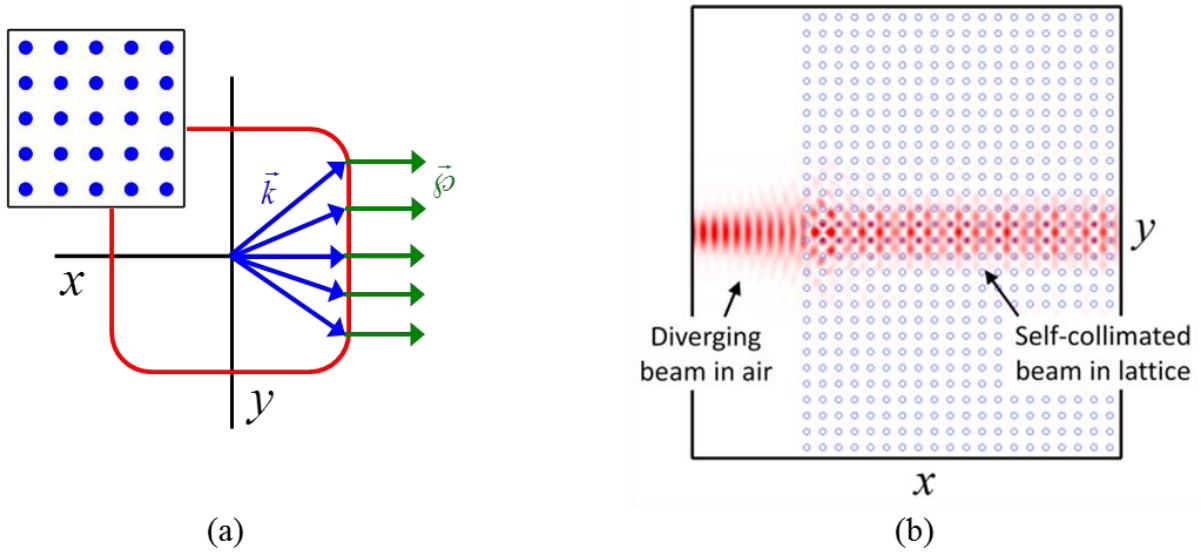


Figure 3.3 [52]: A (a) square isofrequency contour and its effect on energy propagation, and (b) self-collimation observed in a lattice. A diverging beam is collimated in the lattice and is forced to propagate without scattering or diffraction.

### 3.3.3 Optimization of the Self-Collimation Effect

Self-collimation in photonic crystals has received a lot of attention in the literature, partly due to recent interest in silicon photonics, yet no performance metrics have been proposed. This work presents a proposed figure of merit (FOM) for the self-collimation effect and outlines a methodical approach for calculating it [11]. Performance metrics include bandwidth, angular acceptance, a “strength” factor, and an overall FOM. Two key contributions of this work include

the performance metrics and identifying that the optimum frequency for the self-collimation effect is not necessarily at the inflection point.

The FOM is used to optimize a planar photonic crystal composed of a square array of cylinders. Conclusions are drawn about how the refractive indices and fill fraction of the lattice impact each of the performance metrics. The optimization is demonstrated by simulating two spatially variant self-collimating photonic crystals, where one has a high FOM and the other a low one. This work should provide optical designers tremendous insight into how to design and optimize robust self-collimating photonic crystals, which promise many applications in silicon photonics and integrated optics.

### ***Performance Metrics for Self-Collimation***

When the isofrequency contours are flat over some span of wave vectors, beams contained within this angular spectrum propagate without diffraction because all of their power is forced to propagate in a single direction. For a beam traveling in the  $+x$  direction, a “region of self-collimation” is defined as the area in  $k$  space where the slopes of the isofrequency contours remain vertical to within a sufficiently small angle threshold. This region is highlighted in Figure 3.4 [11] and resembles the back of a dolphin (for square unit cells of rods of varying fill fractions).

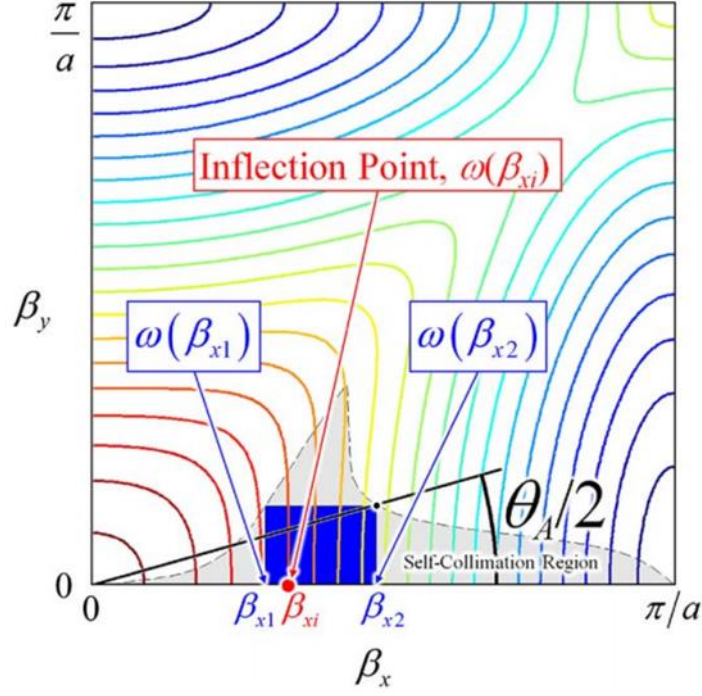


Figure 3.4 [11]: Determining the performance metrics for the self-collimation effect. Only the upper right quadrant of the Brillouin zone is shown here.

Experience has shown that a threshold angle of  $4^\circ$  works well. The angle  $\phi$  of the isofrequency contours is calculated from the gradient of the frequency  $\omega$  in  $k$ -space according to

$$\phi = \tan^{-1} \frac{\partial \omega / \partial \beta_y}{\partial \omega / \partial \beta_x} \quad (3.9)$$

The inflection point  $\beta_{xi}$  is identified as the point along the horizontal axis where the curvature of the IFC is zero. This can be interpreted as the point of maximum “flatness” and is also identified in Figure 3.4.

The figure of merit for the self-collimation effect is now defined. Three important considerations were identified to accomplish this. These are (1) the fractional bandwidth (FBW), (2) the acceptance angle  $\theta_A$ , and (3) the strength  $S$ . First, numerically find the largest possible rectangle that fits within the region of self-collimation. This rectangle is shown in Figure 3.4. Second, the FBW and acceptance angle are calculated from this rectangle. The FBW is calculated from the frequencies associated with the left and right edges according to

$$\text{FBW} = 2 \frac{\omega(\beta_{x2}) - \omega(\beta_{x1})}{\omega(\beta_{x2}) + \omega(\beta_{x1})} \quad (3.10)$$

Next, the acceptance angle  $\theta_A$  is defined to be the largest span of angles that falls entirely inside the rectangle. This is the angle of the line extending from the origin to the upper right corner of the rectangle relative to the horizontal axis. This angle is divided by  $180^\circ$  to normalize it:

$$\theta_A = \frac{\tan^{-1}(\beta_{y2}/\beta_{x2})}{90^\circ} \quad (3.11)$$

The area of this rectangle is not defined as simply the product of its width and height because this has little meaning in terms of what is physically important: bandwidth and acceptance angle. Instead, the “area” of the rectangle is defined as

$$A' = \text{FBW} \cdot \theta_A \quad (3.12)$$

This definition for area was used in this work to find the largest rectangle within the region of self-collimation. It is entirely possible that some applications may favor acceptance angle over bandwidth, or vice versa. In this case, the terms can be individually weighted in a number of different ways, such as through exponential or logarithmic functions.

During this investigation, it was found that photonic crystals with extremely low dielectric contrast still exhibited reasonable FBW and acceptance angle; however, these lattices required having many hundreds of unit cells before the self-collimation effect could be observed. From this observation, a strength metric was sought that would be larger for lattices requiring fewer unit cells. After some trial and error, this was correlated to the proximity of the inflection point to the band edges. The farther the inflection point from the band edge, the stronger the self-collimation was observed through simulation. It was surmised that this was due to the strong dispersive effects near the band edge interfering with the self-collimation effect. From this observation, the strength metric  $S$  was defined to have a minimum value of 0 when the inflection point  $\beta_{xi}$  is at a band edge and a maximum value of 1 when the inflection point is at the midpoint between band edges. It follows that the strength metric is

$$S = 1 - \left| \frac{2\Lambda_x}{\pi} \beta_{xi} - 1 \right| \quad (3.13)$$

Simulations showing the correlation between the visual quality of self-collimation and the strength metric are provided in Figure 3.5 [11]. This figure shows simulations over an array of lattices with varying strength metric for the TE mode. Each lattice was simulated at its optimum frequency using an isotropic dipole source placed near the top of the lattice to excite waves at all possible angles. Self-collimation is clearly stronger in lattices with a larger strength metric.

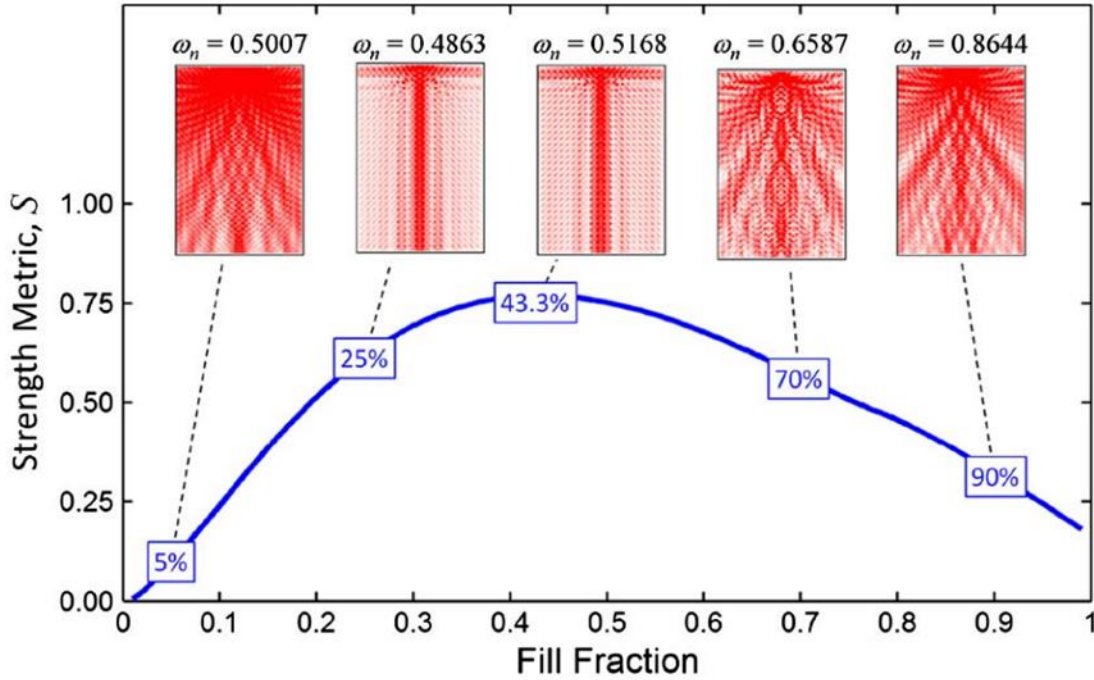


Figure 3.5 [11]: Illustration of the self-collimation effect and the strength metric.

Given these three performance metrics, the FOM for the self-collimation effect is defined as the geometric mean of the performance metrics described above. All of the performance metrics were normalized so their values have no units and fall roughly between 0 and 1. As mentioned previously, a specific application may place more importance on one of these metrics over the other, so they can be individually weighted as needed. The FOM is defined as

$$\text{FOM} = \sqrt[3]{\text{FBW} \cdot \theta_A \cdot S} \quad (3.14)$$

A surprising conclusion from this work is the observation that the optimum frequency for self-collimation is not usually observed to be at the inflection point. There seems to be a trade-off between operating at the inflection point and operating as far away from a band edge as possible. This behavior can be observed in the series of simulations shown in Figure 3.6 [11] that span a range of frequencies containing both the inflection point and the observed optimum frequency.

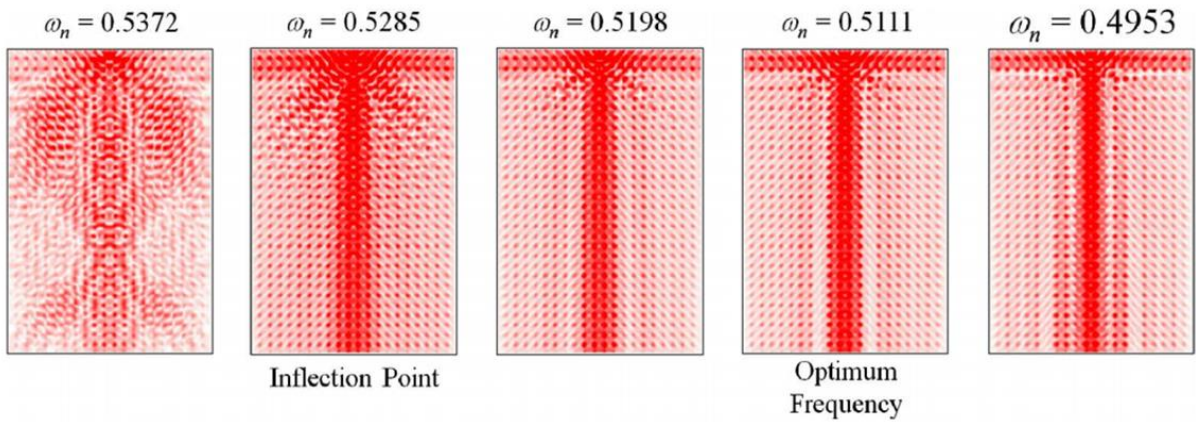


Figure 3.6 [11]: Visualization of self-collimation over a range of frequencies. The optimum frequency for self-collimation is slightly offset from the inflection point.

A dipole source was used at the top of the lattice to excite waves at all possible angles. The optimum frequency was observed to be slightly offset from the inflection point towards a direction opposite the closest band edge. These same offsets were observed using converged models and even different numerical methods. This work does not develop a technique, other than visually, to determine the optimum frequency. It was observed, however, that the optimum frequency and the inflection point were closer in lattices with higher index contrast. It was also observed that the offset between these points fluctuated depending on how the photonic crystal was being used or how it was spatially varied.

## Optimization

Equipped with a robust FOM for the self-collimation effect, photonic crystals can be analyzed and optimized. Considering the baseline unit cell of this work consisting of a square-symmetry two-dimensional unit cell composed of air and rods, only two factors remain: the dielectric constant and the fill fraction. The fill fraction is defined as the percent area filled by  $\epsilon_{r1}$ , as shown by the unit cell in Figure 3.7 [11].

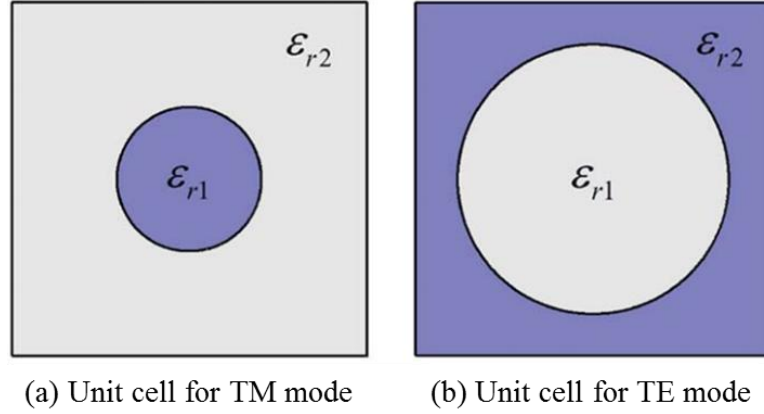


Figure 3.7 [11]: Unit cells for optimization

To study the effects of the dielectric constant on the performance metrics, the fill fractions were fixed to 13% for the TM mode and 45.5% for the TE mode. These quantities are shown later to be the optimum values for each mode. These fill fractions correspond to a radius of  $0.2a$  for the TM mode and  $0.38a$  for the TE mode. Double parameter sweeps were tabulated by iterating  $\epsilon_{r1}$  and  $\epsilon_{r2}$  over the ranges  $1 \leq \epsilon_{r1} \leq 13$  and  $1 \leq \epsilon_{r2} \leq 13$ .

Figure 3.8 [11] shows the data for the double parameter sweep of the TM mode. The same set of data for the TE mode is shown in Figure 3.9 [11]. It can immediately be seen that the TM mode experiences the best self-collimation in lattices composed of high-index cylinders within a low-index surrounding. In contrast, the TE mode prefers inverted lattices with low-index cylinders embedded in a high-index surrounding. In both cases, lattices with low average index and low contrast provided the greatest bandwidth. Lattices with low contrast provided the largest acceptance angle, but the variation was small compared to the variation of the other

parameters. Lattices with high contrast and low average index exhibited the highest strength metric. When all of these metrics are combined into a single FOM, lattices with lower average index are preferred. Unlike other performance metrics, the FOMs for both modes exhibited “sweet spots” that exhibited a maximum because of the competition between the other performance metrics. For the TM mode,  $\epsilon_{r1}=2.51$  and  $\epsilon_{r2}=1.00$  were optimal. For the TE mode,  $\epsilon_{r1}=1.00$  and  $\epsilon_{r1}=3.93$  were optimal. These maxima are highlighted in Figures 3.8 and 3.9 [11].

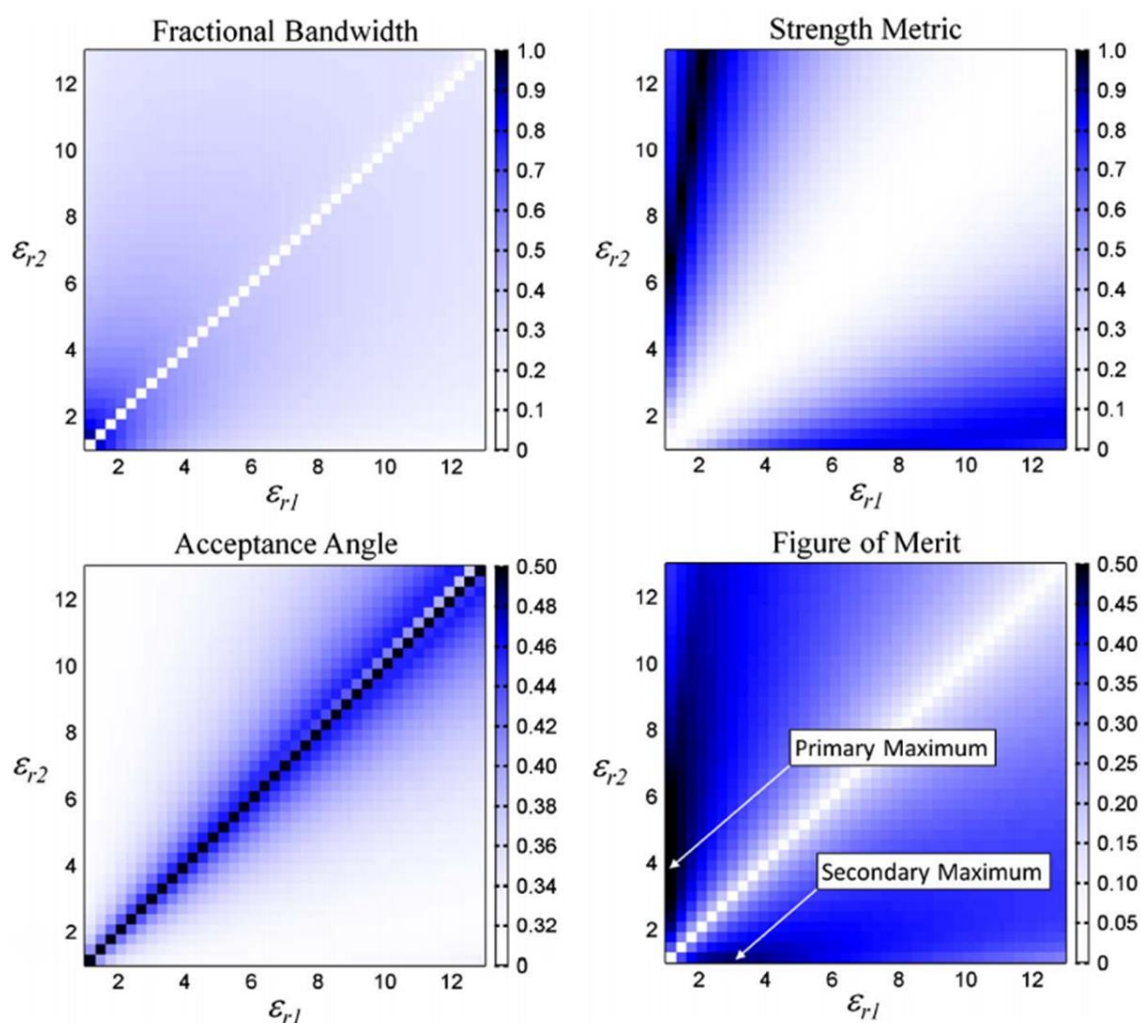


Figure 3.8 [11]: Performance metrics as a function of dielectric constant for the TM mode.

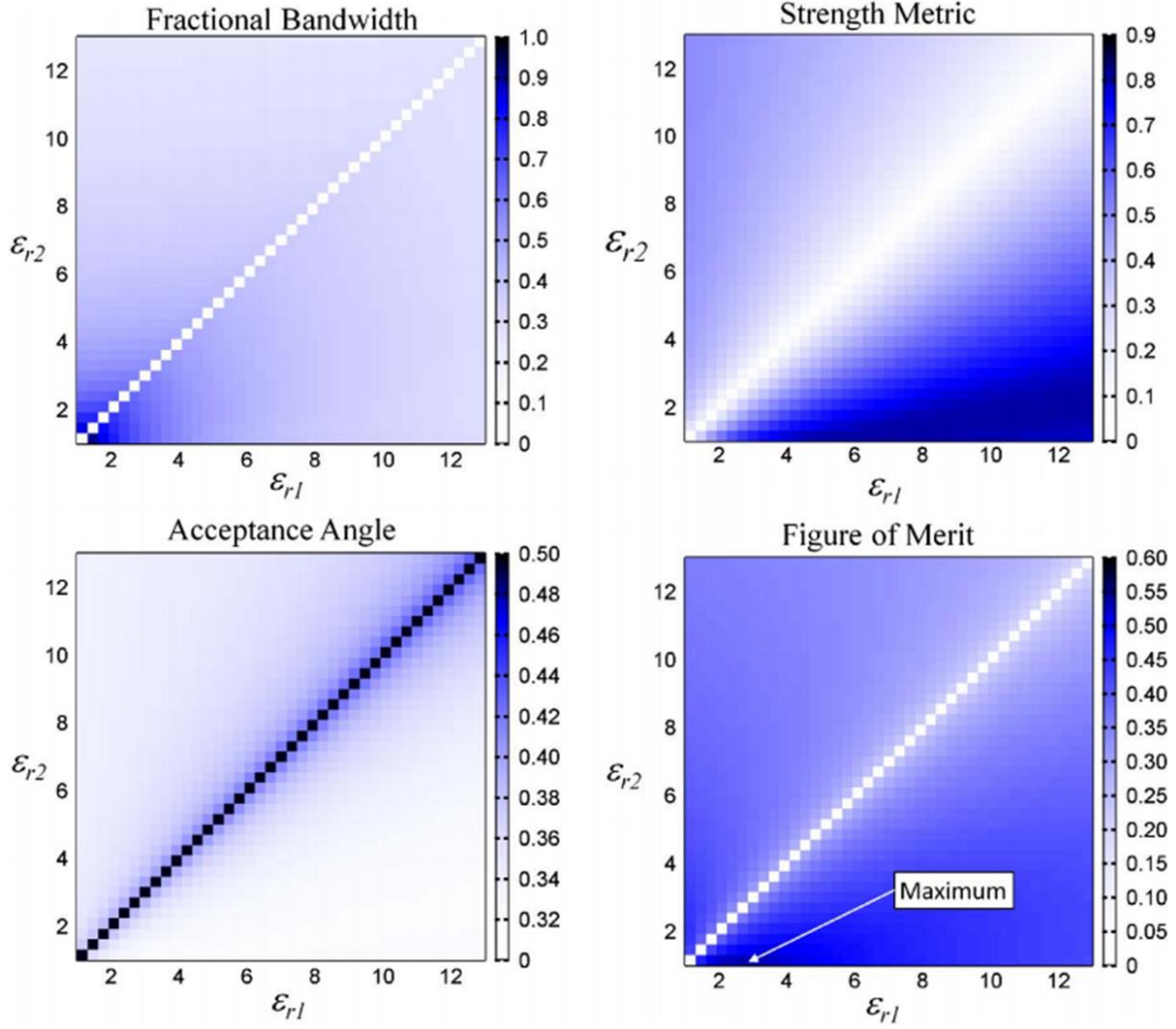


Figure 3.9 [11]: Performance metrics as a function of dielectric constant for the TE mode.

Next, the dielectric constants were fixed to the optimum values identified above to calculate the performance metrics as a function of the fill fraction. This data for both modes are provided in Figure 3.10 [11]. Dramatically different results for the two modes are observed here. For the TM mode, an anomaly occurred over a small range of fill fractions spanning 50%. In this range, the inflection point was very close to the band edge at  $\Gamma$ . Outside this range, and away from the 0% fill fraction, the FBW was relatively flat, but was 16% higher on the low fill fraction side. The acceptance angle was also relatively flat outside the anomalous range. The strength metric, however, exhibited two distinct peaks. The highest peak occurred at 13.5% fill

fraction, while the second peak occurred at 13.5% fill fraction. The shape of the FOM was dominated by the strength metric because the other parameters were relatively constant. This is a useful observation because it suggests that perhaps the FBW and acceptance angle can be ignored during a computationally intensive optimization. The FOM had a maximum at 13.4% fill fraction and a secondary peak at 82.1%.

The TE mode exhibited a very different response to the fill fraction and contained no anomaly except at 0% fill fraction. The FBW remained relatively flat over most of the range but increased gradually with increasing fill fraction. The acceptance angle also remained relatively flat with maximum values at the extreme fill fractions. The strength metric exhibited a strong peak at 43.3% fill fraction and tapered off significantly away from the peak. As was the case for the TM mode, the FOM was dominated by the strength metric due to the relative flatness of the other parameters. In this case, the FOM hit a maximum at 45.5% fill fraction.

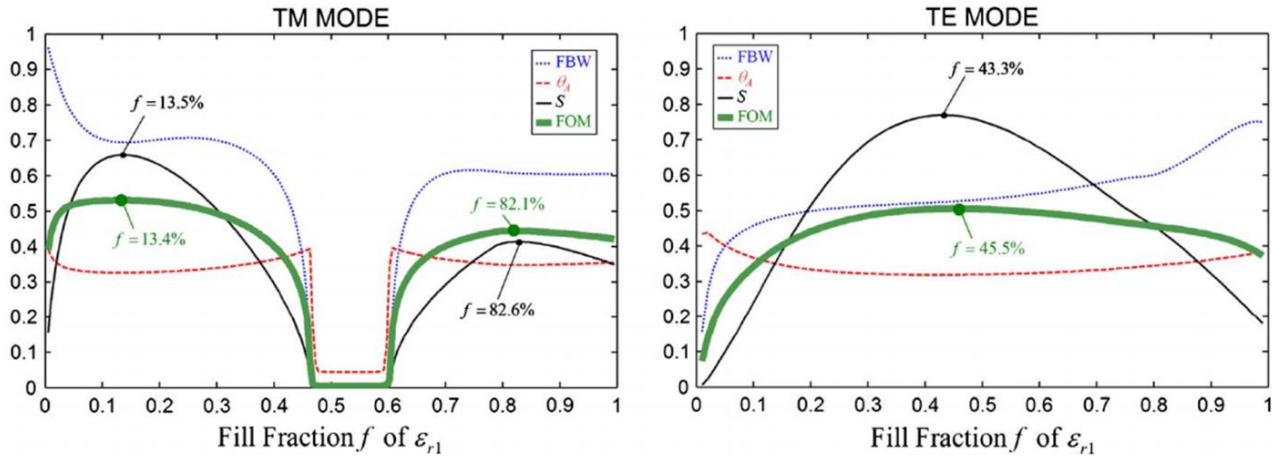


Figure 3.10 [11]: Performance metrics as a function of fill fraction.

After comparing the performance metrics of the TE and TM modes, some important observations can be made. The bandwidth of the TM mode was higher than that of the TE mode. The acceptance angles of both modes were approximately the same. The strength metric was higher and broader for the TE mode. Overall, this led to the TM mode having a slightly higher FOM, but over a narrower range of fill fraction. The TE mode exhibited an FOM with a very

broad peak, perhaps making this lattice more robust to being spatially varied and easier to fabricate. The best unit cell for the TM mode had an acceptance angle of  $\theta_A = 53.8^\circ$  over an FBW of 2.3%. The strength metric was  $S = 0.659$ , and the overall FOM was 0.165. The best unit cell for the TE mode had an acceptance angle of  $\theta_A = 53.7^\circ$  over an FBW of 2.7%. The strength metric was  $S = 0.770$ , and the overall FOM was 0.184.

### ***Applications in Spatially Variant Photonic Crystals***

To demonstrate the effectiveness of the optimization methodology outlined in this work, simulations were performed for two spatially variant self-collimating photonic crystals. These are shown in Figure 3.11 [11]. In these lattices, the unit cell orientation was spatially varied so as to flow and unguided beam around a  $90^\circ$  bend. The first photonic crystal was built from a lattice with a high FOM. It was observed to flow the beam quite effectively around the bend. Some scattering was observed at the output edge because nothing was done to prevent reflections at the interface. In addition, self-collimation does not control phase, and the bend induces phase asymmetrically. This exaggerates the scattering effects at the edges. The second lattice had a lower FOM, and it exhibited highly degraded performance.

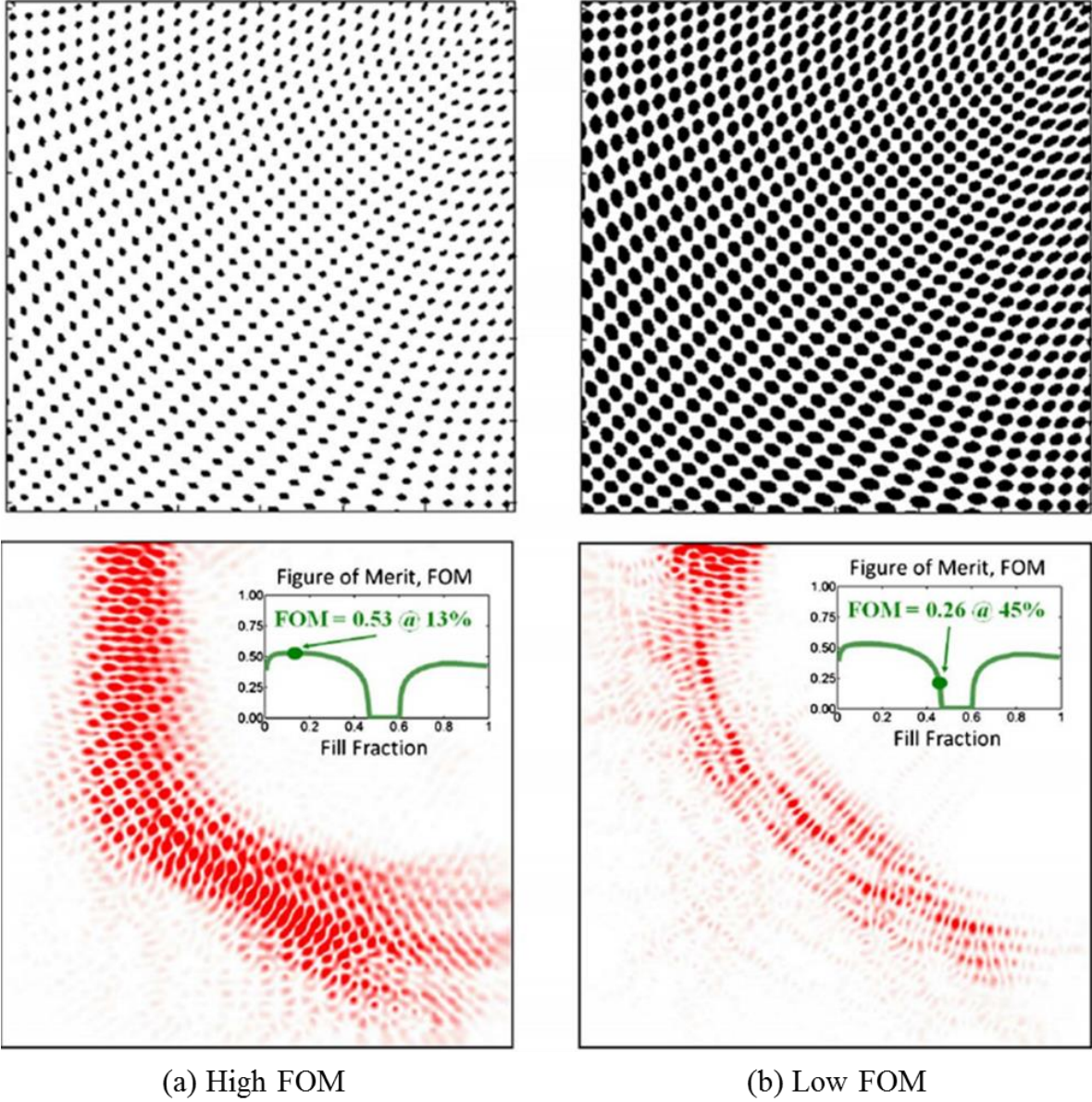


Figure 3.11 [11]: Demonstration of the performance enhancement in a spatially variant self-collimating photonic crystal for the TM mode. (a) Lattice with high FOM, and (b) lattice with lower FOM.

## Chapter 4: Synthesis of Spatially Variant Lattices

### 4.1 MOTIVATION

It is ultimately desired to control every aspect of the electromagnetic field throughout some volume. This includes the direction of energy flow, amplitude profile of the field, phase of the waves, polarization, and more. Many degrees of freedom are necessary to achieve control over such properties. To control electromagnetic fields, however, inhomogeneity in the form of interfaces, modulations, curved surfaces, gradients, and more, is necessary; electromagnetic waves cannot be controlled with homogeneous structures. Periodic structures like photonic crystals and metamaterials have been shown to provide extraordinary control over the electromagnetic field, often offering novel functionalities not before possible using naturally occurring materials. Field control with these structures, namely photonic crystals, has been achieved principally through phenomena including anisotropy, band gaps, and dispersion. These, however, are directional effects, limited to functionality only along the principal axes of the unit cell and thus the overall lattice.

To exploit the useful properties of periodic structures, the efficacy and functionality of well-known directional phenomena, and potentially more, a general purpose synthesis procedure was developed that is capable of simultaneously and independently spatially varying the orientation, fill-fraction, lattice spacing, and other properties of a periodic structure throughout its volume in such a manner that will render the resulting lattice smooth and continuous [21]. Avoiding discontinuities in the lattice is crucial because they produce scattering and field concentrations which can degrade the performance of the device. The ability to smoothly spatially vary these properties of the lattice, namely orientation, enables the aforementioned directional phenomena like band gaps, anisotropy and dispersion to be fully exploited. The algorithm is unique in that it directly calculates the physical geometry of the spatially variant lattice, a huge benefit when at the fabrication stage. This is in contrast to transformation optics (TO), a popular coordinate transformation technique which only calculates the permittivity and permeability tensor functions [19, 20, 22]. It does not calculate the physical geometry of the

lattice necessary to realize these material parameters. With TO, this information must come from a subsequent step. The synthesis algorithm can serve this function.

The algorithm here will be presented in a two-dimensional (2D) domain, although the techniques and formulation can easily be extrapolated to  $n$ -dimensions

## 4.2 SYNTHESIS ALGORITHM

The algorithm can be separated into two sections: 1. Input data including the baseline unit cell, desired direction field, period field, and other information on how the unit cell is to be spatially varied throughout the device; 2. The actual synthesis algorithm and techniques used to process the input data to generate the final spatially variant lattice.

### 4.2.1 Input Data

Several functions must be defined constructed that define the baseline unit cell and how it is to be spatially varied as a function of position. These are inputs to the synthesis procedure and are not generated by the algorithm itself.

#### *Baseline Unit Cell*

The baseline unit describes the specific geometry that is to be arrayed and spatially varied to form the final lattice. The geometry and parameters of the baseline unit cell are selected prior to the synthesis procedure and are typically derived from a rigorous electromagnetic optimization to produce whatever property is desired. For the purpose of this overview, and to echo a geometry that is seen quite often in photonic crystal applications, a unit cell of dielectric rods ( $r = 0.2a$ ) in air background will be used throughout. For the purpose of this algorithm, the unit cell's material distribution function  $\epsilon_{uc}(\vec{r})$  is initialized to all zeros and set to 1 wherever dielectric is to be placed. This can be extended to incorporate multiple materials, where the actual dielectric constants of the materials are incorporated in a later step.

From Fourier theory, a periodic function can be decomposed into a complex Fourier series, where the original function can be approximated by a series of complex exponentials. Periodicity in our unit cell is implied here and in the definition of photonic crystals. Each term

in the Fourier series is called a spatial harmonic, where each can be interpreted as a one-dimensional (1D) sinusoidal grating. Each of these sinusoidal gratings has its own unique period, complex amplitude, and direction (complex amplitudes can be obtained either analytically through Fourier theory or computationally through a Fast Fourier Transform (FFT)). Figure 4.1 shows our baseline unit cell along with a visual representation of a subset of its spatial harmonics and the parameters that can be extracted from it.

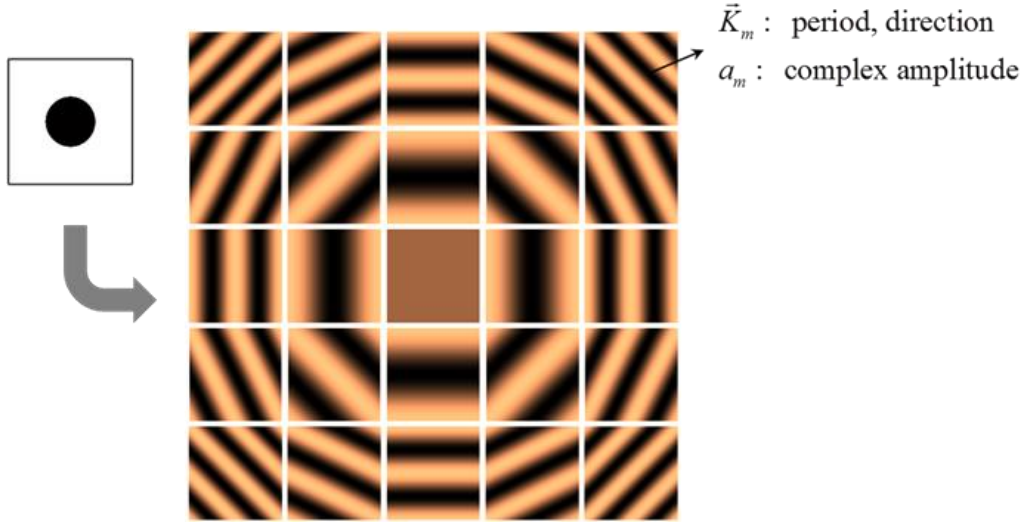


Figure 4.1: The baseline unit cell, its spatial harmonics representation, and the parameters which can be extracted from it.

For square symmetries, the grating vector associated with each spatial harmonic is calculated using Eq. (4.1), where  $p$ ,  $q$  are integers specifying the current harmonic, and  $\Lambda_x$ ,  $\Lambda_y$  are the unit cell dimensions in the  $x$  and  $y$  directions respectively. Given the truncation of the Fourier series terms to an integer number  $M = P \times Q$ , the grating vector for the  $m^{th}$  harmonic is described by Eq. (4.1). This equation is readily extended to 3D by considering the  $z$ -dimension in a similar manner.

$$\vec{K}_{p,q} = \vec{K}_m = \frac{2\pi p}{\Lambda_x} \hat{x} + \frac{2\pi q}{\Lambda_y} \hat{y} \quad (4.1)$$

The grating vectors are determined by the symmetry of the unit cell and the total number of harmonics retained, and they convey information on spatial period and direction. A Fourier transform analysis of the unit cell provides the Fourier coefficients (complex amplitudes) corresponding to the  $m^{\text{th}}$  grating vector. These functions and parameters conglomerate to reconstruct the  $m^{\text{th}}$  spatial harmonic according to

$$\varepsilon_m(\vec{r}) = a_m \exp(j\vec{K}_m \bullet \vec{r}) \quad (4.2)$$

When a series of these spatial harmonics are summed together, they reconstruct the original unit cell according to Eq. (4.3). While an infinite number of spatial harmonics is needed to reconstruct the unit cell exactly, the series must be truncated to a finite set of spatial harmonics  $M = P \times Q$  for practical implementation. Also, while the choice of which spatial harmonics are retained is arbitrary, typically it is the lowest-order harmonics, up to a certain cutoff, which are selected.

$$\varepsilon_{uc}(\vec{r}) = \text{Re} \left[ \sum_{m=1}^M a_m \exp(j\vec{K}_m \bullet \vec{r}) \right] \quad (4.3)$$

In this equation,  $\vec{r}$  is position ( $x$  and  $y$  in 2D),  $a_m$  is the complex amplitude of the  $m^{\text{th}}$  harmonic, and  $\vec{K}_m$  is the grating vector associated with the same. Numerical artifacts may occur during computation, sprouting small, negligible imaginary components in the final summation. Therefore, the real part of the summation is taken as the final devices.

### ***Define the Spatial Variance***

To control how the unit cell orientation, lattice spacing, and fill fraction are to be spatially varied throughout the volume of the lattice, separate functions must be constructed that define each of these parameters as a function of position. These are also defined prior to the synthesis and require knowledge only of the final lattice size. Figure 4.2 demonstrates an example of what the orientation, lattice spacing, and fill fraction functions might resemble and their individual, as well as combined, effects on the lattice.

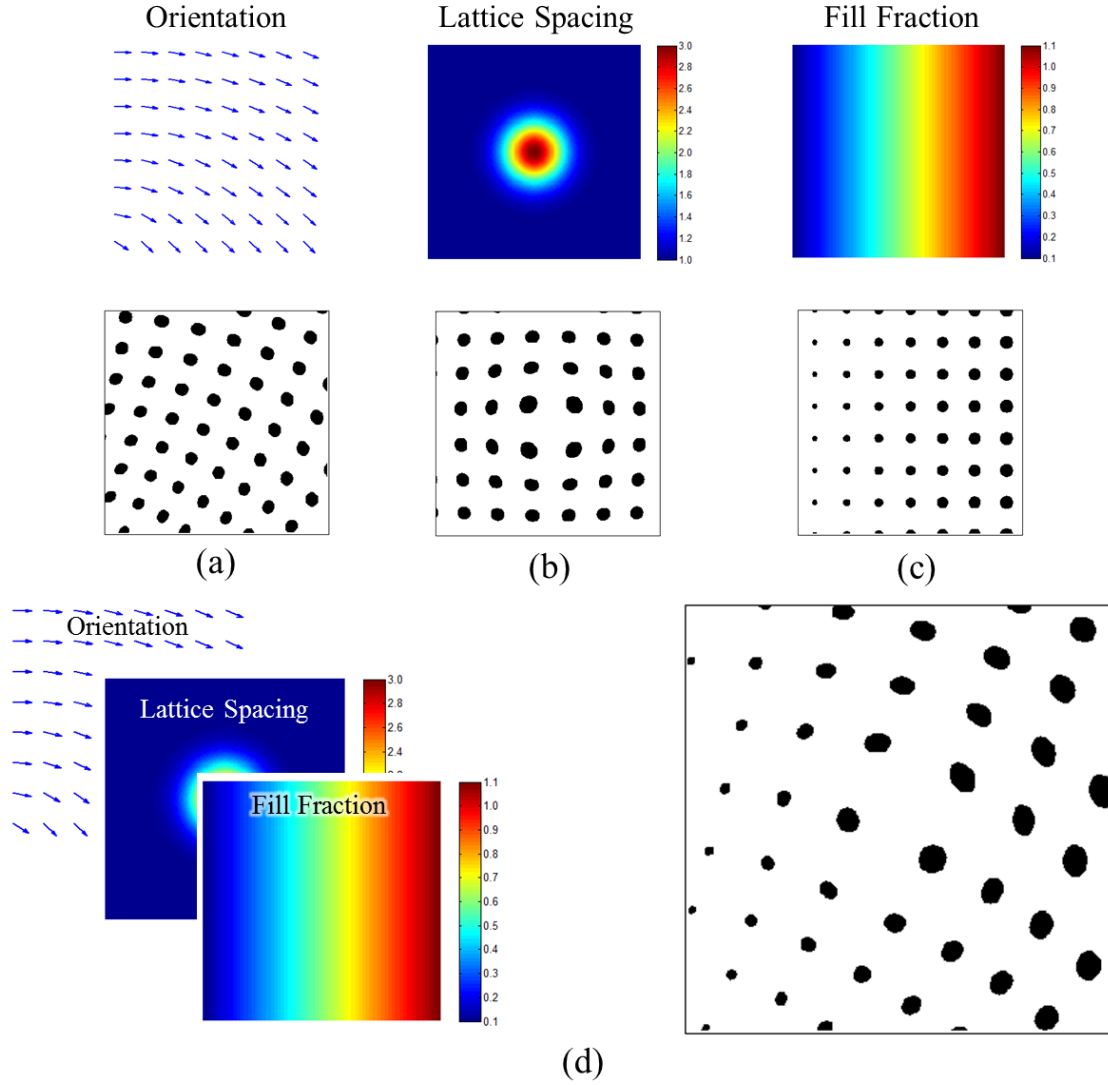


Figure 4.2: The spatially variant parameter functions and their effects on the lattice.

Describing the spatial variance in this manner lends itself well to design by intuition. It therefore offers the ability to incorporate much more complicated patterns than what could be described analytically. Having to describe the spatial variance analytically would put a halt to any transformation optics based efforts, as the coordinate system is a required input to the algorithm.

### 4.2.2 Synthesize the Spatially Variant Lattice

The synthesis algorithm generates the final lattice by spatially varying each of the spatial harmonics separately and then summing the results. The steps to do this for each spatial harmonic are described below.

#### *Construct the Spatially Variant $K$ Function*

Certain spatial variance functions, such as the orientation and the lattice spacing, are implemented through the grating vectors. Parameters like the fill fraction are implemented on the lattice directly after construction. When implementing spatially variant lattice orientation and lattice spacing, the first step is to select the grating vector  $\vec{K}_m$  associated with the  $m^{\text{th}}$  spatial harmonic computed by Eq. (4.1). The information conveyed by this specific vector is then expanded to fill a grid equal in size to the final lattice. An example grating vector selection and its expansion process is shown in Figure 4.3. The orientation of the grating vector will shift as we sweep through the list of length  $M$ .

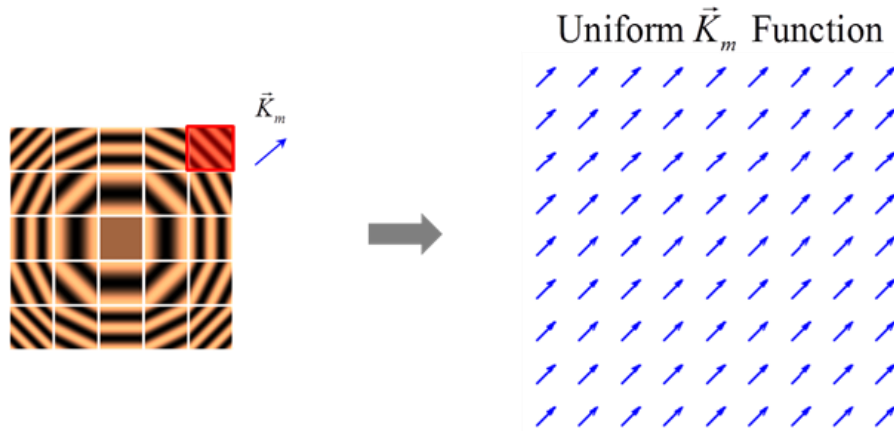


Figure 4.3: Example of the expansion of a grating vector to a full grid.

Second, the tilt of the orientation function is added to this uniform  $K$  function to arrive at an intermediate  $K$  function. Third, the magnitude of the  $K$  function is divided by the lattice spacing function to produce the final spatially variant  $K$  function. In the end, the spatially variant  $K$  function describes both the orientation and the period of the 1D grating as a function of

position throughout the lattice. The aforementioned spatially variant  $K$  function process is visually represented below in Figure 4.4.

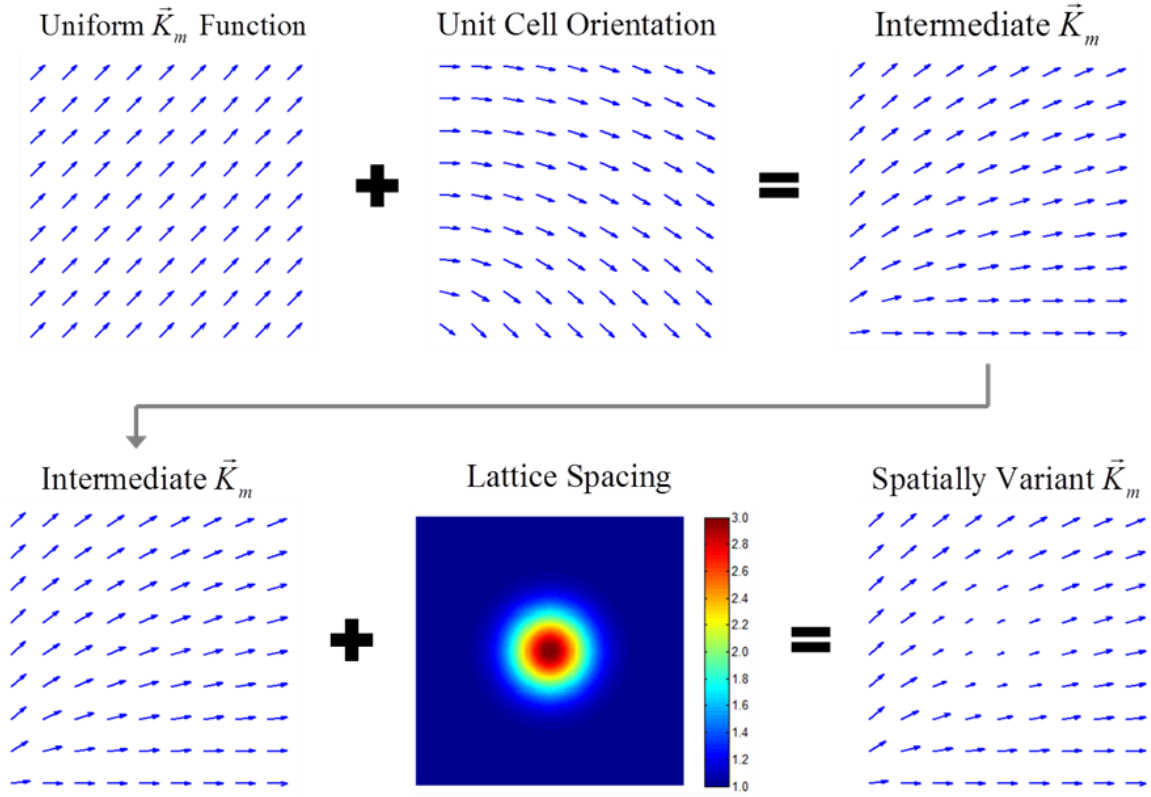


Figure 4.4: Implementing spatially variant orientation and lattice spacing to the current  $K$  function.

### ***Compute the Grating Phase Function***

Having defined the now spatially variant  $K$  function, it is tempting to try to construct the spatial harmonic from Eq. (4.3). This straightforward approach, however, fails to properly construct the grating when the  $K$  function is spatially varied. The problem with this reconstruction is obvious with a chirped grating [53].

$$\varepsilon_m(\vec{r}) \neq a_m \exp[j\vec{K}_m(\vec{r}) \bullet \vec{r}] \quad (4.4)$$

Instead, the spatially variant spatial harmonic can be constructed using an intermediate function called the grating phase  $\phi_m(\vec{r})$ . The grating phase  $\phi_m(\vec{r})$  is related to  $K_m(\vec{r})$  through a gradient operation.

$$\nabla \phi_m(\vec{r}) = \vec{K}_m(\vec{r}) \quad (4.5)$$

A number of analytical and numerical methods can be used to solve Eq. (4.5) to calculate the grating phase from the spatially variant  $K$  function. In this work, the finite-difference method [54] was used to approximate the derivatives in Eq. (4.5). This method results in a large set of equations that can be written in matrix form as

$$\begin{bmatrix} \mathbf{D}_x \\ \mathbf{D}_y \end{bmatrix} \Phi_m = \begin{bmatrix} \mathbf{K}_{x,m} \\ \mathbf{K}_{y,m} \end{bmatrix} \quad (4.6)$$

The term  $\Phi_m$  is a column vector containing the grating phase at each point on the grid. The values are not known at this point but will be calculated shortly. The terms  $\mathbf{D}_x$  and  $\mathbf{D}_y$  are sparse banded matrices that perform derivative operations across the grid using central finite-differences. The terms  $\mathbf{K}_{x,m}$  and  $\mathbf{K}_{y,m}$  are column vectors containing the components of the current spatially variant  $K$  function across the grid.

This process results in an over determined system of linear equations; the matrix formulation contains more equations than it does unknowns. This implies there are more attributes of the grating that are trying to be controlled than there are degrees of freedom to do so. A suitable approach to this problem is to solve the matrix equation in the sense of linear least squares [55], where the resulting 1D grating is seen as a best fit. The least squares approach is apparent from Eq. (4.7), where the unknown vector quantity is the grating phase. The linear least squares approach yields a set of equations termed the “normal equations”, where the minimum solution occurs when the directional derivatives are zero [56]. This leads to a rearranged least squares equation, Eq. (4.8), which now includes the transpose of these matrix operators, as in Eq. (4.9). The matrix  $\mathbf{A}'$  remains a sparse matrix, and the system of equations should be solved as a sparse system for best efficiency [57, 58].

$$\begin{bmatrix} \mathbf{D}_x \\ \mathbf{D}_y \end{bmatrix} \Phi_m = \begin{bmatrix} \mathbf{K}_{x,m} \\ \mathbf{K}_{y,m} \end{bmatrix} \quad \leftrightarrow \quad \mathbf{Ax} = \mathbf{b} \quad (4.7)$$

$$\mathbf{A}'\mathbf{x}_m = \mathbf{b}'_m \quad (4.8)$$

$$\mathbf{A}' = \mathbf{A}^T \mathbf{A} \quad \mathbf{b}'_m = \mathbf{A}^T \mathbf{b}_m \quad (4.9)$$

At this point, the equation for calculating the grating phase function becomes

$$\Phi_m = (\mathbf{A}')^{-1} \mathbf{b}'_m \quad (4.10)$$

As mentioned, direct construction using Eq. (4.4) fails when the  $K$  field is non-uniform. To demonstrate this, direct construction is compared to grating phase construction using Eqs. (4.7) - (4.10). Figure 4.5 (a) [21] shows the spatially variant grating produced by direct construction. In this case, the lattice spacing and orientation are greatly distorted. The grating constructed using the grating phase approach is shown in Figure 4.5 (b) [21]. Here we note the minimized lattice distortions.

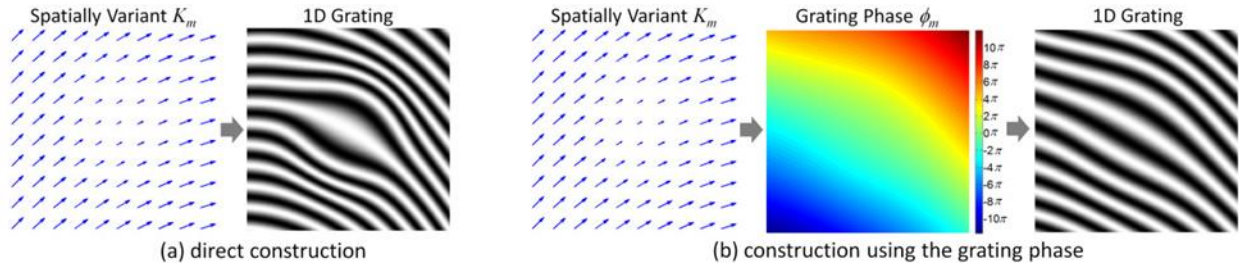


Figure 4.5 [21]: Comparison of the direct versus grating phase approach for the construction of a spatially variant 1D grating.

### ***Compute the Spatially Variant 1D Grating***

Given the grating phase function  $\phi_m(\vec{r})$  and the complex amplitude  $a_m$  of the  $m^{\text{th}}$  spatial harmonic, it becomes a straightforward task to compute the corresponding spatially variant 1D grating using

$$\varepsilon_m(\vec{r}) = a_m \exp[j\phi_m(\vec{r})] \quad (4.11)$$

The dielectric function  $\varepsilon_m(\vec{r})$  is in general complex to convey the offset of the grating. While it is not necessary at this point, the 1D grating can be visualized by ignoring the imaginary component.

### ***Construct Overall Lattice***

Having constructed the list of spatially variant 1D gratings, a preliminary spatially variant lattice  $\varepsilon'(\vec{r})$  is constructed from their sum. It is preliminary because the spatially variant fill fraction has not yet been incorporated; at this point, the profile of the preliminary lattice is an analog one. Also, due to numerical artifacts arising from the FFT, the resulting dielectric distribution may contain small complex components. These are typically many orders of magnitude smaller than the real part and should be neglected. Eq. (4.12) summarizes the procedure after grating construction.

$$\varepsilon'(\vec{r}) = \text{Re} \left[ \sum_{m=1}^M \varepsilon_m(\vec{r}) \right] \quad (4.12)$$

### ***Apply Spatially Variant Fill-Fraction***

The process of applying a spatially variant fill-fraction threshold on the lattice requires an analog profile. Lattices constructed from a low number of spatial harmonics typically have a graded profile. This allows for greater variation in fill-fraction threshold. Conversely, when a lattice is constructed using a high number of spatial harmonics, its profile results in a nearly binary distribution; thus, the fill-fraction options become very limited. When this is the case, blurring of the lattice will yield a smoother profile, allowing for greater versatility in fill-fraction thresholds.

The spatially variant fill fraction of the lattice can then be incorporated by applying a threshold technique to the preliminary dielectric distribution according to Eq. (4.13). This method of applying a threshold also produces the final lattice by incorporating the actual dielectric constants  $\varepsilon_1$  and  $\varepsilon_2$ .

$$\varepsilon(\vec{r}) = \begin{cases} \varepsilon_1 & \varepsilon'(\vec{r}) \leq \gamma(\vec{r}) \\ \varepsilon_2 & \varepsilon'(\vec{r}) > \gamma(\vec{r}) \end{cases} \quad (4.13)$$

When retaining a small number of spatial harmonics, the preliminary dielectric distribution calculated using Eq. (4.12) varies in a near sinusoidal manner. In this case, the threshold needed to realize the fill fraction  $f$  of  $\varepsilon_2$  can be estimated according to

$$\gamma \approx \cos(\pi f) \quad (4.14)$$

### 4.3 NOTES ON IMPLEMENTATION

There are some unit cell choices that can speed up the synthesis algorithm and provide a greater degree of control over its spatial distribution. The algorithm works on each spatial harmonic independently, thus it follows that the time and computational cost to synthesize a spatially variant lattice is proportional to the number of retained spatial harmonics  $M$ . Geometries with sharp discontinuities and small features typically require a larger number of spatial harmonics for accurate reconstruction. While one option to reduce the computational expense is to select an optimized geometry with low harmonic requirements, an alternative may be to generate a unit cell based on a low number of harmonics. Starting with a list of few, defined grating vectors can yield a rather versatile array of geometries. Figure 4.6 [21] shows an example of the many variations of dielectric distributions that can be created with a list of 2 harmonics. This bit of ingenuity affords tremendous savings in time

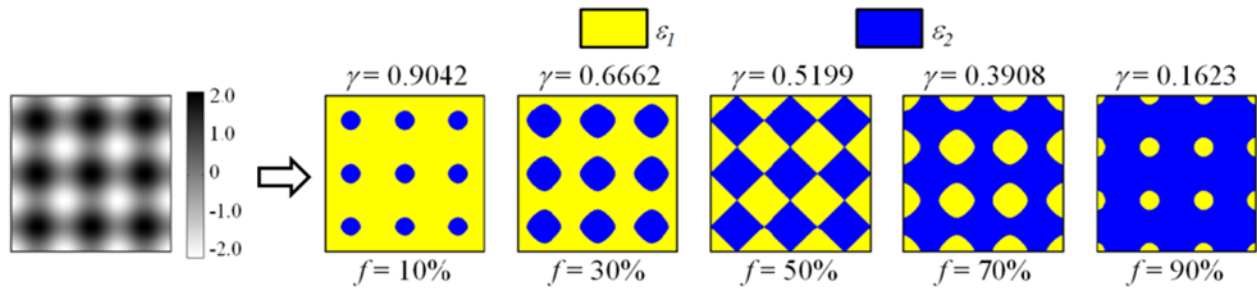


Figure 4.6 [21]: Using the threshold technique to control the fill fraction of a lattice constructed with only two grating vectors. This technique results in many geometries while remaining computationally inexpensive.

The particular threshold parameters will vary according to the unit cell geometry as well as the number of harmonics. As the threshold value  $\gamma$  decreases, the fraction of the lattice filled by material  $\varepsilon_2$  increases. Alternatively, when many spatial harmonics are used, the resulting dielectric distribution will have a high contrast, closer to a binary distribution than an analog one, and thus direct application of Eq. (4.13) becomes less effective. To regain control over fill fraction, the preliminary dielectric function can be partially blurred before applying Eq. (4.13).

#### 4.4 DEFORMATION CONTROL

As consequence of the “best fit” approach in the grating phase function computation, numerical artifacts are present in the resulting spatial harmonic constructed using the grating phase. The actual values of the orientation and lattice spacing functions that the  $m^{\text{th}}$  spatial harmonic should convey are instead offset by small amounts.

The algorithm can be modified to control deformations [59]. The modification begins by constructing the target  $K$ -function  $\vec{K}_T(\vec{r})$  which represents the perfect grating. This becomes the first  $K$ -function  $\vec{K}_i(\vec{r})$  for the iterative algorithm. The grating phase  $\phi_i(\vec{r})$  for the first iteration is calculated from  $\vec{K}_i(\vec{r})$  as

$$\vec{\phi}_i(\vec{r}) = \nabla^{-1} \vec{K}_i(\vec{r}) \quad (4.15)$$

This calculation comes from a best fit so  $\vec{\phi}_i(\vec{r})$  does not correspond to  $\vec{K}_i(\vec{r})$  exactly. The actual  $K$ -function,  $\vec{K}_{a,i}(\vec{r})$ , that results is calculated from  $\vec{\phi}_i(\vec{r})$  as

$$\vec{K}_{a,i}(\vec{r}) = \nabla \vec{\phi}_i(\vec{r}) \quad (4.16)$$

If  $\vec{K}_{a,i}(\vec{r})$  were used as the input for a second iteration, the grating phase from the second iteration would be the same as the first. Instead, the  $K$ -function for the next iteration  $\vec{K}_{i+1}(\vec{r})$  is constructed from some combination of  $\vec{K}_T(\vec{r})$  and  $\vec{K}_{a,i}(\vec{r})$ , depending on the areas of the lattice where deformation control is vital. The three simplest approaches for combining these terms are described here. First, to enforce the orientation of the grating at the cost of the period, the new  $K$ -function is calculated according to

$$\vec{K}_{i+1}(\vec{r}) = |\vec{K}_{a,i}(\vec{r})| \angle \vec{K}_T(\vec{r}) \quad (4.17)$$

This calculation retains the magnitude information from the previous iteration, but replaces the angle with the angle component of the target  $K$ -function. Second, to enforce the grating period at the cost of the orientation, the new  $K$ -function is calculated according to

$$\vec{K}_{i+1}(\vec{r}) = |\vec{K}_T(\vec{r})| \angle \vec{K}_{a,i}(\vec{r}) \quad (4.18)$$

This retains the angle information from the previous iteration, but replaces the magnitude with the magnitude component of the target  $K$ -function. Third, to improve the quality of the grating in critical regions at the cost of the noncritical regions,  $\vec{K}_{i+1}(\vec{r})$  is set equal to  $\vec{K}_T(\vec{r})$  in the critical regions and set equal to  $\vec{K}_{a,i}(\vec{r})$  otherwise.

$$\vec{K}_{i+1}(\vec{r}) = \begin{cases} \vec{K}_T(\vec{r}) & \text{critical regions} \\ \vec{K}_{a,i}(\vec{r}) & \text{otherwise} \end{cases} \quad (4.19)$$

After the new  $K$ -function is constructed, a new grating phase function is calculated and the process repeats. Iteration terminates when the change in the grating phase from one iteration to the next is sufficiently small. This usually happens within 20 to 40 iterations, depending on the size and geometry of the lattice, and the complexity of the spatial variance. Hybrids of these three approaches are possible along with using weighted combinations of the target and actual  $K$ -functions.

Figure 4.7 [59] shows two spatially variant photonic crystals (SVPCs) generated through the synthesis algorithm described in this chapter. Figure 4.7 (a) shows the lattice constructed by the basic algorithm. Deformations due to the abrupt spatial variance caused scattering and reduced transmission to just below 50%. Figure 4.7 (b) shows the SVPC generated using the modified algorithm to control the deformations. In this case, the beam flowed around both bends without any significant scattering or spreading of the beam. Transmission through the second SVPC approached 97%.

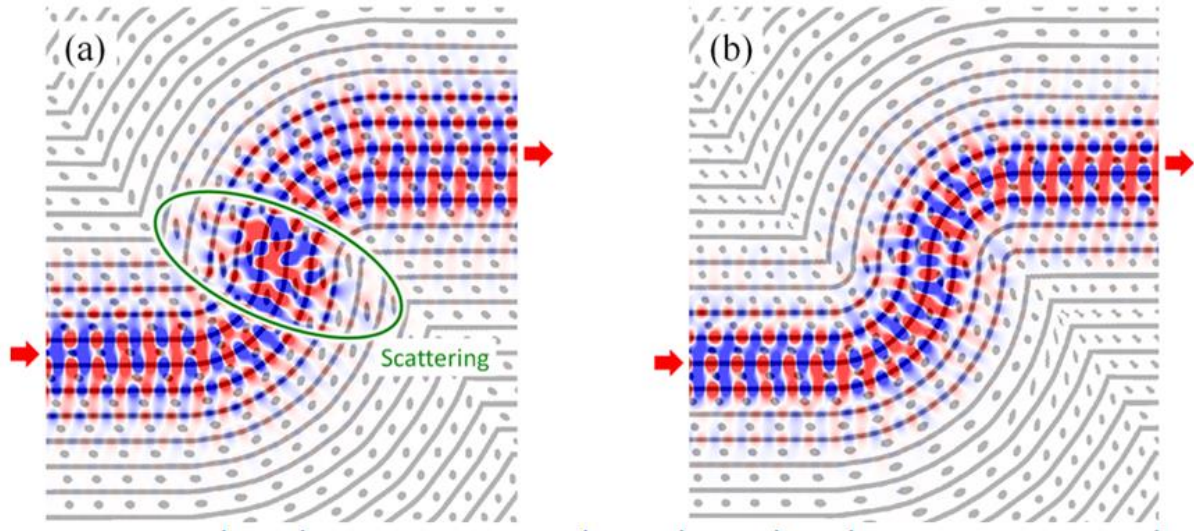


Figure 4.7 [59]: (a) Beam propagation through an SVPC generated using the basic algorithm. Beam scatters at the center of the device. (b) Beam propagation through an SVPC generating with the modified algorithm to control deformations. Beam is well confined and propagates efficiently through the lattice.

## Chapter 5: Spatially Variant Self-Collimating Photonic Crystals

Marrying the self-collimation mechanism of Chapter 3 with the synthesis of spatially variant lattices of Chapter 4, a lattice with spatially variant self-collimation was designed to achieve arbitrary control of waves. To demonstrate the concept, an unguided beam was made to flow around a  $90^\circ$  bend without scattering due to the bend or the spatial variance [60]. Control of the field was achieved by spatially varying the orientation of the unit cells throughout a self-collimating photonic crystal in a manner that would almost entirely eliminate deformations to the size and shape of the constituent unit cells. The resulting device is all-dielectric, monolithic, and comprises only ordinary materials with low relative permittivity ( $\epsilon_r = 2.45$ ). It was manufactured by the 3D-printing technology fused deposition modeling, and its performance was confirmed experimentally around 15 GHz.

Building on this work, a second set of spatially variant photonic crystals (SVPCs) were designed, built, and tested at optical frequencies [61]. In these devices, the orientation of the unit cell changes as a function of position where the lattice spacing and fill factor were made to remain nearly constant throughout the lattice. Abrupt control of light beams using low index materials was achieved. These devices can also be made to have high polarization selectivity. Fabrication of these devices employed the multi-photon direct laser writing technology in the photo-polymer SU-8. The SVPCs were characterized at a wavelength of  $2.94\ \mu\text{m}$  by scanning the faces with optical fibers. These experimental results were compared to electromagnetic simulations. The lattices were shown to direct infrared light of one polarization through sharp bends while the other polarization propagated uniformly through the SVPC. This work introduced a new scheme for controlling light that should prove very useful for integrated photonics.

## **5.1 SPATIALLY VARIANT SELF-COLLIMATING PHOTONIC CRYSTALS AT MICROWAVE FREQUENCIES**

### **5.1.1 Introduction**

Metamaterials and photonic crystals are engineered composites that exhibit superior properties not found in nature, nor are they observed in their constituent materials [62]. They are composed of a periodic array of unit cells with physical features that interact with the applied wave. These produce new and useful phenomena, among them the self-collimation effect. This phenomenon depends strongly on the direction of the applied wave and/or the polarization of the field. Additionally, electromagnetic waves cannot be controlled using homogeneous materials. Functional devices must contain inhomogeneous features such as material interfaces, curved surfaces, gradients, and more. It is therefore necessary to spatially vary the geometric attributes of the lattice in order to: 1. Exploit directional phenomena, and/or 2. Make the lattices macroscopically inhomogeneous. This spatial variance, however, must be incorporated in a manner which will not deform the geometry or composition of the unit cells, as this will degrade the performance of geometrically-tuned effects.

It is also important to note that a major setback for traditional metamaterials is the prohibitively high loss caused by metallic resonators [63, 64]. This loss is often prohibitively large for certain applications. The extensive use of metals in traditional metamaterials also makes them less viable for specialized applications at high power [65] or at high temperatures [66] where problems with loss, heat, arcing, and chemical reactivity are much more pronounced.

All-dielectric metamaterials and photonic crystals offer an attractive solution to these problems. One issue, however, is the weaker interaction with the field that dielectric exhibit. This limits the design options, but it can be partly overcome through clever engineering of the dispersion and anisotropy of the dielectric structures. Achieving these tailored dispersion relations, however, usually requires devices with highly complex geometries which are not feasible to manufacture by conventional means. In these regards, 3D printing seems ideally

suited for producing the next generation of electromagnetic devices. These will present unprecedented, complex geometries that will likely make heavier use of sculpted dielectrics.

Here, we demonstrate a spatially variant all-dielectric photonic crystal as a new method for spatial control of electromagnetic waves in 3D systems. The device exploits the directional properties of the self-collimation effect to perform the simple task of flowing an unguided beam around a 90° bend without diffracting or scattering. The final device is shown in Figure 5.1 [60].

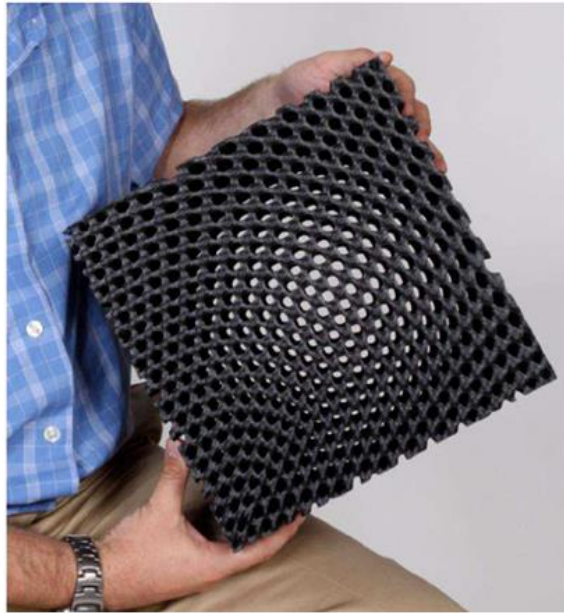


Figure 5.1 [60]: Photograph of the spatially variant self-collimating lattice designed to operate at microwave frequencies.

These dispersion properties arise from conditions of the self-collimation effect, a phenomenon where a beam propagates without diffraction and is forced to flow in a direction relative to the principal axes of the unit cells. Using this effect, a beam can be made to flow along an arbitrarily curved path; one that is dictated by the spatially variant orientation of the unit cells. Devices based on self-collimation can be monolithic, all-dielectric, and composed of just ordinary isotropic materials. The author's experience has shown that such devices are also highly tolerant to dielectric loss and to surface roughness. Excellent performance can even be obtained using materials with low dielectric constant (i.e.  $\epsilon_r < 3.0$ ), which are usually less

expensive and more commonly available than more exotic dielectrics with higher permittivity. Spatially variant self-collimation is unique because it spatially varies the orientation of the unit cells within an otherwise monolithic and uniform lattice. Devices can often be designed with fewer lattice periods and with lower dielectric contrast than with alternative approaches. No extreme or anisotropic constitutive parameters are needed. Other degrees of freedom like fill fraction and lattice spacing can be spatially varied at the same time for further optimization or building in additional functionality. This device is not a waveguide and cannot be designed through transformation optics because the unit cells are isotropic and their fill fraction is kept uniform throughout the lattice.

### 5.1.2 Device Design

#### *Baseline Unit Cell*

The device design began with a unit cell described by the superposition of only three planar gratings. This description was chosen to speed the procedure of synthesizing the spatially variant lattice, as mentioned in a previous chapter. The grating vectors describing the three planar gratings were chosen to produce a simple cubic symmetry lattice as follows:  $\vec{K}_1 = \hat{a}_x 2\pi/\Lambda$ ,  $\vec{K}_2 = \hat{a}_y 2\pi/\Lambda$ , and  $\vec{K}_3 = \hat{a}_z 2\pi/\Lambda$ . From these, the unit cell as a function of position  $\vec{r}$  was constructed according to Eq. (5.1) by adding the three gratings and then applying a threshold to define regions as either air or dielectric. To generate a unit cell with 30% fill fraction of dielectric, the threshold parameter was set to  $\gamma = 0.6165$  according to the equation below.

$$\varepsilon(\vec{r}) = \begin{cases} 1.0 & \varepsilon'(\vec{r}) \leq \gamma \\ \varepsilon_{uc} & \varepsilon'(\vec{r}) > \gamma \end{cases} \quad (5.1)$$

$$\varepsilon'(\vec{r}) = \cos(\vec{K}_1 \cdot \vec{r}) + \cos(\vec{K}_2 \cdot \vec{r}) + \cos(\vec{K}_3 \cdot \vec{r})$$

The device was manufactured using a polycarbonate-ABS blend (310-20500 filament from Stratasys) which was measured to have a dielectric constant of  $\varepsilon_{uc} = 2.45$  at 15 GHz. The loss tangent of the material was ignored in the design, but it was measured to be  $\tan \delta = 0.04$  at this

same frequency. The lattice spacing was chosen to be  $\Lambda = 1.59$  cm to place the center frequency of self-collimation at around 15 GHz. The resulting unit cell is shown in Figure 5.2 [60].

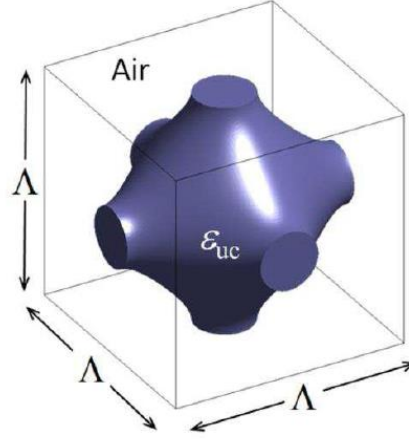


Figure 5.2 [60]: Three-dimensional simple cubic unit cell with 30% fill fraction.

The unit cell was analyzed for self-collimation conditions using the concept of isofrequency contours (IFCs), as explained in Chapter 3. These were calculated using the reduced Bloch mode expansion technique [50] based on the plane wave expansion method. IFCs are dispersion surfaces in  $k$ -space that characterize the magnitude of the wave vector as a function of the direction of a Bloch wave propagating through a uniform infinite lattice. Given a point on an IFC, phase propagates according to the wave vector that extends from the origin to that point. In contrast, energy propagates according to the Poynting vector that is in a direction normal to the surface of the IFC at that point. In ordinary isotropic materials, the IFCs are spherical, and phase and energy propagate in the same direction. In photonic crystals, the IFCs can be engineered to take on other shapes, usually resembling the shape of the Brillouin zone. In these cases, the energy and phase of a wave can propagate in different directions. Self-collimation occurs when a portion of the IFC is flat and energy is forced to flow in a common direction over an entire span of wave vectors. Only small portions of the IFC are truly flat, however, and Fourier components of a beam that lie outside the flat regions will diverge, but much more slowly than they would outside of the lattice. The severity of the divergence depends

on the slope of the IFC. In addition, when the beam exits the lattice, it is no longer self-collimated, and it will diverge or diffract according to whatever amplitude and phase distribution is imparted on the beam.

In this work, the threshold was estimated by requiring that no energy in the beam be offset laterally by more than half of the beam width  $w$  after propagating through the entire lattice. If the beam must travel a total distance of  $L$ , the angle tolerance should be set to  $\tan \theta = w/(2L)$ . In the present device, the beam travels a total distance of 19.7 unit cells, and through simulation it was assessed that the beam width amounts to about 6 unit cells inside the lattice. Based on these quantities, the angle tolerance was calculated to be  $\theta = 8.7^\circ$ . From this, a field-of-view (FOV) for the self-collimation effect was defined to be the solid angle that bounds the region of self-collimation. A bandwidth metric for the self-collimation effect was further defined to be the range of frequencies over which the IFCs remain flat to within this same tolerance. Figure 5.3 [60] shows the 3D IFC calculated at 15.2 GHz as well as a cross section of all the IFCs throughout the entire Brillouin zone. The 3D IFC at the center of this figure is shaped like a cube with rounded corners where a large portion of each face is flat to within the above threshold. The FOV enclosing the flat region on the IFC is shown as a rounded square cone emanating from the origin. From this data, the FOV was predicted to be  $52.5^\circ$ , and it was maintained over a fraction bandwidth of 6.1% (915 MHz).

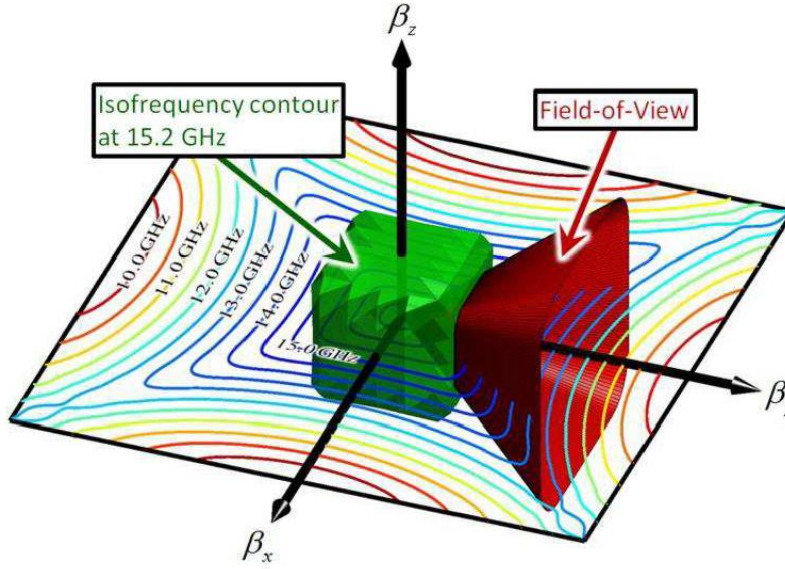


Figure 5.3 [60]: Isofrequency contours superimposed with field of view.

The FOV can be considerably larger over narrower bandwidths. A consequence of the IFC resembling a cube is that the lattice has the ability to self-collimate along three different axes. If defects are introduced into the lattice, power can be scattered into these other directions. The scattering can be suppressed somewhat by tailoring the symmetry of the unit cells, but this was not done in the present work because no defects were introduced and the spatial variance was kept sufficiently smooth.

### ***Synthesis of Spatially Variant Lattice***

Given this baseline unit cell design, the geometry of the spatially variant lattice was generated to flow a beam around a  $90^\circ$  bend. The novel algorithm presented in Chapter 4 was used to spatially vary all of the attributes of the lattice independently and simultaneously while still rendering the overall lattice smooth and continuous [21]. The present design called only for the orientation of the unit cells to be gradually rotated by  $90^\circ$  in an azimuthal pattern, as illustrated in Figure 5.4 [60].

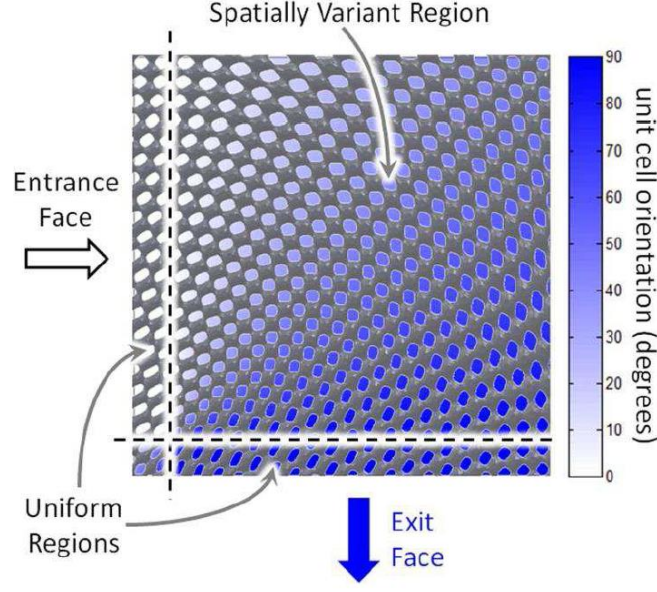


Figure 5.4 [60]: Final lattice superimposed above the orientation function.

The arrows outside the lattice identify the entrance and exit faces. As indicated in the figure, the orientation of the unit cells was made constant for a two unit-cell-wide area at the entrance and exit faces to assist the beam's transition into and out of the bend. The pattern of the orientation function at the extreme inside of the bend was constructed to make the function as smooth and continuous as possible. The synthesis algorithm kept the lattice spacing extraordinarily uniform despite the orientation of the unit cells being spatially varied and the radius of the curve varying by more than  $20\times$  across the device. This property is crucial because fluctuations in the shape and size of the unit cell detune the self-collimation effect.

A basic assumption in the design approach described above is that the lattice is uniform and infinitely periodic. This assumption is no longer true when the lattice is spatially varied. As long as adjacent unit cells are sufficiently similar, however, the resonance and dispersion effects of the lattice can still be maintained to some degree. In the context of IFCs, spatially varying the orientation of the unit cells rotates the IFCs along with the unit cells. In this manner, the directionality of the self-collimation effect is spatially varied so as to flow a beam along a desired path.

To assess how abruptly a lattice can be spatially varied while maintaining a quality self-collimated beam, a series of simulations was performed for varyingly sized lattices using the finite-difference frequency-domain (FDFD) method. The confinement of the beam around the bends was visually evaluated. These results are shown in Figure 5.5 [60]. While lattices as small as  $12 \times 12$  unit cells performed reasonably well, it was decided to manufacture the final lattice with  $22 \times 22 \times 11$  unit cells as a safety margin.

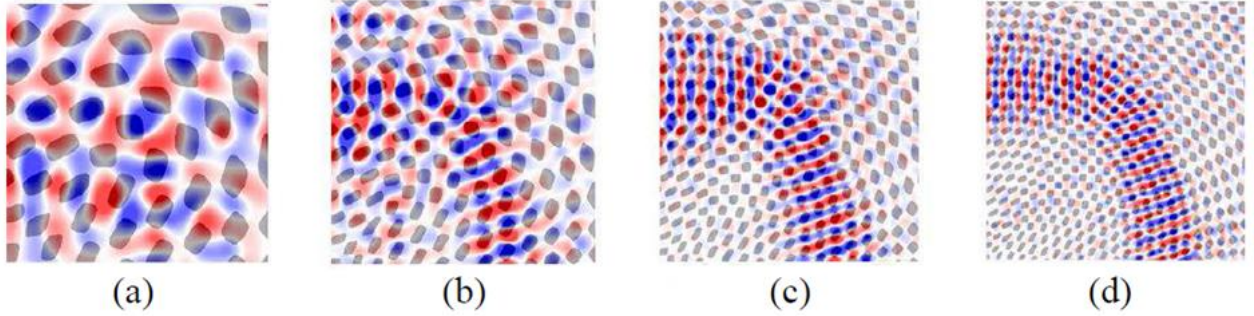


Figure 5.5 [60]: Simulations of lattices of different sizes to determine the minimum bend radius. (a)  $7 \times 7$  unit cells. (b)  $12 \times 12$  unit cells. (c)  $17 \times 17$  unit cells. (d)  $22 \times 22$  unit cells

The 3D geometry of the selected device was exported from the synthesis tool as an industry standard STL file [67].

### 5.1.3 Experimental Results

3D printing is ideally suited for manufacturing devices with complex geometries, as it provides the ability to arbitrarily place different materials in three dimensions with high precision. It is already well established for producing rapid prototypes, but recent advances in equipment and materials have made it viable for producing functional devices and even final products. The device in this work was printed from the STL file using fused deposition modeling (FDM) in a Stratasys FDM 400 mc. FDM was inspired by the hot glue gun; it feeds an inexpensive thermoplastic filament through a print head where it is melted and deposited onto the surface of a platform. The print head is translated within the horizontal plane to deposit a layer of the material in the desired pattern. When a layer is finished, the platform is lowered by a

few thousandths of an inch and the next layer is written on top of the previous. This process is repeated layer-by-layer to produce a fully three-dimensional structure. Printed parts are typically built with temporary support material to prevent sagging of the hot plastic. It was determined that our device could be printed without using support material, which would have been difficult to remove from the internal features of the device. Building without support cannot always be achieved, but in this case the lattice features were self-supporting when the fill fraction was set to 30%. The final device, shown in Figure 5.1, took approximately two weeks to build.

To experimentally evaluate the device's performance, the lattice was placed onto a Styrofoam platform and illuminated at the entrance face by a standard gain horn antenna operating within the Ku-band (12 GHz to 18 GHz). Styrofoam was used as a base for the device, as its electromagnetic properties (in this context) are akin to those of air. A field probe was constructed from a small monopole antenna and scanned around the perimeter of the device to profile the field. 44 samples were taken along each of the three sides for a total of 132 measure points. The data was captured using an Agilent N5245 PNA-X vector network analyzer. Figure 5.6 (a) [60] shows the device in its test configuration. Figure 5.6 (b) [60] shows the field amplitude data measured at 15.2 GHz plotted around the perimeter of the device where it was measured.

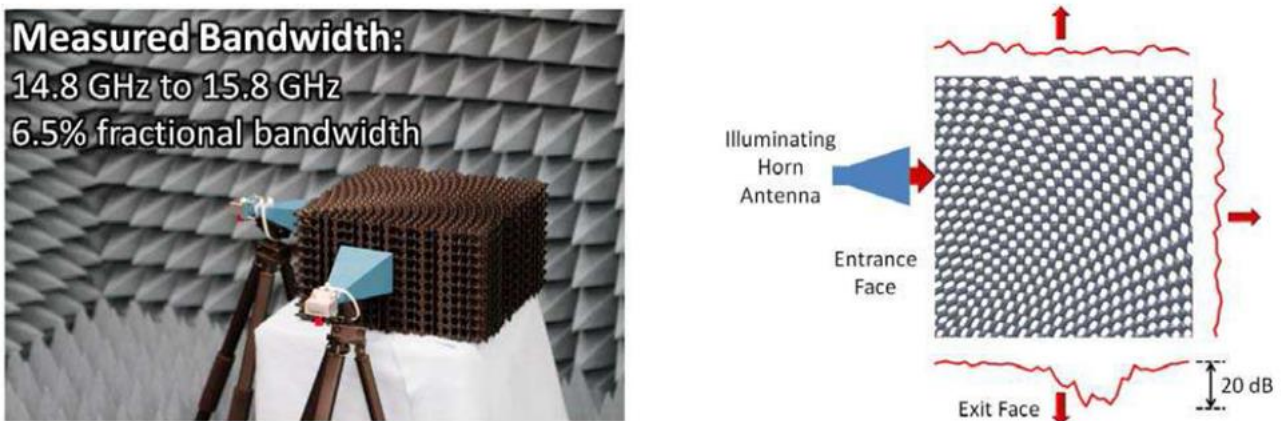


Figure 5.6 [60]: Experimental results for the spatially variant self-collimating lattice. (a) Spatially variant lattice in test setup. (b) Measured field profile around the perimeter of the device.

It was observed experimentally that the device self-collimated within the frequency range of 14.8 GHz to 15.8 GHz, exhibiting a 6.5% fractional bandwidth. An approximately 20 dB (99%) fluctuation in the field amplitude in the location of the exiting beam was measured. The mismatch between air and the lattice produced some scattering from the edges of the device. Techniques have been developed to overcome this [68-71], but they were not implemented in this work. Noise in the experimental results was caused by waves scattered from the exit face. These waves reflect backwards into the device in multiple directions, eventually exiting through all faces. This scattering was as well observed in simulation. Despite these imperfections, the exiting beam is most prominent, and the data confirms the device's operation without a doubt.

#### **5.1.4 Conclusion**

This work demonstrated a novel all-dielectric spatially variant self-collimating photonic crystal. It performed the task of flowing an unguided beam around a 90° bend without diffracting or scattering. It was the first known effort to exploit the directional dependence of self-collimation by spatially varying the orientation of the unit cells throughout a lattice. The all-dielectric design eliminated the loss problems associated with traditional metallic metamaterials. Excellent performance was achieved through a lattice that was synthesized to minimize defects and lattice spacing fluctuations; it was also manufactured very well by 3D printing. The concepts demonstrated by this device, and their many variations, provide new mechanisms for controlling electromagnetic waves. Due to the size scale, most applications of self-collimation will be in the millimeter wave to optical frequencies and may include switching, fan out devices, coupling circuits, spectroscopy, creating quiet zones for antennas or sensors, modifying the radiation patterns of antennas, shaping beams, manipulating images, energy collection, and more. Future work could readily entail more complex spatial variance map, techniques to better match into the lattice, other spatially varied parameters, and more.

## **5.2 SPATIALLY VARIANT SELF-COLLIMATING PHOTONIC CRYSTALS AT OPTICAL FREQUENCIES**

The success of spatially variant self-collimating photonic crystals for controlling unguided beams would be very useful at optical frequencies. Integrated photonic systems require a similar abrupt control of optical beams to route signals, control polarization, and more. Following the methodology of Section 5.1 to design spatially variant self-collimating photonic crystals at optical frequencies, several optical spatially variant photonic crystals were designed and shown to be capable of abruptly guiding light beams using low index materials [61]. They were also shown to have high polarization selectivity.

The authors of Ref. [61] fabricated three-dimensional SVPCs using multiphoton direct laser writing in the photo-polymer SU-8. The SVPCs were designed to flow light around a 90° bend and were characterized at a wavelength of 2.94  $\mu\text{m}$ . Referencing scans of the SVPCs, collected through scanning electron microscope (SEM) imaging of their faces using optical fibers [61], this work focused on the computational modeling and electromagnetic optimization of them. Experimental results were compared with electromagnetic simulations. Polarization selectivity was shown by the bending of one polarization while the other polarization propagates straight through the SVPC. This work introduces a novel scheme useful for controlling light in integrated photonics applications.

### **5.2.1 Computational Modeling of the SVPCs**

The geometry, lattice spacing, and fill fraction of the SVPCs were approximated using SEM scans of the printed devices themselves. Figure 5.7 [61] shows images and information of one of the SVPCs.

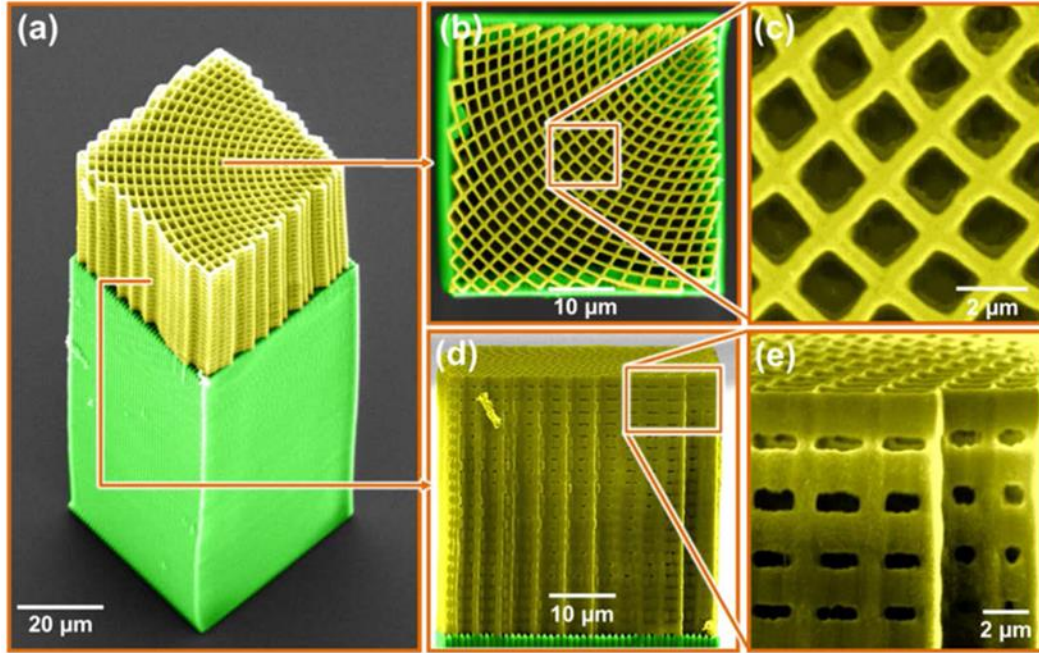


Figure 5.7 [61]: False-color SEM images of an SVPC. The perspective views and dimensional analysis noted in the figure were the information available to accurately model these in a computational domain.

These scans, and the information provided therein, served as the design parameters used to build the computational model.

The three-dimensional cubic unit cell design began with the superposition of three orthogonal elliptic cylinders. After the voxel was defined as the Boolean sum of these, a Gaussian blur function was applied to it, where the regions of higher Boolean values were subject to a heavier blur. This process was designed to attempt to model the nonlinear chemical processes of the areas of higher exposure. Figure 5.8 (a)-(b) [61] shows the unit cell affected by the blur (red) superimposed on the ideal (blue). Blurring the voxel more achieved a more accurate representation of the physical geometry. Once the voxel was obtained, a 2D model was extracted from it for electromagnetic simulation. The effective refractive index profile of the 2D model was approximated by marching along the  $x$ - $y$  plane and averaging the material's fill fraction along the  $z$ . Figure 5.8 (c) shows a rendition of this process. The refractive index  $n$  and

extinction coefficient  $\kappa$  for SU-8 film at  $2.94\ \mu\text{m}$  was obtained through the ellipsometry measurements of Ref. [61].

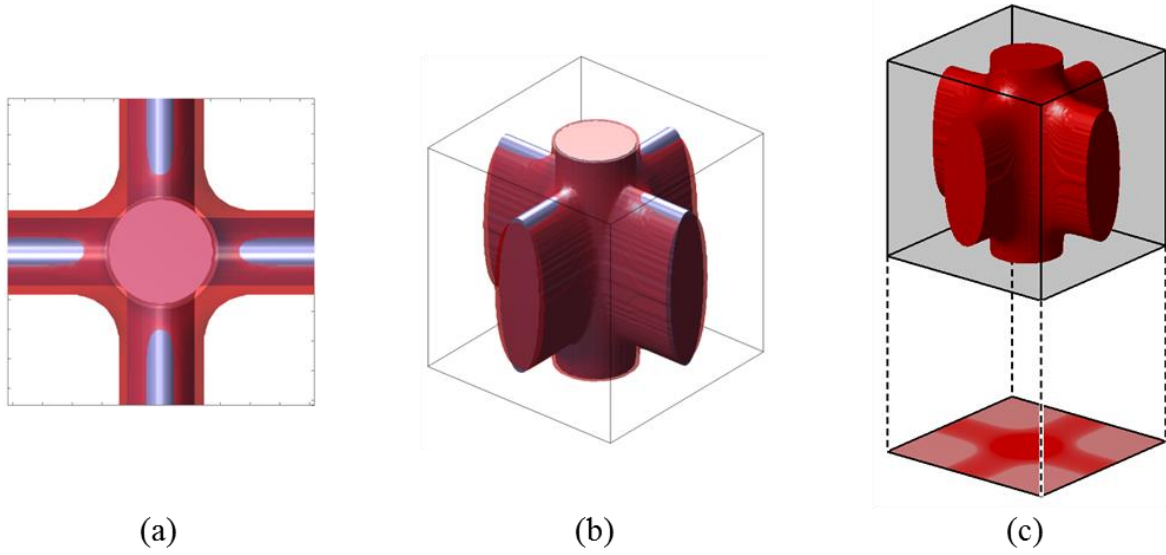


Figure 5.8 : (a)-(b) [61] Perspective views of the ideal (blue) versus diffusion-simulated model unit cell. (c) A 2D approximation of the effective refractive index profile.

A 2D model of the spatially variant lattice was obtained using a similar methodology. It was constructed from a single layer of the 3D lattice using a similar effective index method. The effective refractive index at each  $(x,y)$ -position of the 2D lattice was obtained by averaging the refractive index along the corresponding column in the 3D lattice. Figure 5.9 [61] shows the resulting 2D lattice from this process.

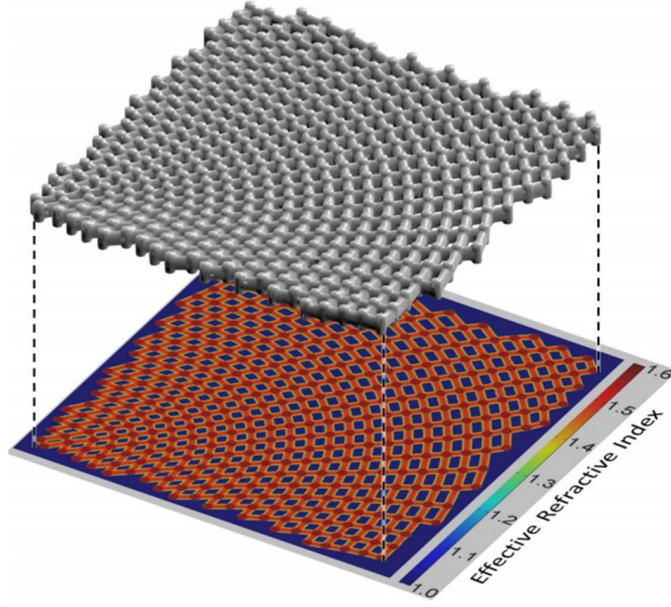


Figure 5.9 [61]: The 2D model that was generated from the 3D lattice using the effective index method. This 2D model was used for simulating the SVPCs.

### 5.2.2 Electromagnetic Simulation of the Optical SVPCs

The process stepped through above was performed for several SVPCs of varying lattice constants and fill fractions. These were characterized through the finite-difference frequency-domain algorithm discussed in Chapter 2. The 2D lattices consisted of  $22 \times 22$  lattice constants in the  $x$  and  $y$ , respectively. The SVPCs fabricated at 39%, 44%, and 70% fill fraction, along with their electromagnetic simulations, are shown in Figure 5.10 (a)-(f) [61]. The simulations show the TM mode polarization, where the electric field is normal to the plane of periodicity. It is also shown that the measured beam bending efficiencies of these simulations match the experimental ones.

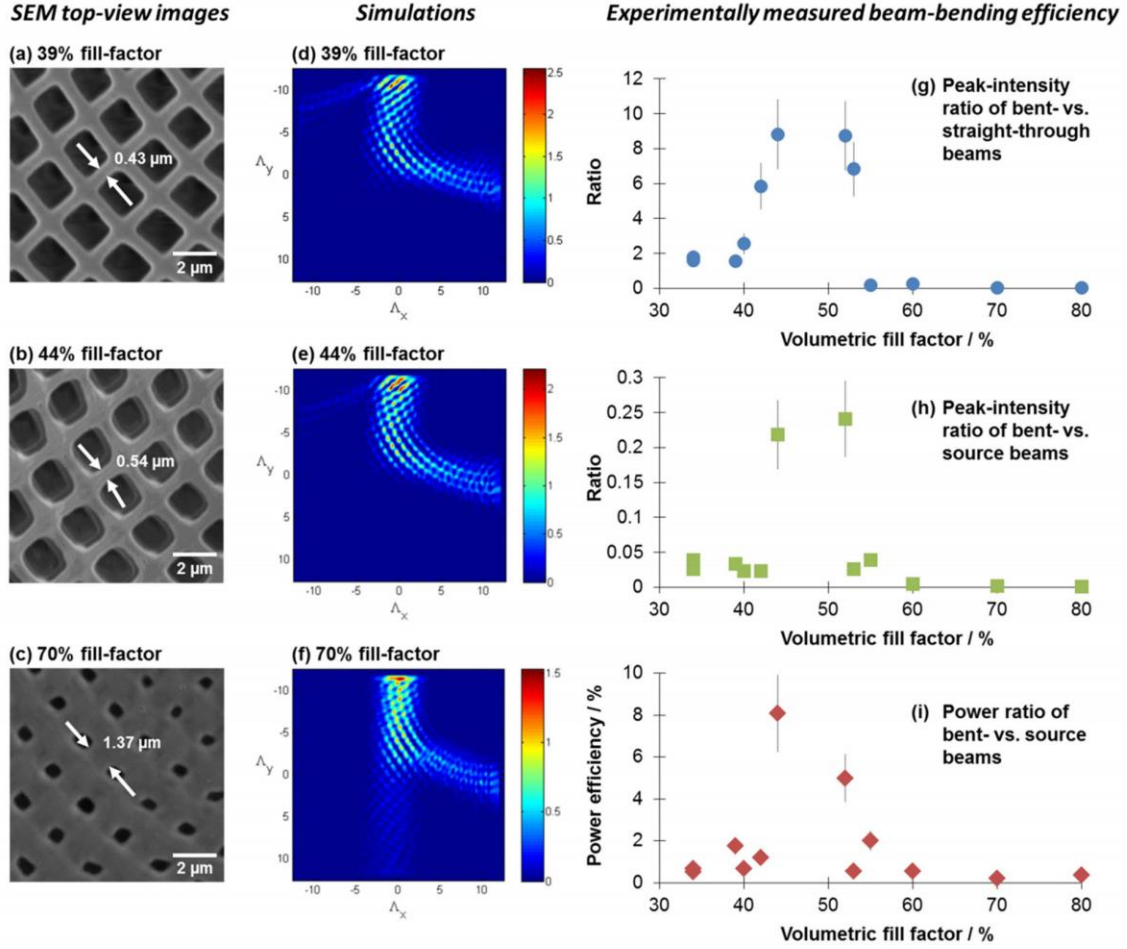


Figure 5.10 [61]: (a – c) SEM image views of the SVPCs of varying fill factors and (d – f) the electromagnetic simulations of the intensity of vertically polarized light. (g – i) The experimentally measured beam-bending efficiency of the SVPCs versus varying fill factors.

The beam bending efficiency of the SVPCs was further characterized by its polarization sensitivity. Figure 5.11 [61] shows the beam bending efficiencies, calculated as the ratio of intensities of the output versus the input, for both vertical and horizontal polarizations. The lattice was designed to self-collimate vertically polarized beams, while allowing the beam to flow straight through, virtually ignoring the spatial variance, with horizontally polarized light. It was found that these SVPCs favored fill factors close to 50%.

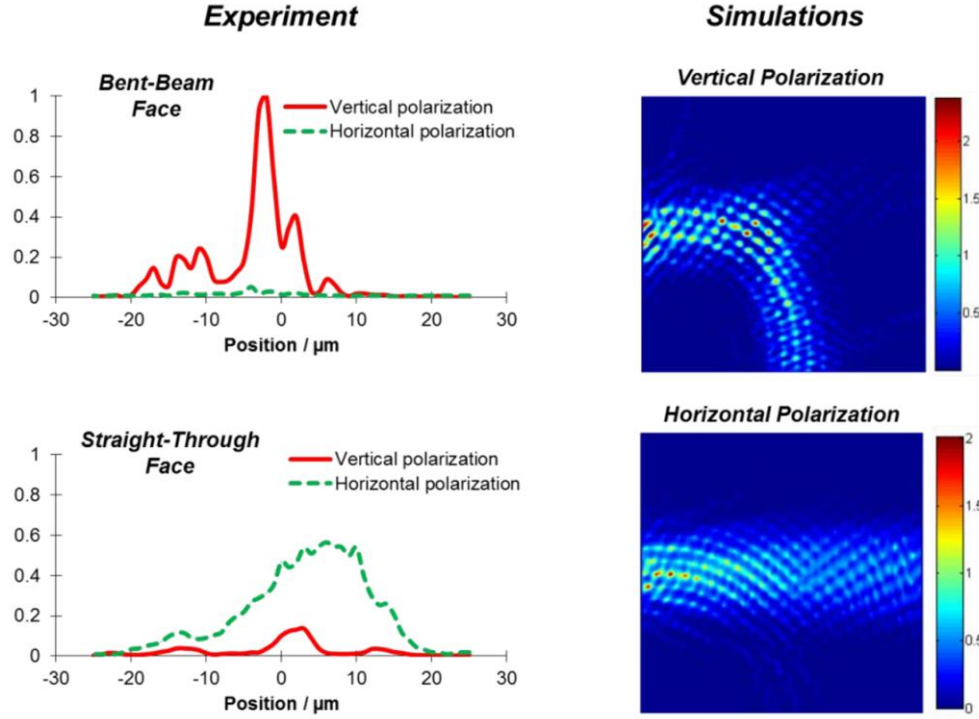


Figure 5.11 [61]: Experimental results of the intensity line-scans for an SVPC guiding a vertically polarized beam versus a horizontally polarized one. The simulation visually agrees very well with experimental measurements.

Comparing beam bending efficiencies between SVPCs and devices such as dielectric waveguides, graded index devices, and more, is difficult because the performance of each depends on parameters which may vary depending on the design requirements. However, it is useful to make a comparison between existing reports, taking note of the differences in fabrication complexity, material requirements, and more. From a survey of existing reports on waveguides, Ref. [61] devised a preliminary performance metric for devices that bend electromagnetic waves. This metric was defined as the product of the bend radius, normalized to the operating wavelength, and the refractive index contrast  $(R_{bend}/\lambda_0)\Delta n$ . The bend radius is important because it impacts the size of the device; the lower the better. The index contrast is also important because, although higher index contrast allows for a stronger control of the fields, material requirements can become exotic and expensive very quickly; here, as well, lower contrast is desired.

The survey concluded that the two efforts presented in this chapter, a SVPC for infrared wavelengths and an SVPC for microwaves, were the owners of the two lowest performance metrics, equaling the best performance. The SVPC for microwaves resulted in a performance metric of 3.6, while the SVPC for infrared wavelengths resulted in a value of 3.7. The latter was then classified as the world's tightest bend for optical beams.

Figure 5.12 [61] shows an example SVPC and the intensity measurements around its perimeter.

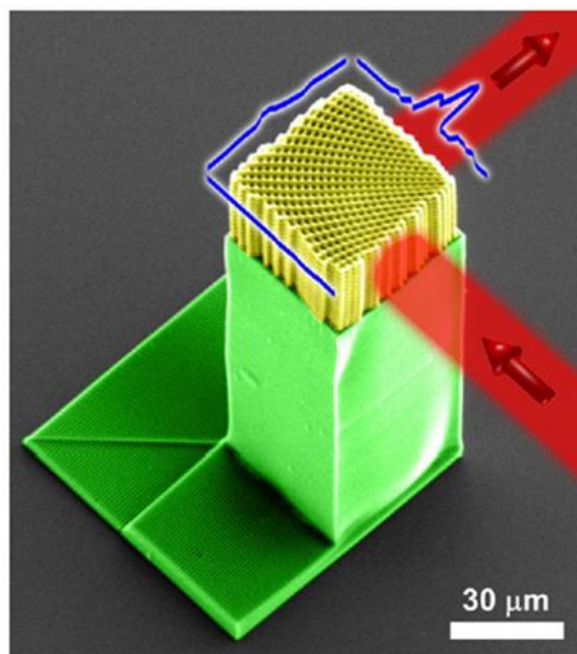


Figure 5.12 [61]: False-color SEM image of a spatially variant photonic crystal and the field profile measurements (blue ribbons) along its perimeter, confirming a successful bending of optical beams.

## **Chapter 6: Spatially Variant Multi-Mode Photonic Crystal Waveguides**

### **6.1 INTRODUCTION**

Electronic systems follow a trend of increasing information capacity and decreasing component size with every new generation [29]. This poses a problem for the current data channel infrastructure, where metal interconnects are the principal means for data piping. Metallic interconnects suffer from issues like limited bandwidth, which greatly increases the number of channels required to fulfill increasing data demands. They're also not optimal for data routing, where achieving a bend with metal interconnects requires a large bend radius to avoid mode leaking and scrambling. Photonic crystals offer a promising solution to these issues. Photonic crystal band gap waveguides could serve as components in a network of optical interconnects, where these can be optimized to offer tight beam routing [60, 61] and excellent multi-mode signal integrity even after routing. They can also offer solutions to other problems such as waveguide crossing through novel spatially variant designs [59].

Photonic crystal band gap waveguides derive from the band gap phenomenon in photonic crystals [72-81]. In a band gap lattice, a waveguide structure could be achieved by introducing a line defect (removing a row of unit cells) in the lattice, where energy would be forced to propagate along it due to the mirror nature of the band gap lattice.

A greatly promising structure for optical systems would consist of a band gap waveguide with the ability to transmit multiple channels of information at a single frequency and to arbitrarily and abruptly route the waveguides. To this effect, this chapter presents the results of a spatially variant multi-mode photonic crystal waveguide based on band gaps. The multi-mode design allows for the transmission of multiple channels of information, while the synthesized spatial variance allows for abrupt and arbitrary routing of the waveguides.

### **6.2 BACKGROUND**

Multi-mode waveguides are of great interest for optoelectronic circuits because applying multiple channels of information onto different modes greatly increases the information capacity

and decreases the number of waveguides needed, reducing the on-chip real estate typically required by these [82, 83]. Unfortunately, few efforts can be found on the topic of information routing in multi-mode waveguides. Efficient multiplexing has been achieved in optical fibers [84-86], but it is not clear how this would extend to spatially variant designs, where these modes would have to be arbitrarily routed. The studies on spatially variant multi-mode waveguides include a gradual  $90^\circ$  multi-mode bend utilizing transformation optics [82], and another sharp  $90^\circ$  multi-mode bend achieved through topology optimization [83]. Both of these works are designed to guide a total of three modes. Ref. [82] requires a large bend radius ( $> 50\lambda_0$ ) and a graded refractive index profile with very subwavelength features which increases fabrication complexity. Ref. [83] achieves a multi-mode bend through highly optimized topology, where it suffers from a narrow bandwidth, and it becomes unclear how well this method would extend to waveguides supporting more modes.

More work can be found on the analysis and computation of uniform multi-mode band gap waveguides. In these, the connection between the number of unit cell rows removed and the number of modes supported appears to be one-to-one. This is implied in the naming convention, where “W3” would refer to a defect width of three rows while supporting three guided modes [46]. A more robust approximation to this considered the width of the mode. For instance, for the lowest frequency mode, half of the wavelength should fit within the defect. This approximates the defect width required for one mode to be  $w_{w1} \approx \lambda/2$  [32]. Lattices designed for band gaps are typically subwavelength, so a one-to-one connection between the number of guided modes and the number of defect rows is a good approximation.

## **6.3 PHOTONIC CRYSTAL BAND GAP WAVEGUIDES**

### **6.3.1 Methodology Survey**

Photonic crystal waveguides based on band gaps have been analyzed using various numerical methods including the finite-difference time-domain (FDTD) method [72, 73, 75-77, 79, 80], transfer matrix method (TMM) in a plane wave basis [74], the plane wave expansion

method (PWEM) [29], and more, including an eigenfunction framework using the finite-difference frequency-domain (FDFD) method that will be presented in this work. The FDFD framework used here has the advantage of calculating the eigenmodes and simulating the fields on the same grid. Additionally, efforts vary in the specific technique used to compute guided modes and distinguish them from evanescent or standing ones [29]. Some of the techniques used for finding guided modes include exciting a dipole source [76], where the idea is that, in a time-domain analysis, the guided modes will remain and outlast the decaying transient ones. Another technique includes the filter diagonalization technique [72], which was not explored here.

One study performs an optimization of the defect width [77] of a W1 photonic crystal waveguide to extract guided modes. More generally, there are studies such as those found in Ref. [80], which attempt to survey and compare the general methods for designing single-mode photonic crystal waveguides. This particular reference claims that photonic crystal waveguides based on triangular band gap lattices yield the best results, however that claim was not investigated in this work. There are also three-dimensional models of photonic crystal band gap waveguides investigated where the (out of plane) height is comparable to the wavelength [87-89]. These are commonly termed photonic crystal “slabs”, and they operate under the additional out-of-plane guiding mechanism total internal reflection (TIR), and as such, they require full 3D simulations (computationally expensive); these were not investigated in this work. There also remains the problem of multiplexing/demultiplexing on the separate modes. This work studies only the propagation of multiple modes in the waveguide.

### **6.3.2 Modeling Photonic Crystal Waveguides**

The characterization of photonic crystal band gap waveguides in this work begins with the “supercell” technique [29, 46]. Figure 6.1 shows a single line-defect (W1) photonic crystal band gap waveguide along with its supercell representation.

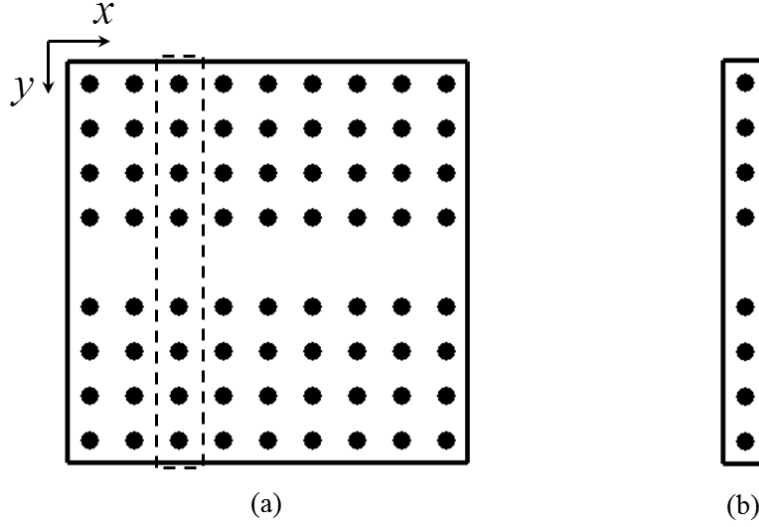


Figure 6.1: (a) A common photonic crystal waveguide and (b) its supercell representation.

The supercell technique is helpful for models with high symmetry. While periodicity along the  $x$  from Figure 6.1 is evident and straightforward, periodicity along the  $y$  requires further consideration. One simple technique is to consider a stretched unit cell along the  $y$ , thus creating a “supercell”. The critical region is around the defect, so this technique requires a minimum number of “buffer” unit cells along the  $y$  to achieve a pseudo-periodicity. One study recommends 12 unit cells on each of the surrounding sides of the defect region as enough of a buffer [76], and this work found that to be a healthy recommendation. A rigorous method to determine the minimum number of buffer unit cells needed will be discussed in the coming sections.

### 6.3.3 Simulation of Photonic Crystal Waveguide Modes

#### *FDFD for Eigenvalue Problems*

This work utilizes the FDFD algorithm to solve an eigenvalue problem where the frequencies (eigenvalues) and the mode shapes (eigenvectors) are computed to extract guided modes in a photonic crystal waveguide. The details are as follows.

The formulation begins with Maxwell’s equations in the form of Eqs. (2.14)-(2.15). They are restated here for convenience.

$$\begin{aligned}
\frac{\partial E_z}{\partial y} - \frac{\partial E_y}{\partial z} &= k_0 (\mu_{xx} \tilde{H}_x + \mu_{xy} \tilde{H}_y + \mu_{xz} \tilde{H}_z) \\
\frac{\partial E_x}{\partial z} - \frac{\partial E_z}{\partial x} &= k_0 (\mu_{yx} \tilde{H}_x + \mu_{yy} \tilde{H}_y + \mu_{yz} \tilde{H}_z) \\
\frac{\partial E_y}{\partial x} - \frac{\partial E_x}{\partial y} &= k_0 (\mu_{zx} \tilde{H}_x + \mu_{zy} \tilde{H}_y + \mu_{zz} \tilde{H}_z)
\end{aligned} \tag{6.1}$$

$$\begin{aligned}
\frac{\partial \tilde{H}_z}{\partial y} - \frac{\partial \tilde{H}_y}{\partial z} &= k_0 (\varepsilon_{xx} E_x + \varepsilon_{xy} E_y + \varepsilon_{xz} E_z) \\
\frac{\partial \tilde{H}_x}{\partial z} - \frac{\partial \tilde{H}_z}{\partial x} &= k_0 (\varepsilon_{yx} E_x + \varepsilon_{yy} E_y + \varepsilon_{yz} E_z) \\
\frac{\partial \tilde{H}_y}{\partial x} - \frac{\partial \tilde{H}_x}{\partial y} &= k_0 (\varepsilon_{zx} E_x + \varepsilon_{zy} E_y + \varepsilon_{zz} E_z)
\end{aligned} \tag{6.2}$$

For ease of computation implementation, at this point they are written in matrix form.

$$\begin{aligned}
\mathbf{D}_y^e \mathbf{e}_z - \mathbf{D}_z^e \mathbf{e}_y &= k_0 \boldsymbol{\mu}_{xx} \tilde{\mathbf{h}}_x \\
\mathbf{D}_z^e \mathbf{e}_x - \mathbf{D}_x^e \mathbf{e}_z &= k_0 \boldsymbol{\mu}_{yy} \tilde{\mathbf{h}}_y \\
\mathbf{D}_x^e \mathbf{e}_y - \mathbf{D}_y^e \mathbf{e}_x &= k_0 \boldsymbol{\mu}_{zz} \tilde{\mathbf{h}}_z
\end{aligned} \tag{6.3}$$

$$\begin{aligned}
\mathbf{D}_y^h \tilde{\mathbf{h}}_z - \mathbf{D}_z^h \tilde{\mathbf{h}}_y &= k_0 \boldsymbol{\varepsilon}_{xx} \mathbf{e}_x \\
\mathbf{D}_z^h \tilde{\mathbf{h}}_x - \mathbf{D}_x^h \tilde{\mathbf{h}}_z &= k_0 \boldsymbol{\varepsilon}_{yy} \mathbf{e}_y \\
\mathbf{D}_x^h \tilde{\mathbf{h}}_y - \mathbf{D}_y^h \tilde{\mathbf{h}}_x &= k_0 \boldsymbol{\varepsilon}_{zz} \mathbf{e}_z
\end{aligned} \tag{6.4}$$

For analysis where the  $z$  is assumed to be of infinite extent and propagation is restricted to the  $x$ - $y$  plane, these decouple into two distinct modes (for detailed derivation, see Chapter 2).

The TM mode:

$$\left( \mathbf{D}_x^h \boldsymbol{\mu}_{yy}^{-1} \mathbf{D}_x^e + \mathbf{D}_y^h \boldsymbol{\mu}_{xx}^{-1} \mathbf{D}_y^e \right) \mathbf{e}_z = -k_0^2 \boldsymbol{\varepsilon}_{zz} \mathbf{e}_z \tag{6.5}$$

The TE mode:

$$\left( \mathbf{D}_x^e \boldsymbol{\varepsilon}_{yy}^{-1} \mathbf{D}_x^h + \mathbf{D}_y^e \boldsymbol{\varepsilon}_{xx}^{-1} \mathbf{D}_y^h \right) \tilde{\mathbf{h}}_z = -k_0^2 \boldsymbol{\mu}_{zz} \tilde{\mathbf{h}}_z \tag{6.6}$$

These take on the form of generalized eigenvalue problems  $\mathbf{Ax} = \lambda \mathbf{Bx}$ .

Analysis of the supercell requires Bloch boundary conditions, rather than simple periodic, to account for wave propagation. In the FDFD algorithm, the computation of the derivative operators  $\mathbf{D}_x^e, \mathbf{D}_x^h, \mathbf{D}_y^e, \mathbf{D}_y^h$  requires an incident wave vector  $\vec{k}_{inc}$ . In this formulation, the Bloch wave vector  $\vec{\beta}$  fills this role. Figure 6.2 represents the TM mode formulation visually, and where information of the Bloch wave vector is embedded.

$$\vec{\beta}$$

$$(\mathbf{D}_x^h \boldsymbol{\mu}_{yy}^{-1} \mathbf{D}_x^e + \mathbf{D}_y^h \boldsymbol{\mu}_{xx}^{-1} \mathbf{D}_y^e) \mathbf{e}_z = -k_0^2 \boldsymbol{\epsilon}_{zz} \mathbf{e}_z$$

Figure 6.2: In the FDFD algorithm, information of the Bloch wave vector, which accounts for propagation of the Bloch waves, is embedded in the derivative operators.

### ***Extracting Guided Modes***

As per the formulation of Eqs. (6.5) and (6.6), the algorithm described above attempts to find guided modes corresponding to a given Bloch wave vector  $\vec{\beta}$ . This requires a proper selection of the Bloch wave vector, where guided modes are supposed to exist. Photonic crystal waveguides operate based on the mirror properties of the band gap lattice, therefore it follows that the operating frequencies of a band gap waveguide reside within the band gap of the infinite lattice. These band gap frequencies can be determined by the band diagram of the infinite lattice.

One characteristic of a guided mode is the localization of power within the defect. Solution of the eigenvalue problem presented here results in  $N_x \cdot N_y$  number of solutions (eigenvalues), equaling the number of points in the two-dimensional grid being modeled. Because it is expected that a guided mode propagates almost entirely within the defect, a simple preliminary check for guided modes from the list of eigenvectors consists of computing the power density in a specified area of the waveguide. One study suggests sorting through the list of eigenvectors and retaining those which have less than 10% of their total energy along the

boundaries of the supercell [29]. The technique of this work consists of measuring the power density of the area within the defect, and the areas extending to within a number of unit cells equal to at least the defect width on each side of it. Potentially guided modes were selected as those eigenvectors which contained  $\geq 90\%$  of the power within this region.

Once a list of potentially guided modes has been retained, they are simulated as a uniform waveguide via the FDFD method. This is to test for those modes which are truly guided, as opposed to those that are standing or evanescent [29]. A FDFD simulation is a good test because guided modes will propagate along the uniform lattice while retaining their mode shape, as opposed to the non-guided modes, which will either decay or strongly scatter.

#### **6.4 MULTI-MODE BAND GAP WAVEGUIDES**

The analysis of multi-mode band gap waveguides initially follows the same procedure as the single-line defect models. The band gap frequency range must first be calculated. This is achieved through a band diagram analysis of the infinite lattice, as discussed in Chapter 3. The possible eigensolutions, then, for the waveguide modes are restricted to those within the band gap. Multi-mode waveguides, however, require multiple wave vector solutions for a single frequency because each of the modes possesses a different propagation constant. Following the FDFD formulation prescribed here, this work utilized Newton's method [90] to search for the wave vectors having a target frequency as their solution. It should be recalled that the band gap frequencies are calculated from the infinite lattice. The defect width of the waveguide may dictate the number of guided modes, but up to a certain point this correlation breaks down, as the fixed band gap width will have a limited number of solutions it can support.

Figure 6.4 shows a uniform four unit cell wide line defect (W4) waveguide and its four propagating modes.

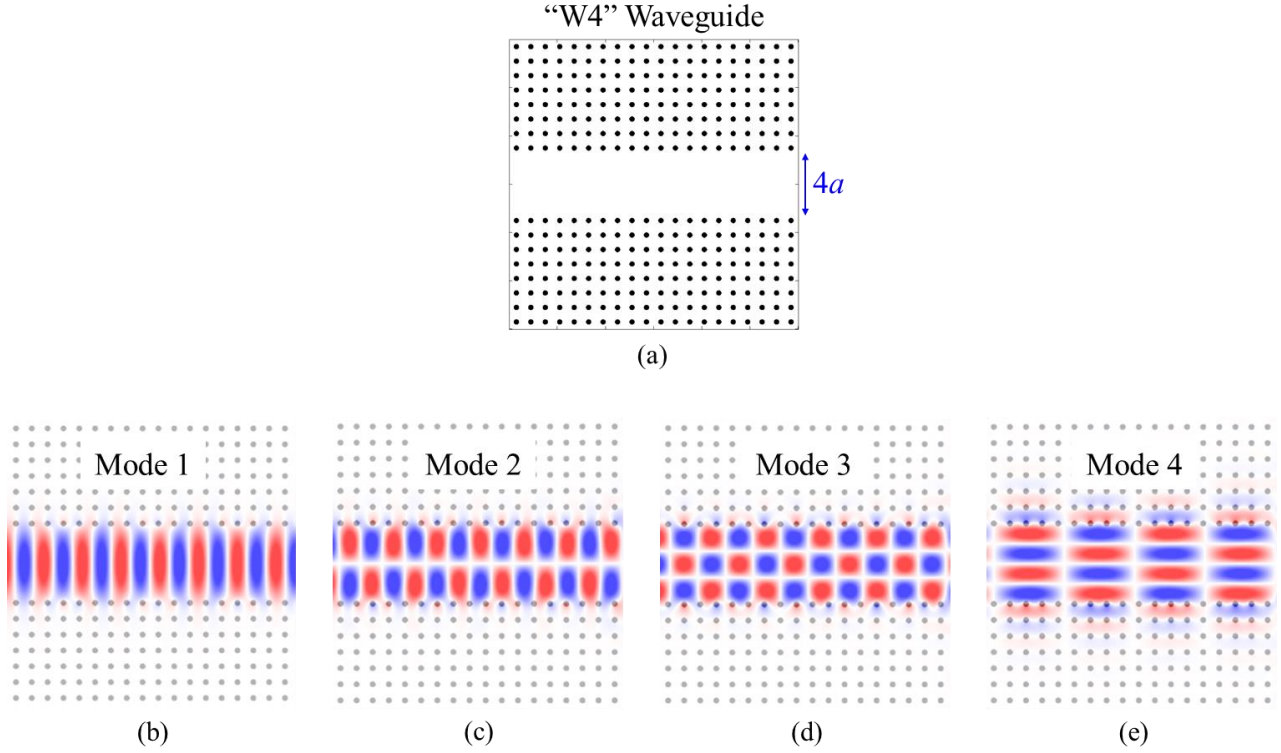


Figure 6.4: (a) A photonic crystal band gap waveguide with a line defect width of  $4a$  and (b-e) the four guided modes that it supports. The lattice consists of dielectric rods of index  $n = 3.4$  and radius  $r = 0.18a$  in an air background. These simulations were performed at a normalized frequency of  $a/\lambda_0 = 0.42$ .

The four modes that this W4 waveguide supports operate at the same frequency, but with different propagation constants defined by the Bloch wave vectors. The different propagation constants are responsible for the apparent wavelengths that the different modes exhibit along the horizontal axis. This waveguide was modeled from the lattice in Ref. [46], consisting of dielectric rods of index  $n = 3.4$  and radius  $r = 0.18a$  in an air background.

## 6.5 SPATIALLY VARIANT MULTI-MODE BAND GAP WAVEGUIDES

If there is hope for photonic crystal waveguides to populate an optoelectronic circuit, they will need to route, bend, and control signals throughout the circuit much like dielectric waveguides do now. A substantial amount of work has been performed to achieve and optimize bends of varying degrees with photonic crystal waveguides [39-48, 91-94]. These achieve

efficient beam bending through the use of techniques including topology optimization, the use of dielectric mirrors and splitters, and more. They are only designed to support one mode. As mentioned in a previous section, only a handful of efforts have been reported to achieve the routing of multiple modes on a single waveguide while minimizing the crosstalk between them [82, 83]. Inter-modal coupling remains the primary challenge for multi-mode waveguides through tight bends.

This work aims to generate spatially variant photonic crystal waveguides using the synthesis algorithm described in Chapter 4 [21]. Preliminary efforts included a photonic crystal band gap waveguide made to bend  $90^\circ$ . A spatially variant W4 photonic crystal waveguide is shown on Figure 6.5 (a).

It was found in this work that narrow line-defect waveguides allowed for a more abrupt turning than wide defect ones. To remain competitive, this work sought to achieve at least four modes in a spatially variant band gap waveguide. As consequence of this difficult goal, the spatially variant waveguide required additional deformation control [59], as discussed in Chapter 4. The critical regions for deformation control in this waveguide were selected as narrow as possible, as this allowed for a greater degree of correction. They were made to extend at least two unit cells past the defect width, as the “tails” of the guided modes extend to a width approaching that. The spatially variant W4 waveguide, along with its regions of enforced deformation control superimposed, are shown in Figure 6.5(b).

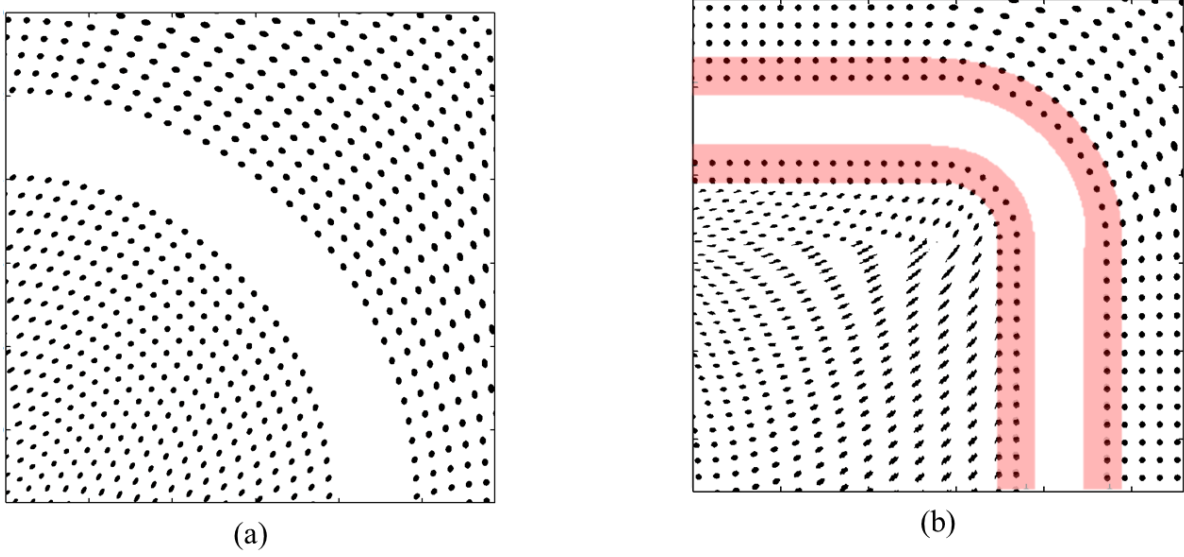


Figure 6.5: (a) A spatially variant W4 photonic crystal band gap waveguide made to turn  $90^\circ$ . Waveguides supporting a large number of modes are more sensitive to deformations in the lattice when spatially varied. These waveguides require additional deformation control; (b) shows a waveguide with uniform regions at the input and output faces, and its regions of deformation control shaded red.

The lattices of Figure 6.5 are  $11.75\lambda_0$  wide and tall. The baseline unit cell is the same discussed in previous sections from Ref. [46]. The resulting lattice from Figure 6.5 (b) is designed with a bend radius of  $r_{bend} = 3.2\lambda_0$ , where the lattice constant is  $a = 0.42\lambda_0$ . This lattice was designed with uniform regions at the input and output faces to ease the transition of the beam.

### 6.5.1 Comparison of Spatially Variant Multi-Mode Waveguides

This preliminary study on multi-mode photonic crystal waveguides in spatially-variant lattices suggests that this is a highly promising technique for realizing sharp bends while also suppressing coupling between the modes. The results from this study are summarized in Figure 6.6 [59]. Each row in the figure shows the first three modes in the same waveguide propagating around a bend of radius  $3.2\lambda_0$ . The first column shows the 1st-order mode in each waveguide, the second column shows the 2nd-order mode, and the third column shows the 3rd-order mode. The first row shows an ordinary dielectric waveguide in air with a width of  $0.5\lambda_0$  and a core refractive index of 3.4. This is a very high contrast waveguide but showcases dielectric

waveguides in their best case. The shape of the modes change through the bend, showing that the bend has produced coupling between the modes. The 3rd-order mode is also observed to be leaking out of the waveguide around the bend. The second row shows a uniform photonic crystal with a multimode waveguide removed from it which has a bend radius of  $3.2 \lambda_0$ . This lattice possesses a band gap so there is no leakage from the waveguides, but the bends induce strong reflections that can be discerned from the field intensity in the plots. In addition, the inter-modal coupling is obvious by looking at the mode profiles exiting the bends which no longer resemble the pure modes. The last row in the figure shows the same photonic crystal, but the lattice was spatially varied to form a bend of radius  $3.2 \lambda_0$ . The lattices were generated using deformation control where the critical regions were defined to be the two unit cells on either side of the waveguide. The quality of the lattice outside of these regions is poor, but these regions are not important to performance of the bend. While not shown here, similar lattices generated using the basic algorithm were observed to leak from the waveguide because the deformations weakened the band gap. Very clean transmission was observed for all three modes, suggesting the inter-modal coupling was virtually eliminated. Future work in this area will calculate the intermodal coupling more rigorously, explore waveguides that support more modes, and explore hexagonal lattices that support stronger band gaps.

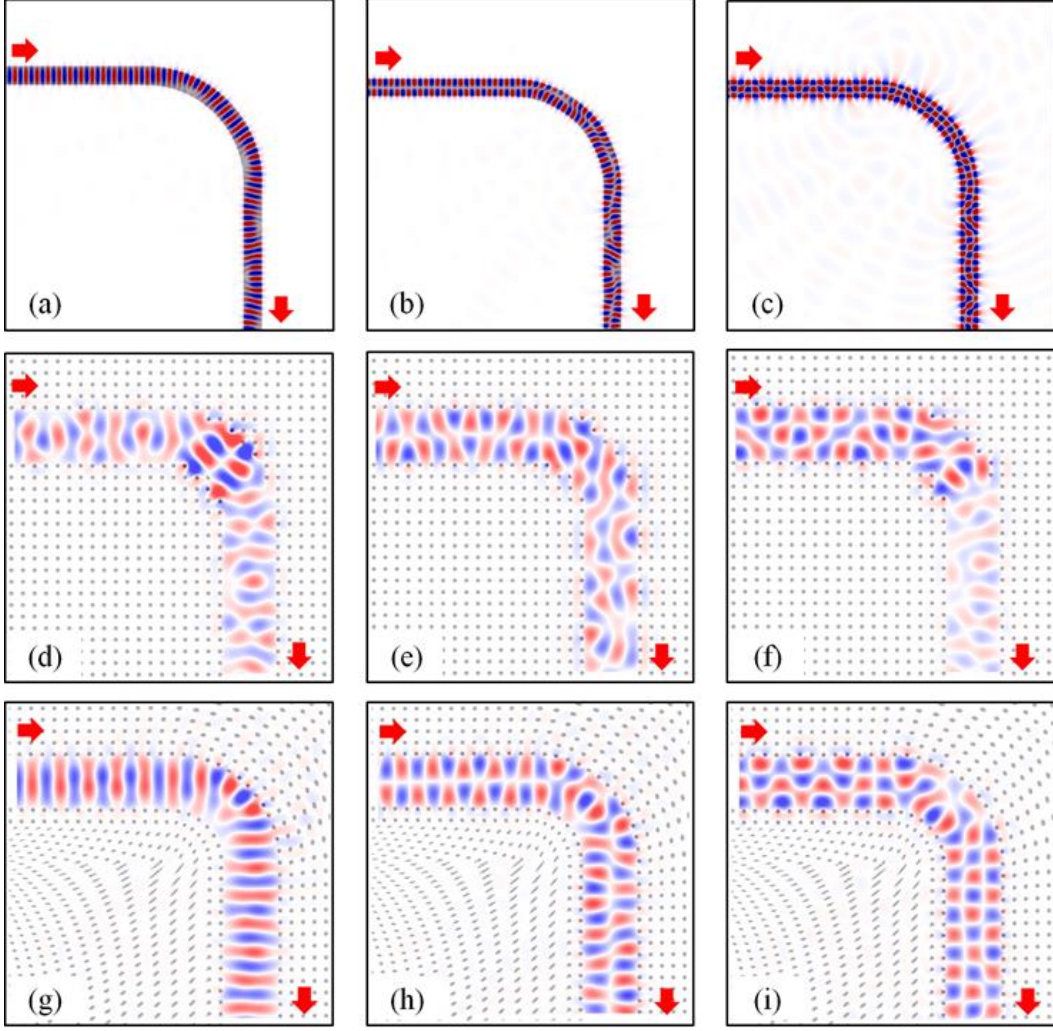


Figure 6.6 [59]: (a)-(c) First three modes in an ordinary multimode dielectric waveguide with  $n_{core} = 3.4$  and  $n_{clad} = 1.0$ . Width of the guide was  $w = 0.5\lambda_0$ . (d)-(f) First three modes in a multimode band gap waveguide cut from a uniform lattice with  $n_{rod} = 3.4$  and  $n_{air} = 1.0$ . Lattice spacing is  $a = 0.42\lambda_0$ , bend radius is  $r_{bend} = 3.2\lambda_0$ , rod radius is  $0.18a$ , and the width of the guide was  $4a$ . (g)-(i) First three modes in a multimode band gap waveguide cut from a spatially-variant lattice with the same parameters as (d)-(f).

## **Chapter 7: Conclusion**

### **7.1 SUMMARY**

A synthesis algorithm was developed that is capable of simultaneously and independently spatially varying the orientation, fill-fraction, lattice spacing, and other properties of a periodic structure throughout its volume in such a manner that will render the resulting lattice smooth and continuous. Maintaining uniformity and minimizing defects is important, as dispersive effects are typically tuned to unit cell geometry and material composition.

The self-collimation effect and the band gap phenomena were selected as two useful tools to control electromagnetic fields. Both of these exist under strict dependencies related to lattice orientation, which limits their application. If the orientation of the lattice itself was spatially varied and routed arbitrarily, then the directional dependencies of these effects would be effectively exploited, enabling an entirely new paradigm of device design and capabilities. This is what the synthesis algorithm achieved, enabling unprecedented control over the electromagnetic field through novel spatially variant photonic crystals. These enabled more abrupt field control than other efforts that have been reported.

### **7.2 FUTURE WORK**

The synthesis algorithm, the optimized self-collimation effect, and the success of spatially variant multi-mode band gap waveguides were proof of concept devices which will serve as enabling technologies for devices based on it. One example of a combination of these revolutionary efforts could be a multi-mode waveguide based on self-collimation. This type of device would be advantageous over band gap waveguides because band gap lattices require relatively high index contrast. Self-collimation, on the other hand, prefers low index contrast. Additionally, modes could prove to propagate under stronger confinement, as they are not propagated solely under total internal reflection. These efforts can also serve as enhancements for current wave control methodologies and technologies.

## References

- [1] D. C. Dobson, and S. J. Cox, SIAM Journal on Applied Mathematics **59** (1999).
- [2] C. Kao, S. Osher, and E. Yablonovitch, Applied Physics B **81** (2005).
- [3] R. D. Meade *et al.*, Physical Review B **48** (1993).
- [4] K. Sakoda, and H. Shiroma, Physical Review B **56** (1997).
- [5] P. Sarrafi *et al.*, Optics Communications **281** (2008).
- [6] H. Uranus, and H. Hoekstra, Opt. Express **12** (2004).
- [7] D. Chigrin *et al.*, Opt. Express **11** (2003).
- [8] R. E. Hamam *et al.*, Opt. Express **17** (2009).
- [9] D. W. Prather *et al.*, Journal of Physics D: Applied Physics **40** (2007).
- [10] D. W. Prather *et al.*, Opt. Lett. **29** (2004).
- [11] R. C. Rumpf, and J. J. Pazos, JOSA A **30** (2013).
- [12] D. Tang, L. Chen, and W. Ding, Applied physics letters **89** (2006).
- [13] J. Witzens, M. Loncar, and A. Scherer, Selected Topics in Quantum Electronics, IEEE Journal of **8** (2002).
- [14] T. Yamashita, and C. J. Summers, Selected Areas in Communications, IEEE Journal on **23** (2005).
- [15] G. Gok, and A. Grbic, Physical Review Letters **111** (2013).
- [16] R. C. Rumpf *et al.*, Progress In Electromagnetics Research **142** (2013).
- [17] H. Kosaka *et al.*, Physical Review B **58** (1998).
- [18] L. Wu, M. Mazilu, and T. F. Krauss, Journal of Lightwave Technology **21** (2003).
- [19] T. Ergin *et al.*, Science **328** (2010).
- [20] J. Li, and J. Pendry, Physical Review Letters **101** (2008).
- [21] R. C. Rumpf, and J. Pazos, Opt. Express **20** (2012).
- [22] J. B. Pendry, D. Schurig, and D. R. Smith, Science **312** (2006).
- [23] D. J. Griffiths, *Introduction to Electrodynamics* 1999), Vol. 3.
- [24] R. C. Rumpf, in *College of Optics* (University of Cetr al Florida, Orlando, Florida, 2006).
- [25] M. N. O. Sadiku, *Numerical Techniques in Electromagnetics* (CRC Press, 2001).
- [26] R. C. Rumpf, Progress In Electromagnetics Research B **36** (2012).
- [27] Y. Kane, Antennas and Propagation, IEEE Transactions on **14** (1966).
- [28] R. C. Rumpf, (2006).
- [29] D. W. Prather, *Photonic Crystals, Theory, Applications and Fabrication* (John Wiley & Sons, 2009), Vol. 68.
- [30] C. Kittel, and P. McEuen, *Introduction to solid state physics* (Wiley New York, 1976), Vol. 8.
- [31] T. M. Apostol, (1974).
- [32] J. Joannopoulos *et al.*, *Photonic Crystals: Molding the Flow of Light (Second Edition)* (Princeton University Press, 2008).
- [33] E. Cassan *et al.*, Journal of Lightwave Technology **29** (2011).
- [34] K.-V. Do *et al.*, Opt. Express **20** (2012).
- [35] Y.-Y. Li *et al.*, Applied optics **47** (2008).
- [36] B. Oner, M. Turdjev, and H. Kurt, Opt. Lett. **38** (2013).
- [37] X.-H. Sun *et al.*, Optics Communications **315** (2014).
- [38] H.-W. Wang, and L.-W. Chen, JOSA B **28** (2011).
- [39] T. Baba, N. Fukaya, and J. Yonekura, Electronics letters **35** (1999).

- [40] S. Boscolo, M. Midrio, and C. G. Someda, Quantum Electronics, IEEE Journal of **38** (2002).
- [41] A. Chutinan, and S. Noda, Physical Review B **62** (2000).
- [42] A. Chutinan, M. Okano, and S. Noda, Applied physics letters **80** (2002).
- [43] L. Frandsen *et al.*, Opt. Express **12** (2004).
- [44] Z. Hu, and Y. Y. Lu, Optics Communications **284** (2011).
- [45] C. Jin *et al.*, Applied physics letters **75** (1999).
- [46] Z.-Y. Li, L.-L. Lin, and K.-M. Ho, Applied physics letters **84** (2004).
- [47] A. Mekis *et al.*, Physical Review Letters **77** (1996).
- [48] M. Tokushima *et al.*, Applied physics letters **76** (2000).
- [49] M. Lax, *Symmetry principles in solid state and molecular physics* (Courier Dover Publications, 1974).
- [50] M. I. Hussein, *Reduced Bloch mode expansion for periodic media band structure calculations* (2009), Vol. 465, 2109.
- [51] J. Hou *et al.*, Optics Communications **282** (2009).
- [52] R. C. Rumpf, 2014).
- [53] R. C. Rumpf, 2014), p. 9.
- [54] S. C. Chapra, and R. Canale, *Numerical Methods for Engineers: With Software and Programming Applications* (McGraw-Hill Higher Education, 2001).
- [55] B. Noble, and J. W. Daniel, *Applied linear algebra* (Prentice Hall, 1977).
- [56] D. Bindel, 2012).
- [57] Y. Saad, *Iterative Methods for Sparse Linear Systems* (Society for Industrial and Applied Mathematics, 2003).
- [58] C. C. Paige, and M. A. Saunders, ACM Trans. Math. Softw. **8** (1982).
- [59] J. J. P. R.C. Rumpf, J.L. Digaum, S.M. Kuebler, Phil. Trans. R. Soc. A. (2014).
- [60] R. C. Rumpf *et al.*, Progress In Electromagnetics Research **139** (2013).
- [61] J. L. Digaum *et al.*, Opt. Express **22** (2014).
- [62] F. Capolino, *Theory and phenomena of metamaterials* (CRC Press, 2009).
- [63] E. Ponizovskaya, M. Nieto-Vesperinas, and N. Garcia, Applied physics letters **81** (2002).
- [64] L. J. V. Varadan, Metamaterials 2008 (2008).
- [65] G. M. Batanov *et al.*, The European Physical Journal - Applied Physics **26** (2004).
- [66] I. Anzel, Association of Metallurgical Engineers of Serbia (2007).
- [67] R. C. Rumpf, in *Synthesizing Geometries for 21st Century Electromagnetics* (2014).
- [68] L. C. Botten *et al.*, Physical Review E **74** (2006).
- [69] W. Śmigaj, and B. Gralak, Physical Review B **85** (2012).
- [70] T. Baba, T. Matsumoto, and M. Echizen, Opt. Express **12** (2004).
- [71] R. Biswas, Z. Li, and K. Ho, Applied physics letters **84** (2004).
- [72] B. Dastmalchi *et al.*, Progress In Electromagnetics Research B **26** (2010).
- [73] X. Letartre *et al.*, Applied physics letters **79** (2001).
- [74] Z.-Y. Li, and K.-M. Ho, Physical Review B **68** (2003).
- [75] M. Loncar *et al.*, Lightwave Technology, Journal of **18** (2000).
- [76] A. Mekis, S. Fan, and J. Joannopoulos, Physical Review B **58** (1998).
- [77] M. Notomi *et al.*, Quantum Electronics, IEEE Journal of **38** (2002).
- [78] H. Taniyama, M. Notomi, and Y. Yoshikuni, Physical Review B **71** (2005).
- [79] J. Witzens *et al.*, JOSA A **20** (2003).
- [80] N. Wu *et al.*, Opt. Express **11** (2003).

- [81] X. Yu, W. T. Lau, and S. Fan, Opt. Lett. **31** (2006).
- [82] L. H. Gabrielli *et al.*, Nature Communications **3** (2012).
- [83] V. Liu, and S. Fan, Opt. Express **21** (2013).
- [84] S. H. Murshid, and A. Chakravarty, Optical Engineering **47** (2008).
- [85] S. Murshid, B. Grossman, and P. Narakorn, Optics & Laser Technology **40** (2008).
- [86] S. H. Murshid, A. Chakravarty, and R. Biswas, in *Proceedings of the Eighth IASTED International Conference on Wireless and Optical Communications* (ACTA Press, 2008), pp. 204.
- [87] S. G. Johnson *et al.*, Physical Review B **60** (1999).
- [88] M. Patrini *et al.*, Physica E: Low-dimensional Systems and Nanostructures **17** (2003).
- [89] S. Shi, C. Chen, and D. W. Prather, JOSA A **21** (2004).
- [90] R. L. Finney, M. D. Weir, and G. B. Thomas, *Thomas' calculus: early transcendentals* (Addison-Wesley, 2001).
- [91] E. K. Chow *et al.*, in *Symposium on Integrated Optics* (International Society for Optics and Photonics, 2001), pp. 453.
- [92] M. Notomi *et al.*, Physical Review Letters **87** (2001).
- [93] I. Ntakis, P. Pottier, and M. Richard, Journal of applied physics **96** (2004).
- [94] K. Schmidt, and R. Kappeler, Opt. Express **18** (2010).

## **Vita**

Javier J. Pazos obtained his Ph.D. in Electrical Engineering in 2014. His bachelor's degree (B.S.) is in Engineering Physics, Electrical track, and was obtained in 2010. His undergraduate curriculum was more strongly focused on electromagnetics and high frequency engineering. This interest carried on to his graduate focus in electromagnetics.

Javier's work in computational electromagnetics, specifically the design of novel photonic crystal devices, was disseminated in the form of a number of peer-reviewed publications in journals including the Optical Society of America (OSA), Progress in Electromagnetics Research (PIERs), and IEEE. This included work done during a technical internship at Intel Corporation.

Apart from the duties of a researcher, Javier has, throughout most of his scholastic career, held positions as an educator. These positions include a teaching assistant, course instructor, and lab instructor. He holds experience as an educator of students of a broad range of ages, ranging from middle school students to those of adult ages.

Permanent address: 232 E. Jefferson St.  
Brownsville, Texas, 78520

This dissertation was typed by Javier J. Pazos.